

**MINIMIZING PLANTER FAN EXHAUST VELOCITY
TO REDUCE ENVIRONMENTAL EFFECTS**

A Thesis Submitted to the College of
Graduate and Postdoctoral Studies
In Partial Fulfillment of the Requirements
For the Degree of Master of Science
In the Department of Mechanical Engineering
University of Saskatchewan
Saskatoon

By

Michael Boyko

PERMISSION TO USE

In presenting this thesis in partial fulfillment of the requirements for a Postgraduate degree from the University of Saskatchewan, I agree that the Libraries of this University may make it freely available for inspection. I further agree that permission for copying of this thesis in any manner, in whole or in part, for scholarly purposes may be granted by the professors who supervised my thesis work or, in their absence, by the Head of the Department or the Dean of the College in which my thesis work was done. It is understood that any copying or publication or use of this thesis or parts thereof for financial gain shall not be allowed without my written permission. It is also understood that due recognition shall be given to me and to the University of Saskatchewan in any scholarly use which may be made of any material in my thesis/dissertation.

DISCLAIMER

The names of certain commercial products were exclusively used to meet the thesis and/or exhibition requirements for the degree of Master of Science at the University of Saskatchewan. Reference in this thesis to any specific commercial products, process, or service by trade name, trademark, manufacturer, or otherwise, does not constitute or imply its endorsement, recommendation, or favoring by the University of Saskatchewan. The views and opinions of the author expressed herein do not state or reflect those of the University of Saskatchewan, and shall not be used for advertising or product endorsement purposes.

Requests for permission to copy or to make other uses of materials in this thesis in whole or part should be addressed to:

Head of the Department of Mechanical
Engineering
University of Saskatchewan
57 Campus Drive
Saskatoon, Saskatchewan, S7N 5A9 Canada

Dean
College of Graduate and Postdoctoral Studies
OR
University of Saskatchewan
116 Thorvaldson Building, 110 Science Place
Saskatoon, Saskatchewan, S7N 5C9 Canada

ABSTRACT

Vacuum fans are a critical component of planters used to draw seeds to a rotating perforated disc for precision sowing. As seeds adhere to the disc it is possible for the coatings to become dislodged, pass through the vacuum fan, and be exhausted into the surroundings. To minimize the possible environmental effects from the fan exhaust, the International Organization for Standardization (ISO) passed the ISO 17962 standard. It sets limits on the air velocity measured at a 2 m radius from the fan, and specifies that the exhaust from the fan must be directed groundward. In partnership with CNH Industrial, research was performed to assess the ability of the CNH Industrial vacuum fan to meet this standard. The research had two main goals: to determine if the vacuum fan could meet the standard, and to show that computational fluid dynamics (CFD) could be an effective tool for measuring compliance with the standard.

The first part of the project was to experimentally determine the ability of the fan to meet the standard. This was accomplished by building and testing three fan configurations using the parameters specified in the ISO standard. The first configuration was inverting the fan to direct its exhaust groundward. The second was attaching a two-dimensional (2D) square diffuser to the fan, which reduced the exhaust velocity and redirected it to the ground. The third was attaching a manifold diffuser to the fan, which divided the exhaust into multiple slower exhaust jets, directed towards the ground. Results from all three configurations indicated exhaust velocities that were measured to be below the ISO standard thresholds (less than 2 m/s or 4 m/s, depending on measurement elevation, with the higher velocity limit imposed closer to the ground).

The second part of the project was to create CFD simulations of the inverted fan and 2D square diffuser configurations, and compare them to the experimental results. The models were able to predict the locations and magnitudes of peak velocities around both configurations. This showed that CFD could be an effective tool for measuring standard compliance.

Finally, the CFD models were used to compare the inverted fan to the 2D square diffuser, in terms of impact on the surroundings. It was found that by reducing the fan exhaust velocity, less air would become entrained by the exhaust jet, indicating a reduced likelihood of spreading fugitive seed coatings. Also, the slow exhaust jet would create less of a disturbance when impinging upon the ground.

ACKNOWLEDGMENTS

I would like to express my gratitude to the following people for their help and support with this research project:

- Dr. D. J. Bergstrom, for his advice, guidance, and supervision.
- Dr. Martin Roberge, for his supervision, advice, and instilling in me his passion for engineering.
- The members of my advisory committee, Dr. Donald Bergstrom (Co-Supervisor), Dr. Martin Roberge (Co-Supervisor), Dr. Duncan Cree (Chair), Dr. David Sumner (Member), Dr. Venkatesh Meda (Member), and Dr. Jafar Soltan (External Examiner).
- CNH Industrial, for their financial support, and access to their Research and Development facility in Saskatoon.
- The Department of Mechanical Engineering at the University of Saskatchewan, for their funding and support.
- The Natural Sciences and Engineering Research Council (NSERC), for partnering with CNH Industrial to fund my research with an IPS scholarship.
- Dr. Bob Hawboldt, for his patience and support in completing my graduate program.
- My parents, Wayne and Marcella Boyko, for their love and support in pursuing my academic studies.
- My wife Fiona Boyko, for the late-night debates, for pushing me to finish, and for her love and devotion. Without her support this work would not have been possible.

TABLE OF CONTENTS

PERMISSION TO USE.....	i
DISCLAIMER.....	i
ABSTRACT.....	ii
ACKNOWLEDGMENTS.....	iii
TABLE OF CONTENTS.....	iv
LIST OF FIGURES.....	vi
LIST OF TABLES.....	ix
NOMENCLATURE.....	x
CHAPTER 1 INTRODUCTION AND LITERATURE REVIEW.....	1
1.1 INTRODUCTION.....	1
1.2 OBJECTIVES.....	3
1.3 LITERATURE REVIEW.....	4
1.3.1 Diffuser Design.....	4
1.3.2 CFD.....	8
1.4 ORGANIZATION OF THESIS.....	13
CHAPTER 2 EXPERIMENTAL MEASUREMENTS.....	14
2.1 INTRODUCTION.....	14
2.2 AIR VELOCITY MEASUREMENT.....	14
2.3 THE EXPERIMENTAL CONFIGURATIONS.....	18
2.3.1 Configuration 1: Inverted Vacuum Fan.....	18
2.3.2 Configuration 2: Fan with 2D Square Wide-Angle Diffuser.....	19
2.3.3 Configuration 3: Fan with Manifold Diffuser.....	22
2.4 RESULTS.....	25
2.4.1 Experimental Data from the Three Configurations.....	26
2.5 CHAPTER SUMMARY.....	37
CHAPTER 3 COMPUTATIONAL FLUID DYNAMICS MODELS.....	38
3.1 INTRODUCTION.....	38
3.2 CFD THEORY.....	38
3.3 THE INVERTED VACUUM FAN MODEL.....	46
3.3.1 Inverted Vacuum Fan Geometry.....	47
3.3.2 Mesh.....	49
3.3.3 Solution Set-up.....	52
3.3.4 Results.....	53
3.4 FAN WITH THE 2D SQUARE DIFFUSER.....	58
3.4.1 Two-Dimensional Square Wide-Angle Diffuser Geometry.....	59
3.4.2 Mesh.....	60

3.4.3 <i>Solution Set-up</i>	62
3.4.4 <i>Results</i>	63
3.5 CHAPTER SUMMARY	67
CHAPTER 4 DISCUSSION AND ANALYSIS OF RESULTS	68
4.1 INTRODUCTION	68
4.2 THE INVERTED FAN	68
4.3 THE FAN WITH THE 2D SQUARE DIFFUSER	72
4.4 COMPARISON OF THE FAN AND 2D SQUARE DIFFUSER	76
4.5 SUMMARY OF CHAPTER	79
CHAPTER 5 CONCLUSION AND RECOMMENDATIONS	81
5.1 CONCLUSION	81
5.2 RECOMMENDATIONS	83
REFERENCES	85
APPENDIX A EFFECT OF OUTLET SHAPE ON VELOCITY DISTRIBUTION FOLLOWING JET IMPINGEMENT	88
APPENDIX B FURTHER WORK RESULTING FROM THIS RESEARCH PROJECT	94

LIST OF FIGURES

Figure 1-1: Interior of seed meter assembly with filled seed disc (CNH Industrial, 2014).....	2
Figure 1-2: Domain area for the design method	3
Figure 1-3: 2D wide angle square diffuser	5
Figure 1-4: 2D wide angle square diffuser with vanes	6
Figure 1-5: Trumpet-shaped diffuser (a), bell-shaped diffuser (b).....	7
Figure 1-6: Exploded view of fan	8
Figure 2-1: Measurement frame.....	15
Figure 2-2: Supports for hot film anemometer	15
Figure 2-3: Interaction between measurement frame and planter	16
Figure 2-4: Blank (un-perforated) seed disc to simulate seed disc filled with corn seeds.....	17
Figure 2-5: Configuration 1 inverted vacuum fan	18
Figure 2-6: Top-down view of measurement locations for configuration 1 with exhaust pointed into the page.....	19
Figure 2-7: Configuration 2 fan with 2D square wide-angle diffuser	20
Figure 2-8: Top-down view of 2D square wide-angle diffuser internal geometry	21
Figure 2-9: Fan with manifold diffuser.....	23
Figure 2-10: Bottom up view of manifold diffuser showing the multiple outlets	23
Figure 2-11: Illustration of how overlapping circles create a stadium shape	24
Figure 2-12: Top-down view of measurement points for the manifold diffuser	25
Figure 2-13: Horizontal velocity profiles for configurations 1, 2 and 3 ranging from location 0° to location 150°	27
Figure 2-14: Velocity profile along centreline of exhaust for configuration 1, inverted vacuum fan	30
Figure 2-15: Interior view of vacuum fan.....	31
Figure 2-16: Plot of velocity profile along centreline for configuration 2, 2D square diffuser....	32
Figure 2-17: Schematic view of diffuser flow impingement	32
Figure 2-18: Plots of the velocity profile along the centreline of outlets one to four of the manifold diffuser.....	34
Figure 3-1: Examples of skewness ranging from not skewed to fully skewed.....	39

Figure 3-2: Examples of orthogonal quality	40
Figure 3-3: Examples of unstructured and structured meshes	41
Figure 3-4: Production vacuum fan CAD model	48
Figure 3-5: Exterior and interior of the fan fluid domain	48
Figure 3-6: Isometric view of the fluid domain surrounding the inverted vacuum fan	49
Figure 3-7: Close-up view of the inflation layers in the fan's volute and outlet and the interface between the rotating and stationary meshes.....	50
Figure 3-8: Three-dimensional view of the interior mesh of the fluid domain surrounding the inverted vacuum fan.....	51
Figure 3-9: Velocity contours and vectors inside of fan, 0 m/s – 100 m/s	53
Figure 3-10: Close-up view of velocity contours in the fan volute and outlet, 0 m/s – 16 m/s....	54
Figure 3-11: Close-up view of pressure contours in the fan volute and outlet	55
Figure 3-12: Plot of predicted and measured velocity profiles along centreline of the inverted fan's exhaust	56
Figure 3-13: Side view of velocity contours and vectors of impinging fan exhaust	57
Figure 3-14: Front view of velocity contours and vectors of impinging fan exhaust.....	57
Figure 3-15: Three-dimensional isometric view of velocity contours and vectors at 1 cm above the ground	58
Figure 3-16: Interior view of the 2D square wide-angle diffuser geometry	59
Figure 3-17: Three-dimensional view of the fluid domain surrounding the fan and diffuser	60
Figure 3-18: Close-up view of the diffuser mesh showing the inflation layers.....	61
Figure 3-19: Three-dimensional view of the interior mesh of the fluid domain surrounding the diffuser and fan	62
Figure 3-20: Velocity contours and vectors inside of the 2D square diffuser	63
Figure 3-21: Pressure contours inside the 2D square diffuser	64
Figure 3-22: Plot of modelled and measured velocity profiles along the centreline of the diffuser exhaust	65
Figure 3-23: Front view of velocity contours and vectors of the impinging diffuser exhausting	66
Figure 3-24: Isometric view of velocity contours and vectors at 1 cm above the ground.....	67
Figure 4-1: Velocity profiles at 30 degree intervals, 2 m radius around the inverted fan	69
Figure 4-2: Velocity profiles at 30 degree intervals, 2 m radius around the 2D square diffuser..	74

Figure 4-3: Top-down view of velocity contours and vectors at 1 cm above the ground for the inverted vacuum fan..... 78

Figure 4-4: Top-down view of velocity contours and vectors at 1 cm above the ground for the 2D square diffuser..... 79

LIST OF TABLES

Table 2-1: List of Diffuser Channel Widths	21
Table 2-2: Manifold Diffuser Outlet Lengths	22
Table 2-3: Height and Air Velocity Requirements of ISO 17962 Standard	25
Table 2-4: Summary of Air Velocity Measurement Uncertainty Analysis	26
Table 2-5: List of Manifold Diffuser Outlet Flow Rates	35
Table 2-6: Summary of the Experimental Measured Velocities.....	36
Table 4-1: Comparison of Experimental and Modelled Velocities for the Inverted Vacuum Fan	72
Table 4-2: Comparison of Experimental and Modelled Velocities for the 2D Square Diffuser ..	76
Table 4-3: Comparison of Velocities of the Inverted Fan and 2D Square Diffuser	77

NOMENCLATURE

Notation

A	Area (m^2)
a	Distance between vanes (m)
C	Centreline
C+	Empirical constant based on surface roughness
dx_i	Percent error in measurement (%)
dz	Total measurement error (%)
f	Vane length (m)
k	Turbulence kinetic energy (m^2/s^2)
L	Diffuser length (m)
\dot{m}	Mass flow rate (kg/s)
N	Fan speed (rev/min)
n	Number of vanes
Q	Flow rate (m^3/s)
R	Range of measurement
Δt	Time step size (s)
u	Fluid velocity (m/s)
u_p	Fluid velocity parallel to a wall (m/s)
u_τ	Friction or shear velocity (m/s)
v	Average fluid velocity (m/s)
w	Diffuser width (m)
w_i	Diffuser inlet width (m)
Δx	Length scale (m)
y_w	Distance from a wall (m)

α	Angle between vanes ($^{\circ}$)
Γ	Empirical constant based on 2θ for optimum vane length
Δ	Error range in measurement
ε	Dissipation rate (m^2/s^3 or W/kg)
2θ	Total divergence angle ($^{\circ}$)
κ	Von Karman constant
ν	Kinematic viscosity (m^2/s)
ρ	Density (kg/m^3)
τ_w	Wall shear stress (Pa)
ω	Specific turbulence dissipation rate (1/s)
ω_a	Angular velocity (rad/s)

Abbreviations

2D	Two dimensional
3D	Three dimensional
CAD	Computer Aided Design
CFL	Courant Friedrichs Lewy number
CFD	Computational Fluid Dynamics
ISO	International Organization for Standardization
RANS	Reynolds Averaged Navier-Stokes
RNG	Renormalisation Group
RPM	Revolutions Per Minute
SIMPLE	Semi-Implicit Method for Pressure-Linked Equations
SISO	Single Inlet Single Outlet
SST	Shear Stress Transport

CHAPTER 1 INTRODUCTION AND LITERATURE REVIEW

1.1 Introduction

In 2015, the ISO 17962:2015 standard came into place to standardize the exhaust emitted by planter vacuum fans. In order for CNH Industrial to meet this new standard, a study of their planter fan exhaust was performed, which is the basis of the research work described in this thesis.

A planter is an agricultural machine used for precision sowing of high value crops, such as corn or soybean, which require seeds to be singulated. This is in contrast to an air seeder that places seed in a furrow based on an average feed rate, which results in a variable amount of seed in close proximity over the length of the furrow. To achieve singulation of the seeds the planter uses a perforated seed disc rotating inside a seed meter to pick individual seeds from a fluidized seed bed to be planted. Figure 1-1 shows the inside of a seed meter assembly with the seed disc removed: Location “A” is the seed meter enclosure, “B” is the agitator which aids in fluidizing the seed bed “C”, “D” is the seed disc, “E” shows the seeds which are covering the perforations along the edge of the seed disc, and “F” is the seed chute by which the seeds leave the seed meter to fall to the ground for planting (CNH Industrial, 2014). On the side of the seed disc opposite from the seed bed, air is removed to create a vacuum through the use of the planter’s vacuum fan. As the seed disc rotates through the seed bed, seeds are attracted to the holes in the disc due to the vacuum that is formed on the opposite side. Once the seeds reach the top of the seed meter, they are knocked off the disc to fall through the seed chute.

A portion of the seed currently being planted has pesticide and herbicide coatings pre-applied. As the seed experiences the above planting process, it is possible for particles of the coating to detach from the seed, get drawn through the vacuum fan, and be exhausted into the atmosphere (Tapparo, et al., 2012). To minimize this effect, ISO (the International Organization for Standardization) has published a standard, ISO 17962:2015 Agricultural machinery -- Equipment for sowing -- Minimization of the environmental effects of fan exhaust from pneumatic systems (International Organization for Standardization, 2015). The exhaust from a vacuum fan can be

shown to comply with the standard in one of two ways. One way is to test the fan, in the field, by injecting dye into its inlet and measuring the concentrations of dye reaching the ground around the planter¹. The other way to show compliance is through a design method. This work focuses on the design method.

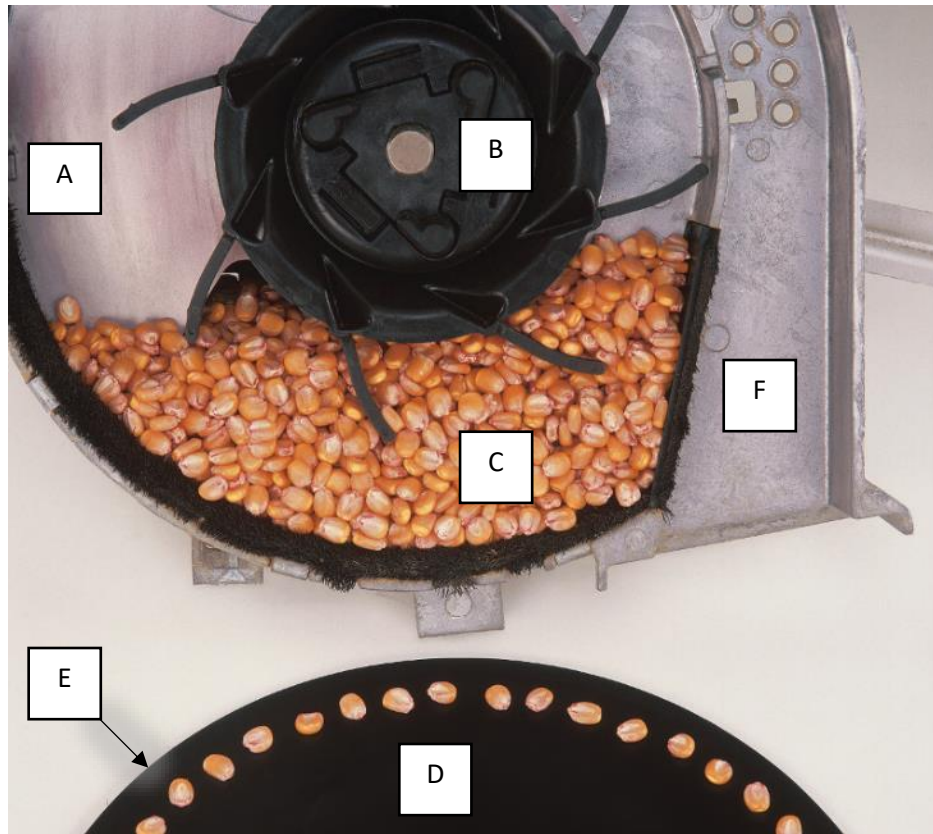


Figure 1-1: Interior of seed meter assembly with filled seed disc (CNH Industrial, 2014)

The design method in the ISO 17962 standard sets forth four requirements that the fan must meet to be deemed compliant:

1. The fan exhaust must point towards the ground;
2. The exhaust must be located between 0.50 m and 1.50 m above the ground;
3. At a 2.00 m radius from the exhaust centerline, the air velocity parallel to the ground must be less than 4.00 m/s, between 0.00 m and 0.25 m above the ground, and less than 2.00 m/s between 0.25 m and 1.50 m above the ground;

¹ This was done by CNH Industrial in a separate internal study.

4. The fan should be tested as it would be configured for work in the field, i.e. as part of the planter and with the fan producing a vacuum in the seed meters.

Also, for planter fan testing to be valid, the cross-wind must be less than a 0.50 m/s.

Figure 1-2 shows a two-dimensional front view of the domain described by the standard. When viewed in three dimensions, this domain is bounded by a cylindrical surface around the fan at which the velocity limits apply.

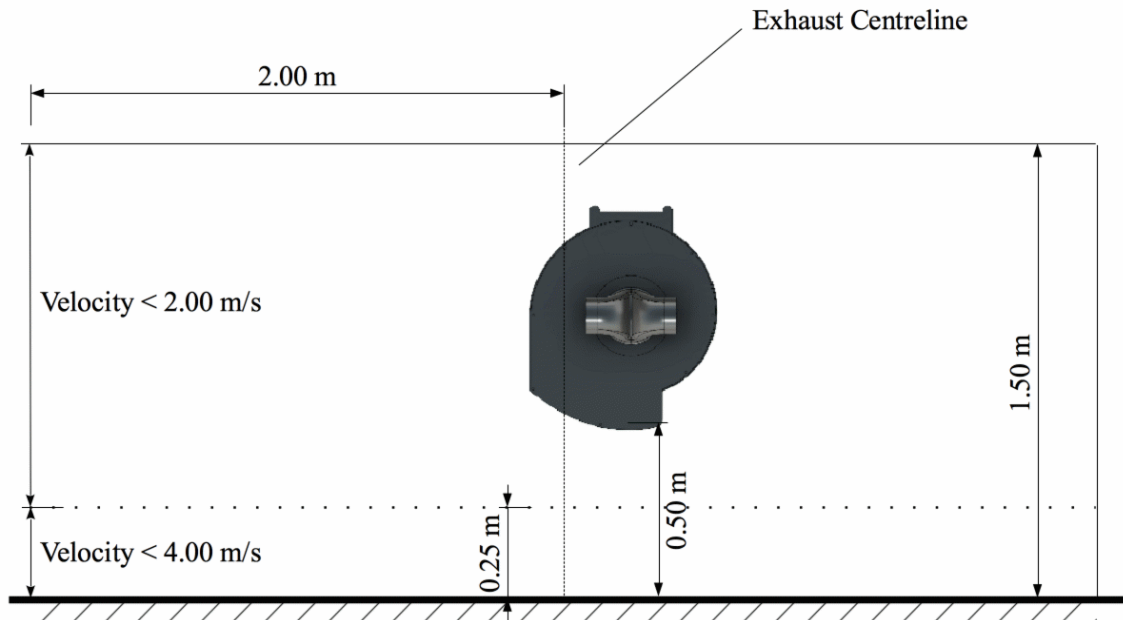


Figure 1-2: Domain area for the design method

1.2 Objectives

This thesis research project has two main objectives:

1. To demonstrate that the vacuum fan on the CaseIH Early Riser™ planter can meet the ISO 17962 standard.
2. To show that a computational fluid dynamics (CFD) simulation, which was not fully validated during this project, can be an effective tool to determine compliance with the ISO standard. A numerical simulation is used where the goal of the model is to determine a high-level solution to the flow within a short period of time and fine details, for example vortex shedding, can be left unresolved.

To achieve the first objective, the fan was tested against the above design criteria by inverting the fan 180° from its present orientation. Currently the fan is oriented on the planter so that it exhausts skyward, and not towards the ground as per the standard. As inverting the fan on models of the CaseIH planter currently in production would require a major redesign of the fan mounting, two diffusers were also tested against the standard. These diffusers were attached to the exhaust of the fan to redirect the exhaust groundward and reduce the exhaust velocity to ensure compliance with the standard. Slowing the exhaust before it reaches the ground has the added benefit of reducing the possible disturbance caused by the exhaust impinging on the ground and minimizing the possibility of dust lift caused by the fan exhaust. In parallel to this work and using the results from achieving this first objective, CNH Industrial developed a new vacuum fan with a modified outlet that exhausts groundward with an integrated diffuser. The new fan is not part of this thesis.

The second objective of this work will be accomplished by modelling the domain around the fan exhaust impinging on the ground, with and without the diffusers present. The results of the simulations will be compared to the experimental results to assess whether that the simulations can be equally effective at demonstrating compliance with the ISO standard as the physical experiments.

1.3 Literature Review

1.3.1 Diffuser Design

The following sections present a review of the literature related to the design and optimization of a diffuser.

A diffuser reduces the fluid velocity by expanding the area of a fluid flow, which partially converts the velocity head of the flow into pressure head in a process known as pressure recovery. The greater the pressure recovery, the better the performance of the diffuser (White, 2011). Figure 1-3 depicts a two-dimensional (2D) wide-angle square diffuser, where c denotes the centerline, L is the diffuser length, w is the initial width of the diffuser, and 2θ is the total divergence angle. The diffuser is said to be 2D since it expands in a single plane. It is defined as

square since the exhaust of the diffuser is in the shape of a square or a rectangle, i.e. the diverging walls meet at 90° to the parallel non-diverging walls.

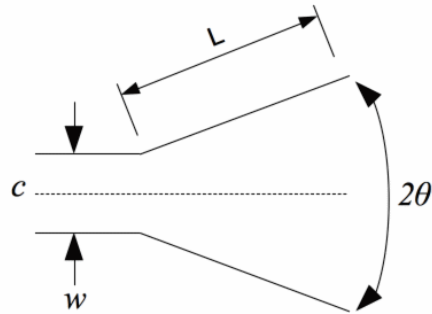


Figure 1-3: 2D wide angle square diffuser

The definitive work on wide-angle 2D square diffusers was performed by Kline in the 1950's and 1960's. Through his research four flow regimes were identified in a diffuser: unseparated flow, transitory stall, fully developed stall along one side of the diffuser, and jet flow (Cochran & Kline, 1958; Morre & Kline, 1958). Optimal performance of a diffuser was found to occur in the unseparated regime. For simple diffusers without vanes, as shown in Figure 1-3, a value of $2\theta = 7^\circ$ was found to maximize pressure recovery and stay within the unseparated flow regime (Kline, et al., 1959).

Kline also studied delaying stall by using vanes, achieving successful delay of stall in diffusers having a value of 2θ from 7° to 42° (Cochran & Kline, 1958). As part of this research a set of guidelines for designing optimal vanes for a 2D square diffuser was developed. The following three equations refer to the vaned diffuser geometry shown in Figure 1-4. First the optimal angle between vanes is determined as follows:

$$\alpha = \frac{2\theta}{n+1} \quad (1-1)$$

where α is the angle ($^\circ$) between the vanes, 2θ is the angle ($^\circ$) of the diffuser exhaust, and n is the number of vanes. The value of n is chosen so that the value of α is as close as possible to 7° . A

second equation is used to determine the optimal spacing between the vanes:

$$a = \frac{w_i}{n+1} \quad (1-2)$$

where a is the space (m) between the vanes, and w_i is the width (m) of the inlet of the diffuser. A third equation determines the optimal length of the vanes as follows:

$$\frac{f}{a} = \Gamma \quad (1-3)$$

where f is the length (m) of the vane, and Γ is an empirical value that is a function of 2θ . When 2θ equals 7° , Γ is equal to 17 (Morre & Kline, 1958).

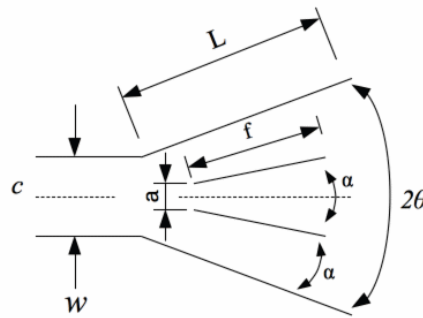


Figure 1-4: 2D wide angle square diffuser with vanes

Another method of influencing diffuser performance is to change the shape of the diffuser walls. Carlson et al. (1967) studied this by comparing the pressure recovery of trumpet-shaped and bell-shaped diffusers (Figure 1-5) to that of a straight-walled diffuser. They found that a bell-shaped diffuser could outperform the equivalent straight-walled diffuser, while a trumpet-shaped diffuser under-performed. However, the performance increase of the bell-shaped walls was on the order of 3% to 4%, and in most cases, would not warrant the increased cost of construction (Carlson, et al., 1967). Later through the use of CFD simulations and computer controlled optimisation, the optimum family of shapes for a diffuser's walls was found to be a combination of a bell and trumpet, i.e. a bell shape near the inlet transitioning to a trumpet shape at the

exhaust (Madsen, et al., 2000). Again, the increase in pressure recovery was minimal compared to a straight-walled diffuser.

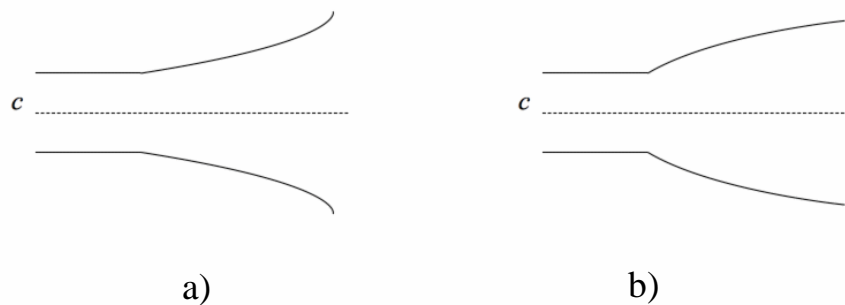


Figure 1-5: Trumpet-shaped diffuser (a), bell-shaped diffuser (b)

Aside from vanes and curving the diffuser walls, there exist a number of additional ways to delay stall in a diffuser. These can be divided into passive or active measures. Examples of passive measures of delaying stall include: boundary layer fences (Sullerey, et al., 2002), vortex generators (Paul, et al., 2013; Sullerey, et al., 2002), J grooves (Kurokawa, et al., 2010), riblets (Reagan, 1990) and vanes (Cochran & Kline, 1958; Chong, et al., 2008; Morre & Kline, 1958). Overall, vanes were shown to be the most effective method for delaying stall. An example of an active measure is using boundary suction on the walls of the diffuser to keep the boundary layer from separating (Hummad & Jadallah, 2007). Suction is achieved by perforating the walls of the diffuser and drawing air out through these holes. Hummad and Jadallah (2007) observed a 35% increase in pressure recovery, compared to the same diffuser without perforated holes and suction. However, this method of delaying stall adds significant cost to the construction of a diffuser.

The shape of a diffuser does not necessarily need to follow a single inlet, single outlet design. Wye (Y) or tee (T) shaped diffusers (Gopaliya & Chaudhary, 2010) take a single inlet and divide it into two branches whose total exit area is greater than the area of the inlet. They have similar performance to straight-walled diffusers. The idea of multiple exhausts can be extended beyond two outlets. For example, the use of a diffuser with multiple exhausts has been proposed to

suppress blowing dust from an agricultural combine (Patent No. US8313362 B2, 2012).

Therefore, it should be possible to create a manifold diffuser where one inlet branches into many outlets, each exhausting only a fraction of the flow entering the inlet, with a lower velocity.

The above literature review identifies two types of diffuser, a traditional single inlet single outlet (SISO) expanding area diffuser and a manifold diffuser. For a SISO expanding area diffuser a 2D straight-walled square diffuser provides the best pressure recovery relative to manufacturing effort. While the effectiveness of a straight-walled diffuser is maximized at an opening angle of 7° , by implementing equations 1.1 to 1.3 and designing a diffuser that uses vanes to effectively divide a larger angled opening into multiple 7° diffusers, a diffuser with up to a 42° opening angle can be made to work. For a manifold diffuser, single inlet with two outlet diffusers have been shown to work effectively, however increasing to more outlets may be more effective, which will be further investigated as a part of this work.

1.3.2 CFD

The following section outlines the knowledge base that was consulted to create a successful CFD model of the vacuum fan. A number of factors must be considered when modelling a centrifugal fan. The geometry of the fan is complex, it has both stationary parts, such as the front and back casing, and a rotating part, the impeller. Figure 1-6 shows a centrifugal fan with its main components labeled. It is essential to properly model the interaction between the stationary and rotating components to correctly model the flow through the fan.

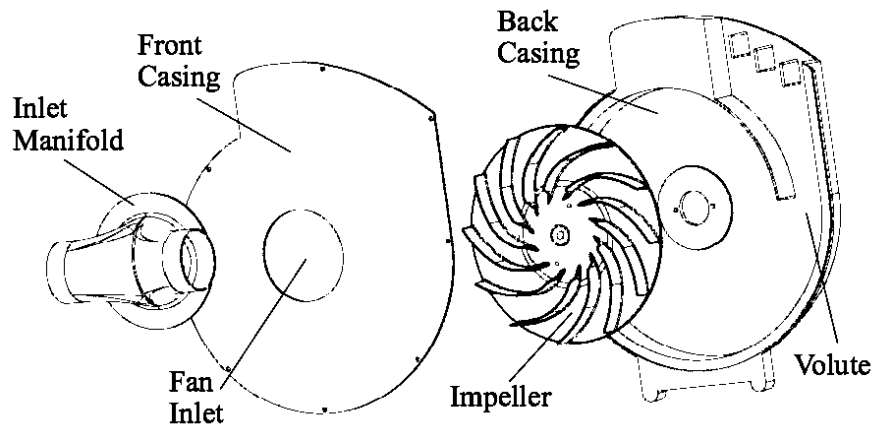


Figure 1-6: Exploded view of fan

To accomplish this, the entire fluid domain of the fan must be correctly discretized or meshed so as to capture the important internal features of the fan. Next it must be decided whether to use a steady state or transient solution to model the interaction between the impeller and the fluid in the fan. Also, an effective model for turbulence must be chosen, and the appropriate boundary conditions set. Finally, a CFD code or program must be chosen to calculate the solution to the fluid flow model (Gülich, 2010). A sample of studies illustrating the methods used to create a viable CFD model is given below. Models for both centrifugal fans and pumps were consulted as the machinery in both cases is similar, with the sole difference being the phase of the fluid. For reference a pump refers to a device that is used for liquids and a fan is a device that performs work on gases (Moran & Shapiro, 2008).

Dick et al. (2001) compared two steady state solution methods and a transient solution method for modelling flow through a pump to determine which method gave the most realistic results. The steady state methods were the frozen rotor and mixing plane methods, and the transient method was the sliding mesh method. The three solution methods are described as follows:

- 1) Frozen Rotor: Over the course of the simulation the impeller is kept at a fixed/frozen position relative to the volute/casing. To solve the flow, two volumes are defined, one comprising the mesh around the impeller and the other comprising the remainder of the domain. A rotating reference frame is defined for the impeller volume and a stationary or absolute reference frame is defined for everything else. The governing equations for the flow around the impeller are solved in the rotating reference frame. This translates the fluid velocities at the impeller inlet into the relative rotating frame of reference and imposes an angular velocity component on the flow. The flow in the casing/volute is solved in the absolute reference frame. The two frames of reference are coupled using continuity. Since the rotor is frozen relative to the rest of the fan, the solution found by this method is based solely on the single impeller position. In other words, only the mathematical domain around the impeller is rotating, and the mesh never changes.
- 2) Mixing Plane: This method uses the same relative and absolute reference frames as the frozen rotor method to impose an angular velocity component on the flow. However, to couple the solutions in the two reference frames, the flow variables at the interface between the two reference frames are circumferentially averaged. Since the flow is

averaged when coupling the two reference frames, this method provides a solution that is independent of relative position between impeller and volute.

- 3) Sliding Mesh: In the sliding mesh method, the motion of the impeller rotating is directly modelled, while the mesh of the rest of the fan is held stationary. This results in a time dependent or transient solution to the model. At each time step the fluxes between the two meshes are solved on the common sliding surface.

As for the results of the study, they found “steady state methods useless for general performance prediction” as they are prone to produce erroneous results. This is because steady state methods have trouble accurately predicting how the fluid leaves the impeller blades. The sliding mesh transient method was found to be superior at accurately predicting the flow field inside the pump. The model used for this study had an unstructured mesh, with 500,000 cells. Turbulence was modelled using the realizable $k-\varepsilon$ turbulence model. The CFD program ANSYS Fluent™ was used to run the model (Dick, et al., 2001).

Gonzalez et al. (2002) used a CFD simulation of a centrifugal pump to study the interactions between the pump’s volute and impeller. They found that an unstructured mesh gave less skewness² and better convergence when compared to a structured mesh due to the complex geometry inside the pump. To ensure the proper fluid interaction between the volute and impeller a transient solution, using the sliding mesh method, was used. A time step of 1.47×10^{-4} s was used with the impeller rotating at 1600 RPM, giving 252 time steps per revolution. To model turbulence the standard $k-\varepsilon$ model with log-law wall functions was implemented. The CFD program Fluent was used to run the model (Gonzalez, et al., 2002).

Majidi (2005) created a CFD model to study the unsteadiness of the flow inside a centrifugal pump. Unlike Gonzalez et al. (2002), Majidi (2005) used a structured mesh, instead of unstructured, which consisted of 833,000 cells. The model was transient, using the sliding mesh method, with a time step of 2.0243×10^{-4} s, which gave 200 steps per revolution of the impeller. The model simulated a total of five impeller revolutions. The turbulence in the pump was modelled using the standard $k-\varepsilon$ model with log-law wall functions. The CFD program ANSYS CFX™ was used to run the model. It was found that the unsteady flow field in between each

² Skewness is defined in section 3.2.

impeller blade followed a periodic pattern, with the flow rate through the individual blade passages increasing and decreasing as the impeller rotated. Once the flow reached the pump outlet, the unsteady flow through the individual blade passages combined to produce a steady, constant, flow rate through the pump outlet (Majidi, 2005).

Gjernes (2014), simulated a centrifugal slurry pump with the goal of optimizing the shape of the impeller blades. The model used an unstructured mesh, as a structured one was unable to properly capture the complex geometry of the interior of the pump. The mesh of the pump had 5.8 million cells, with a minimum cell size of 6 mm. Turbulence was modelled using the SST $k-\omega$ turbulence model. The rotation of the impeller was simulated using the transient sliding mesh method, the impeller was set to rotate at a rate of 3° per time step. This time step size was found using $t_{\text{step}} = 10/\omega_a$, where ω_a is the angular velocity, in rad/s, of the impeller. A total of three rotations of the impeller were simulated. Initially a steady state solution of the model was attempted, using the frozen rotor method. It was found that it was difficult to achieve convergence with the frozen rotor method, and that results did not compare well to experimental data. This was due to the fact that the frozen rotor method was unable to account for the inherent unsteadiness of the flow through the pump. The CFD program CFXTM was used to run the model (Gjernes, 2014).

Petit and Nilsson (2013), performed a comparison study, using OpenFOAM®, of the frozen rotor and sliding mesh solution methods, in addition to comparing the performance of four turbulence models, the standard $k-\varepsilon$ model, the realizable $k-\varepsilon$ model, the RNG $k-\varepsilon$ model, and the SST $k-\omega$ model³ for a centrifugal pump. The pump model in this study consisted of a structured mesh of 2 million cells. All of the turbulence models made use of log-law wall functions, and the SIMPLE method was used to couple the pressure and velocity field. SIMPLE (Semi-Implicit Method for Pressure-Linked Equations) is an algorithm that takes advantage of the fact that CFD models the solution to a flow iteratively and couples the velocity field and pressure by initially solving for the velocity field by using the pressure distribution from the previous solution iteration. It then solves for the pressure in the current iteration of the solution and corrects the initial velocity solution with the new pressure distribution. For each of the tests a time step of 7×10^{-5} s was used, which meant that the impeller was rotated at 0.84° per time step. This time step length was

³ The various turbulence models are defined in section 3.2.

determined using a Courant number of 6. The Courant number is a ratio of time step size and the characteristic velocity of the model, to the cell size. Lower values of the Courant number result in less variation in the modelled solution from one time step to the next, which allows subsequent time steps to converge with fewer iterations. In comparing the frozen rotor to the sliding mesh method, it was found that the sliding mesh results were in better agreement with experimental results. The frozen rotor method predicted the wakes from the impeller blades suddenly changing direction when passing from the relative to the absolute reference frame. This occurred because the wakes tended to follow the local streamlines, which is an un-realistic phenomenon. This led to only the sliding mesh method being used to compare the turbulence methods. When comparing the results of the different turbulence models, it was found that, while each model gave slightly different results, each obtained a similar accuracy when compared to the experimental results. Overall, the realizable k - ϵ model was found to do a slightly better job at resolving the flow features when compared to the experimental data (Petit & Nilsson, 2013).

Liu et al. (2006), used CFD models to predict the noise field from a centrifugal fan. The unstructured mesh of the fan consisted of 500,000 cells. The sliding mesh method was used to model the rotation of the fan impeller. Turbulence was modelled using the RNG k - ϵ model with log-law wall functions. SIMPLEC was used to couple the pressure and velocity fields. When determining the time step size, the Courant number was kept to a value of less than 2. This resulted in a time step of 5.747×10^{-5} s. Since the impeller was rotating at 2900 RPM this meant that the mesh of the impeller was rotated at 1° per time step, or 360 steps per revolution of the impeller. The CFD program Fluent was used to run the model (Liu, et al., 2006).

The above literature review suggests the following characteristics for successful simulation of a centrifugal fan or pump:

- 1) The mesh of the fan should be unstructured and on the order of a million cells would be required to adequately model the complex geometry of the fan.
- 2) A transient solution will provide a more accurate simulation of the fan compared to a steady state solution, as a steady state solution cannot resolve the inherently unsteady flow around the impeller. This means that the sliding mesh method should be implemented to model the motion of the impeller.

- 3) The Courant number can be used to define the time step of the transient simulation, with the average time step on the order of approximately 1° of rotation per step.
- 4) To model turbulence, the realizable $k-\varepsilon$ turbulence model, in conjunction with log-law wall functions, is a valid choice and has been successfully implemented, in a number of fan models.
- 5) The choice of CFD program is not critical as ANSYS CFX™, ANSYS Fluent™, and OpenFOAM® have all successfully calculated the solutions of a fan model. ANSYS Fluent™, was utilized for this work, as it was provided by CNH Industrial.

1.4 Organization of Thesis

The remainder of this thesis is comprised of five chapters. Chapter 2 presents the experimental work, documenting how the CaseIH vacuum fan and two diffusers can comply with the ISO 17962 standard. A description of the experiment and its results will be presented. Chapter 3 presents CFD models of the fan and one of the diffusers, along with the results from those models. Chapter 4 compares the results of the experimental and computational studies to assess whether CFD can be an effective tool in showing compliance with the ISO 17962 standard. Finally, Chapter 5 presents the conclusions of this work and highlights areas for future research and improvement.

CHAPTER 2 EXPERIMENTAL MEASUREMENTS

2.1 Introduction

This chapter will document the methodology and design of the experimental part of this work. Three configurations were tested against the ISO 17962 standard: the vacuum fan, the vacuum fan with an in-plane 2D wide-angle diffuser, and the vacuum fan with a linear manifold diffuser. Results and a brief discussion of the results will be presented for the measurements of the velocity field around each of the configurations.

2.2 Air Velocity Measurement

In order to be able to perform the air velocity measurements around the fan in a repeatable and robust manner, a frame was built to position a hot-film anemometer at various locations. Figure 2-1 shows the frame, which consists of steel supports and an arm capable of rotating horizontally in a 2 m radius about the centre of the supports. A protractor was mounted to the frame to measure the angle of the arm relative to the support structure, and ensure consistent positioning of the arm within an error of $\pm 0.5^\circ$. Consistent placement of the anemometer relative to the ground was achieved by mounting eight cylindrical steel supports on the arm for holding the anemometer (Figure 2-2). This configuration allowed air flow velocities to be measured at: 10 cm, 20 cm, 30 cm, 40 cm, 50 cm, 100 cm, 150 cm, and 200 cm above the ground, with an error of ± 0.1 cm, at any point along a 2 m radius from the fan. A model TSI 8455 digital Air Velocity Transducer was used for all of the air velocity measurements. This transducer has a measurement error of the larger of 2% or 0.5% of the full range of air velocity (from 0.0 m/s to 4.00 m/s). A sampling rate of 10 Hz with a 5 s average was used. The anemometer measures velocity in a single plane based on the orientation of the probe. Therefore, only horizontal air velocities were measured. A small flag was placed on the end of the anemometer probe to indicate if the movement of the air was in the direction away from the fan. The flag was very light, to not disrupt the air flow and had no impact of the measurements of air velocities. The anemometer was supplied by CNH Industrial, who calibrate it twice yearly using wind tunnel tests.

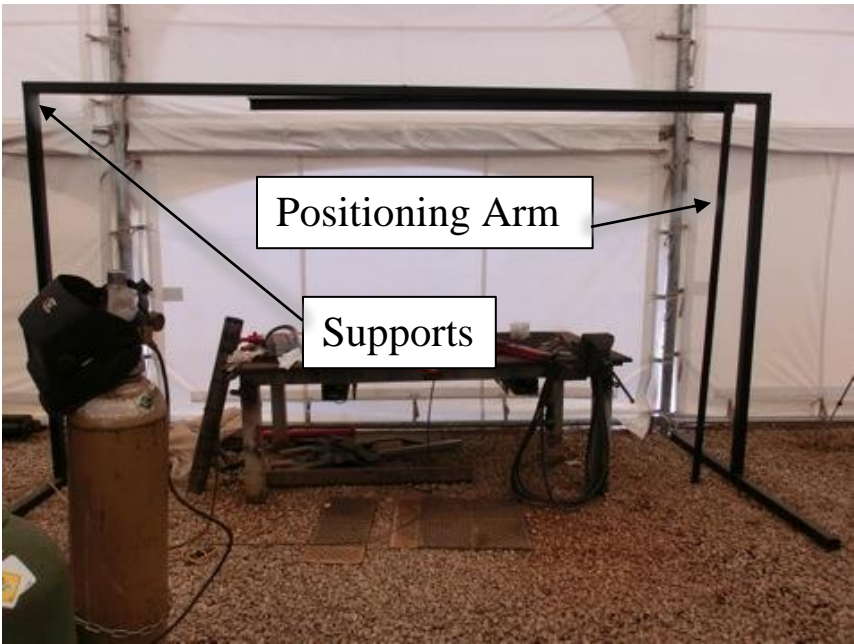


Figure 2-1: Measurement frame

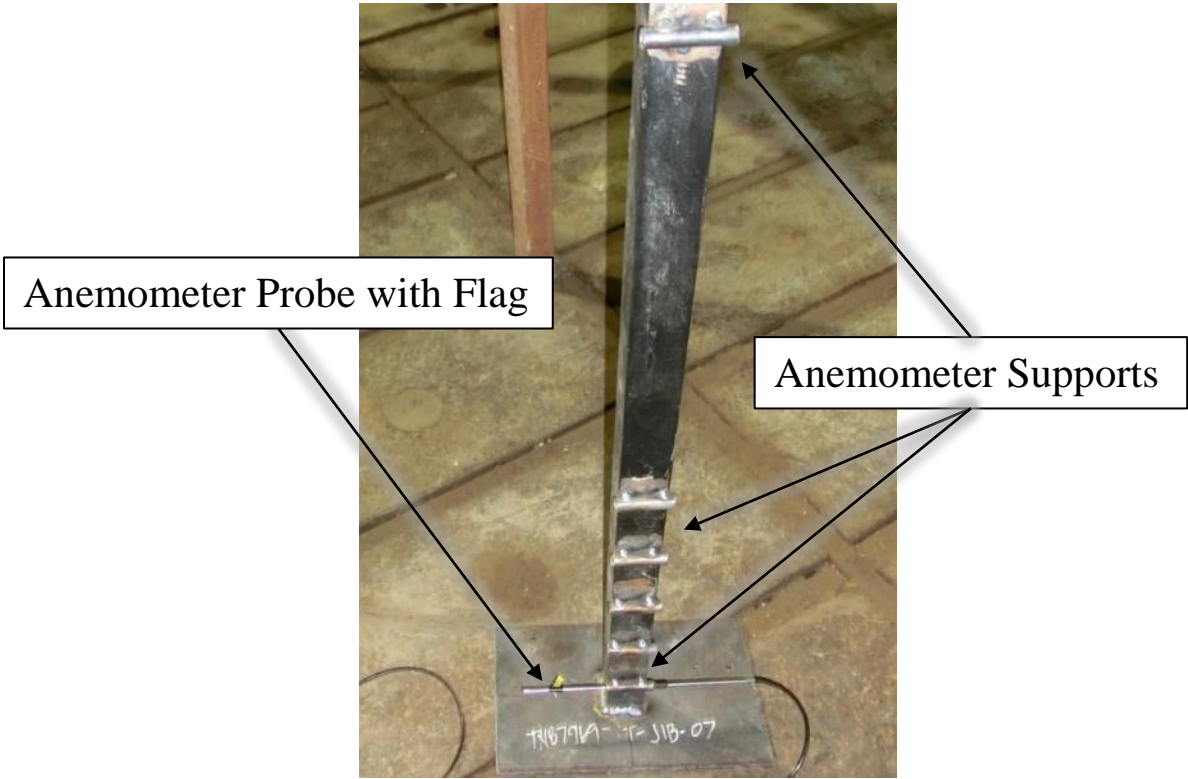


Figure 2-2: Supports for hot film anemometer

It should be noted that there are two reasons that it was not possible to perform measurements of the air velocity of the fan exhaust while the fan was mounted on the planter. The first reason was that the fan (in its production configuration) is mounted on the planter so that its exhaust is directed upwards, not down towards the ground as stipulated in the ISO standard. The second reason was that it would not have been possible to take measurements for a full 360° around the exhaust of the fan, due to physical interferences of the surrounding planter structure. Figure 2-3 shows how the planter would make most measurement points around the fan inaccessible.



Figure 2-3: Interaction between measurement frame and planter

In order to take the required measurements, the vacuum fan was removed from the planter and attached to a test bench. The test bench consisted of a stand to mount the fan. Six seed meters were connected in parallel (with 30 in / 76.2 cm of spacing between them) to the fan, but they were located outside of the space surrounding the fan. Removing the fan from the planter has the added benefit of minimizing obstructions in the flow path of the fan exhaust, allowing for a more rigorous measurement against the standard. It is presumed that if the fan can meet the standard without the planter obstructing the flow and slowing it, then it will still meet the standard when the fan is replaced upon the planter. Blank (un-perforated) seed discs, as shown in Figure 2-4, were placed inside the seed meters to simulate the meters being filled with seed, which allowed the fan to produce a vacuum. A vacuum of 4.98 kPa is required for corn seeds to adhere to a seed disc, which is specified in the manufacturer's operating manual. Vacuum was measured using a vacuum gauge that is supplied with the fan, it has an error of ± 0.3 kPa. To achieve this level of vacuum the fan impeller was required to rotate at approximately 3500 RPM for all tests. A Power Fist Digital Tachometer was used to measure the rotational speed of the impeller, it has an error of 0.5%. The test bench was set up indoors to ensure that the velocity of the ambient air around the fan did not exceed 0.5 m/s as specified in the ISO standard.



Figure 2-4: Blank (un-perforated) seed disc to simulate seed disc filled with corn seeds

2.3 The Experimental Configurations

2.3.1 Configuration 1: Inverted Vacuum Fan

The first configuration tested consisted of only the vacuum fan. This fan configuration will be used as a baseline to measure the effectiveness of the diffusers in the other two configurations. This configuration, depicted in Figure 2-5, consisted of the fan, attached to a frame, with its exhaust pointed towards the ground.

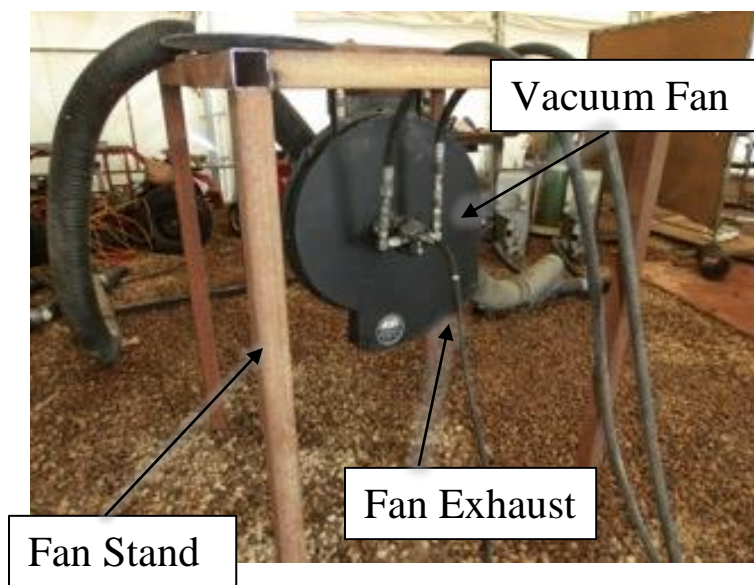


Figure 2-5: Configuration 1 inverted vacuum fan

Measurements of the exhaust air velocity were taken at 30° intervals around the fan at heights of 10 cm, 20 cm, 30 cm, 40 cm, 50 cm, 100 cm, and 150 cm above the ground at a 2 m radius.

Figure 2-6 shows how the measurement locations 0° , 90° , 180° , 270° are located relative to the fan for configuration 1. To achieve 4.98 kPa of vacuum the fan impeller was rotated at 3500 RPM.

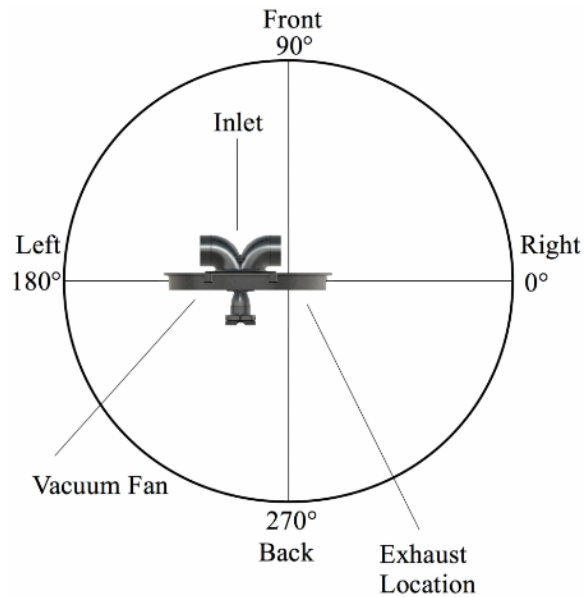


Figure 2-6: Top-down view of measurement locations for configuration 1 with exhaust pointed into the page

2.3.2 Configuration 2: Fan with 2D Square Wide-Angle Diffuser

This configuration consisted of a 2D square wide-angle diffuser attached to the exhaust of the fan. Figure 2-7 shows the set-up of this configuration. The diffuser was designed to be retrofitted to the existing planters so any planter in the family of planters could meet the ISO 17962 standard. The diffuser redirects the exhaust downwards toward the ground.

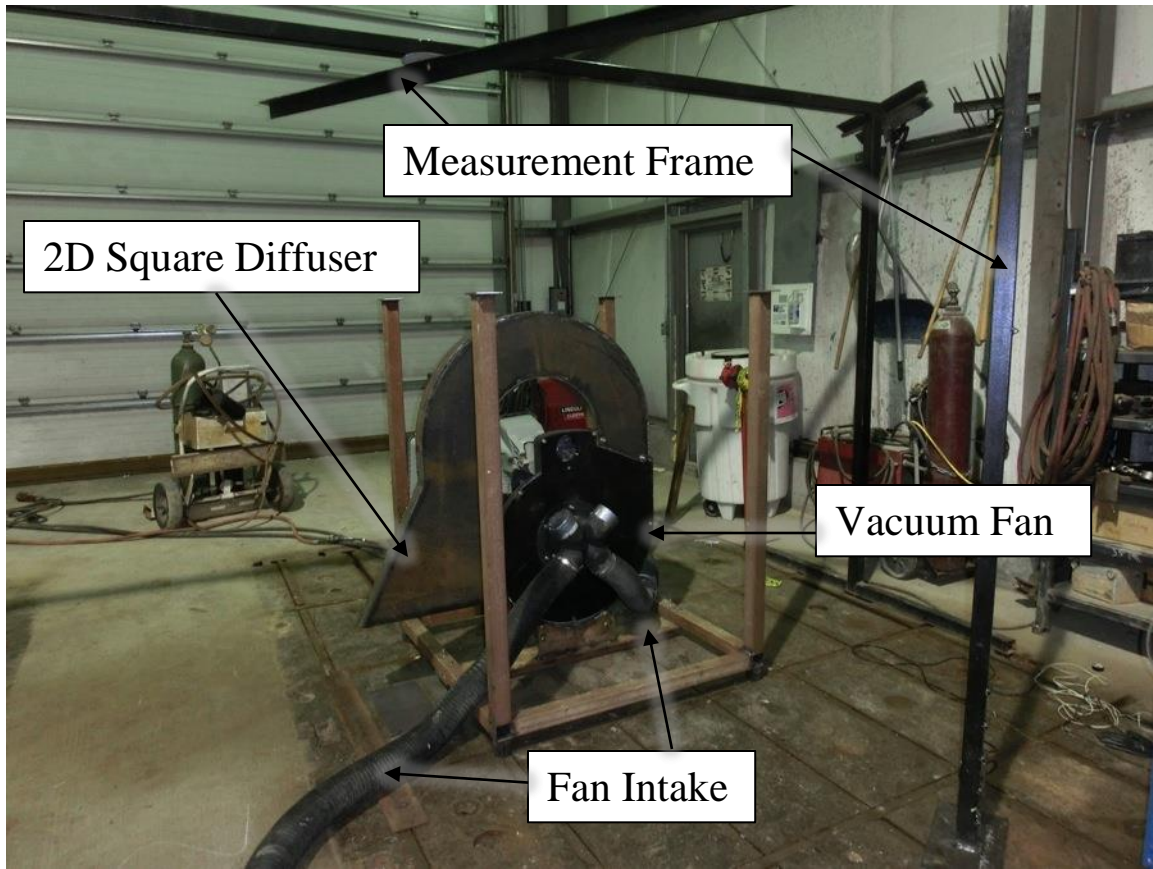


Figure 2-7: Configuration 2 fan with 2D square wide-angle diffuser

Figure 2-8 shows the internal geometry of the diffuser. Inside the diffuser are four vanes: one vane to aid in turning the fan exhaust and the other three vanes to ensure that there is no stall in the expanding section of the diffuser (Cochran & Kline, 1958). The diffuser expands the inlet area from 177 cm^2 to 389 cm^2 . The angle between the vanes is 7° . The turning vane was added based on the research of Lou and Razinsky (2009). They found that a turning vane placed in the centre of a duct will reduce flow separation in the bend and lead to a more evenly distributed flow downstream of the bend. Table 2-1 lists the width of the inlets and outlets for each of the diffuser channels.

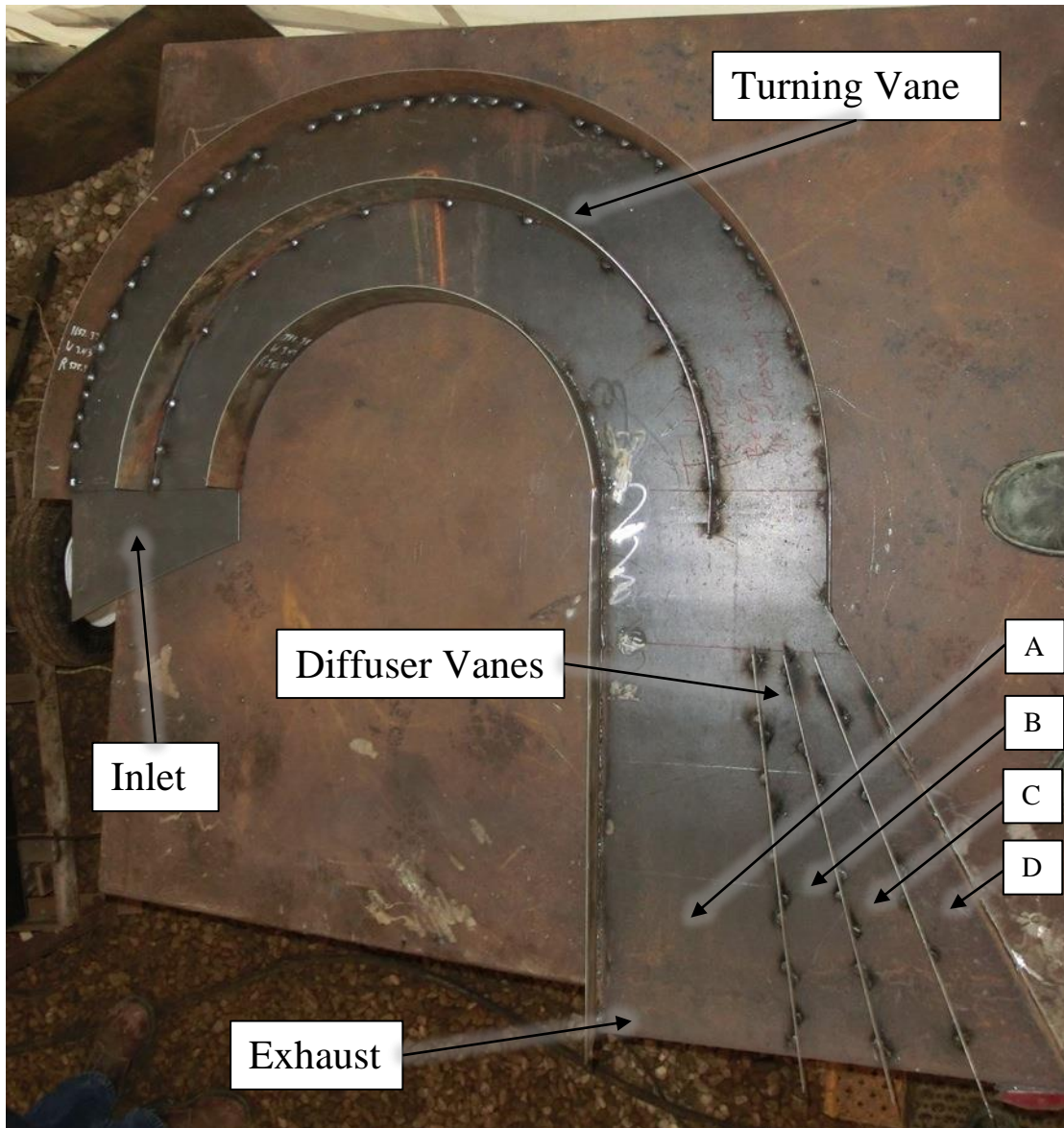


Figure 2-8: Top-down view of 2D square wide-angle diffuser internal geometry

Table 2-1: List of Diffuser Channel Widths

	Inlet Width [cm]	Outlet Width [cm]
Channel A	18.6	24.6
Channel B	3.5	9.7
Channel C	3.5	10.0
Channel D	4.8	12.0

Measurements of the exhaust air velocity were taken every 30° around the exhaust of the diffuser at heights of 10 cm, 20 cm, 30 cm, 40 cm, 50 cm, 100 cm, and 150 cm above the ground. All measurements were made at a 2 m radius from the exhaust. The measurement locations are equivalent to those for configuration 1. To achieve 4.98 kPa of vacuum, for this configuration, the fan was rotated at 3300 RPM.

2.3.3 Configuration 3: Fan with Manifold Diffuser

This configuration consists of the fan and a manifold diffuser attached to the exhaust of the fan. Figure 2-9 shows the set-up for this configuration. The manifold diffuser design exhausts the air gradually over a larger outlet area similar to the method described in a patent owned by CNH Industrial (Patent No. US8313362 B2, 2012). Rather than using a single outlet like the 2D square diffuser to create an increase in area to decelerate the flow, the increased outlet area is divided over multiple outlets. The manifold diffuser consists of six outlets along its length and one outlet at the end with a damper. The damper has a round plate that can be used to vary the open area at the end of the diffuser. The size of each of the six outlets was calculated so that the pressure drop from the fan exhaust to each outlet was equal, which would evenly divide the flow between all the outlets (Mott, 2005). Each outlet is 10 cm deep and 10 cm wide with outlet lengths listed in Table 2-2. The damper was set to 60° to better balance the pressure drops. The body of the diffuser was made of flexible 200 mm diameter ribbed plastic tubing and was supported by square steel tubing and a stool. It was attached to the fan with a 90° elbow. In the field, the body of the diffuser would be supported by the frame of the planter. Figure 2-10 shows a close-up view of the outlets in the manifold diffuser.

Table 2-2: Manifold Diffuser Outlet Lengths

	Length [cm]
Outlet 1	19
Outlet 2	17
Outlet 3	15
Outlet 4	22
Outlet 5	12
Outlet 6	14

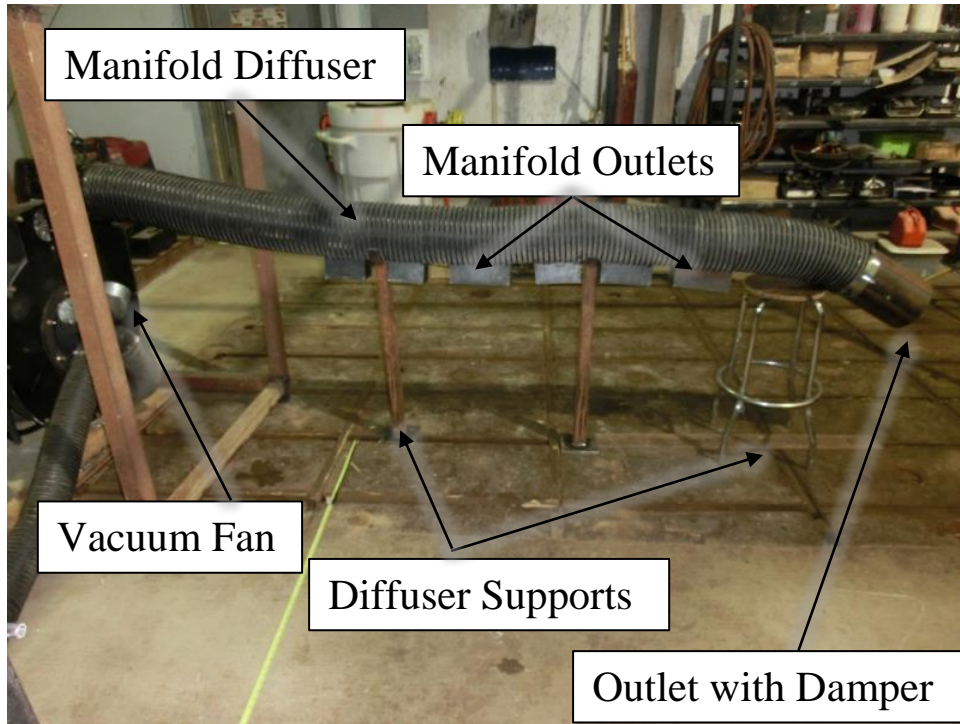


Figure 2-9: Fan with manifold diffuser



Figure 2-10: Bottom up view of manifold diffuser showing the multiple outlets

As the ISO standard did not directly address how to test a fan with multiple exhaust points a new methodology was developed based on the intent of the standard. To determine the measurement points for this configuration a 2 m radius circle was drawn centred on each outlet. Figure 2-11 shows how the perimeter of these overlapping circles creates a stadium shape, as shown in red. A stadium is a two-dimensional shape formed by two semi-circles connected by two straight parallel lines.

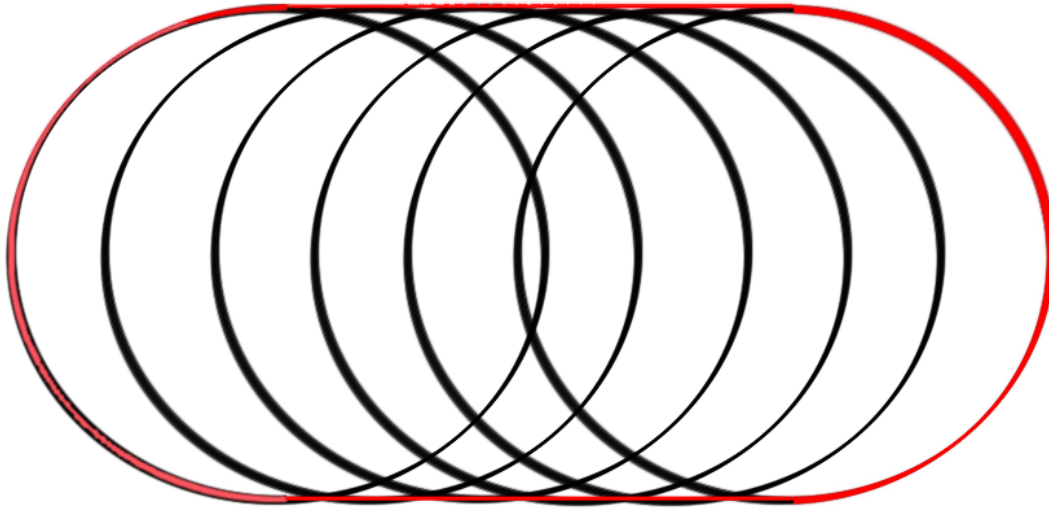


Figure 2-11: Illustration of how overlapping circles create a stadium shape

Using the stadium as a reference the measurement locations can be determined, such that they are equivalent to the intent of the ISO standard methodology. Figure 2-12 shows the measurement points chosen relative to the manifold diffuser and fan. Basing the measurement points off the stadium shape adds six measurement locations in addition to the previous configurations. They are located along the straight sections at 40 cm intervals, three on each side. To achieve 4.98 kPa of vacuum, for this configuration, the fan impeller was rotated at 3300 RPM.

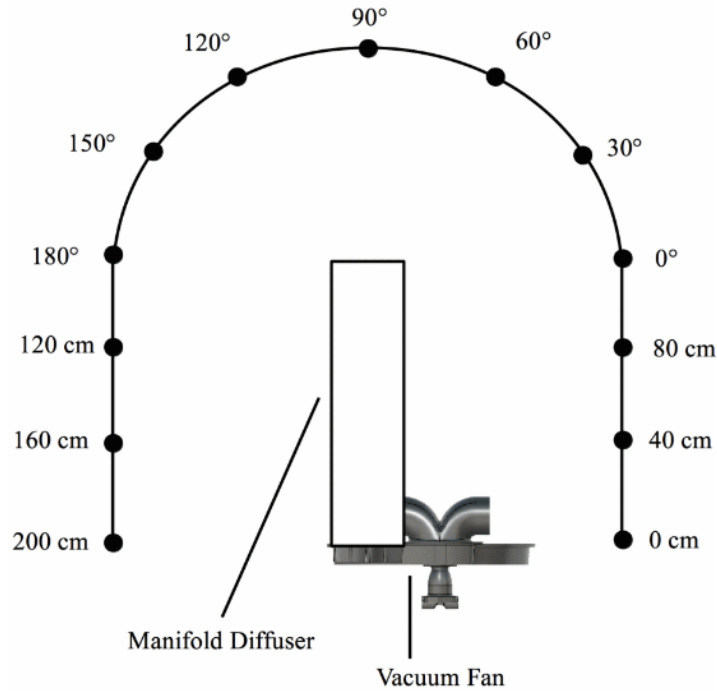


Figure 2-12: Top-down view of measurement points for the manifold diffuser

2.4 Results

The following section presents the results of the experimental measurements taken for each of the three configurations. As a reference, Table 2-3 lists the velocity requirements to meet the ISO standard.

Table 2-3: Height and Air Velocity Requirements of ISO 17962 Standard

Height above Ground [m]	Maximum Air Speed [m/s]
0 - 0.25	4.0
0.25 - 1.5	2.0

Before presenting the experimental results, as the data was measured experimentally the uncertainty in the measurements must be quantified and presented. Table 2-4 is a summary of the uncertainty for the experimental measurements. There are six sources that contribute to the experimental uncertainty, the measured angle of the positioning arm, the measured elevation of

the probe, the horizontal alignment of the probe, the anemometer error, the vacuum gauge error, and the error in the tachometer measurement.

Table 2-4: Summary of Air Velocity Measurement Uncertainty Analysis

Error Source	Error	Range	%
Location of Positioning Arm for Air Velocity Measurement [°]	1°	360°	0.3%
Horizontal Probe Alignment [°]	1°	180°	0.6%
Hot-film Anemometer [%]	-	2%	2.0%
Vacuum Fan Static Pressure Gauge [kPa]	0.3	5.0	6.0%
Fan Speed Tachometer [RPM]	-	0.5%	0.5%
Measurement Elevation [mm]	5	100 to 1500	0.3% to 5%

2.4.1 Experimental Data from the Three Configurations

The exhaust from the fan and diffusers can be compared to air jets impinging on the ground. From previous research conducted by Wolfshtein (1970), when an ideal round jet reaches and impinges on the ground, the flow should spread out equally in all directions with the majority of the flow concentrated near the ground, creating a wall jet. Therefore, when observing the velocity profile in any vertical plane, measured radially around the jet, the velocity magnitude should be highest near the ground and then quickly decrease as the height from the ground increases. Also, for a symmetric jet, the velocity profile should be identical in every vertical plane. Plotted in Figure 2-13 are profiles of the horizontal velocity measured at a 2 m radius around each of the three configurations. Error bars on the measurements are, for most measurements, smaller than the points on the plots due to the scale and are therefore not shown. The measurement locations for configuration 1 (inverted vacuum fan) and configuration 2 (2D square diffuser) are shown in Figure 2-6. The measurement locations for configuration 3 (manifold diffuser) are shown in Figure 2-12. Plots *a* through *g* show data for all three configurations, plots *h* through *l* show data solely for configurations 1 and 2, and plot *m* shows data for the straight sections along stadium shaped perimeter around the manifold diffuser. The coloured lines on the plots are used to identify data sets and not to imply a continuous velocity profile, since only a finite set of discrete measurements was performed.

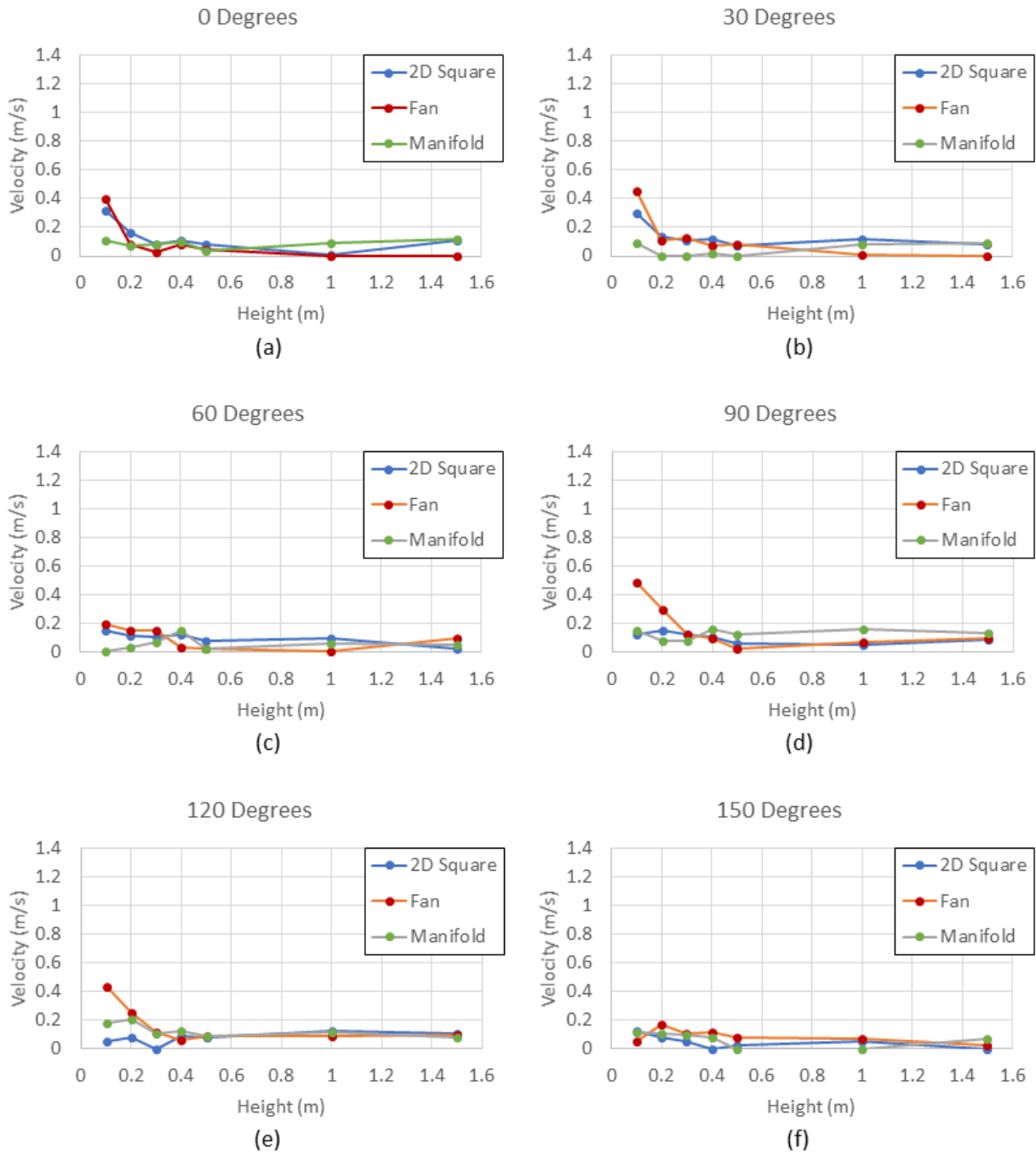


Figure 2-13.1: Horizontal velocity profiles for configurations 1, 2 and 3 ranging from location 0° to location 150°

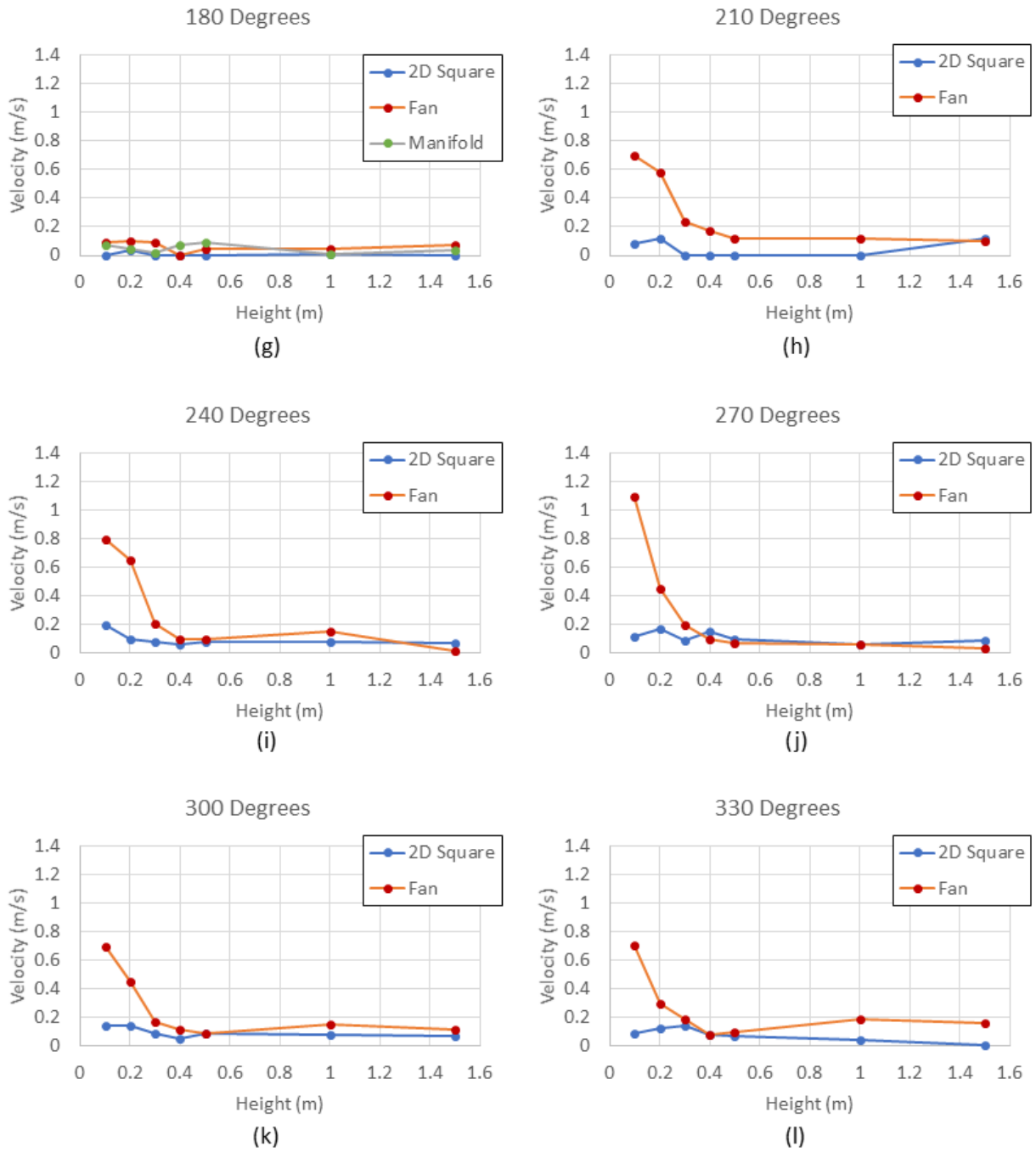


Figure 2-13.2: Horizontal velocity profiles for configurations 1, 2 and 3 ranging from location 180° to location 330°

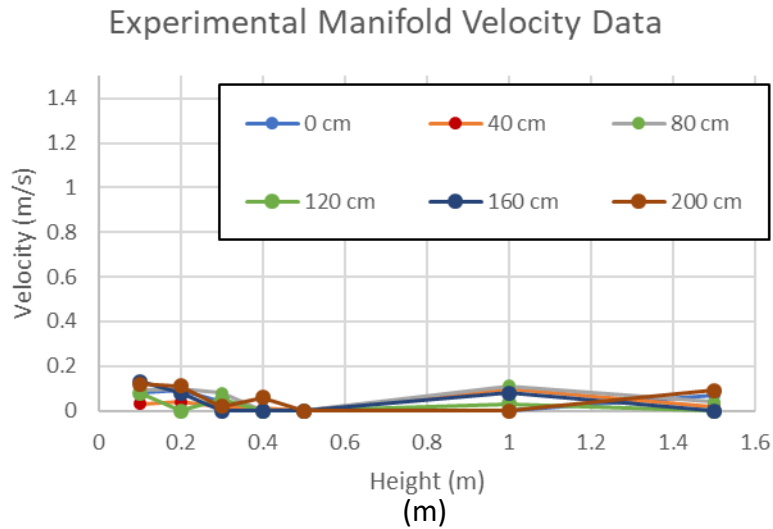


Figure 2-13.3: Horizontal velocity profiles for straight sections around configuration 3

Comparing the measurements for the fan to the measurements for the diffusers, shows that the velocities of the inverted fan are in general consistently higher, indicating that both diffusers are effectively decelerating the fan exhaust. Also, for all three configurations and at every measurement location, the highest velocities measured occurred near the ground and decreased sharply as the measurement elevation increased, as would be expected for an impinging jet. However, the profiles varied greatly depending on the azimuthal measurement location, which is an indication of a non-uniform spreading of the flow following the impingement of the initial jets.

One reason for the variation in the velocity profiles is that the exhausts of the fan and diffusers are not ideal round jets, and as such do not spread out equally along the ground plane after impinging. This behaviour is partially due to the jet and diffuser exit exhaust patterns, which are discussed below.

Figure 2-14 shows the velocity profile along the centreline of the outlet of the inverted fan. Measurements were taken at 1 cm intervals along the outlet centreline using the TSI 8455 digital Air Velocity Transducer. The regions of reduced momentum in the velocity profile at 6 cm, 13 cm, and 20 cm are caused by the vanes located in the fan's volute as shown in Figure 2-15. This asymmetric profile, with the peak velocity occurring between 20 cm and 25 cm, is due to the geometry of the fan casing. After the flow enters the fan and passes through the impeller blade

passages, it encounters the curved fan casing. The casing walls redirect the flow through the volute and towards the outlet. Once the flow enters the volute, it begins to decelerate as the cross-section area expands. The majority of the flow continues to follow the wall at 26 cm, while the remainder expands to fill the inner region. This creates the non-uniform velocity profile shown.

Once the non-uniform jet discharging from the fan impinges upon the ground, the majority of the flow is transferred behind the fan resulting in the peak velocity measured at 270°, 10 cm above the ground (Figure 2-13.1). “Behind” the fan is defined as the side of the fan opposite to the inlet (Figure 2-6). Also, the velocities tend to be higher toward the 0° (left) side of the fan compared to the 180° (right) side of the fan. This indicates an asymmetrical distribution of the flow after it impinges, which is most likely due to two reasons: the shape of the fan outlet, and the non-uniform characteristic of the outlet velocity profile. The combination of these two factors could potentially cause a peak velocity at 270° and the flow to favor one direction over another. See Appendix A for further discussion.

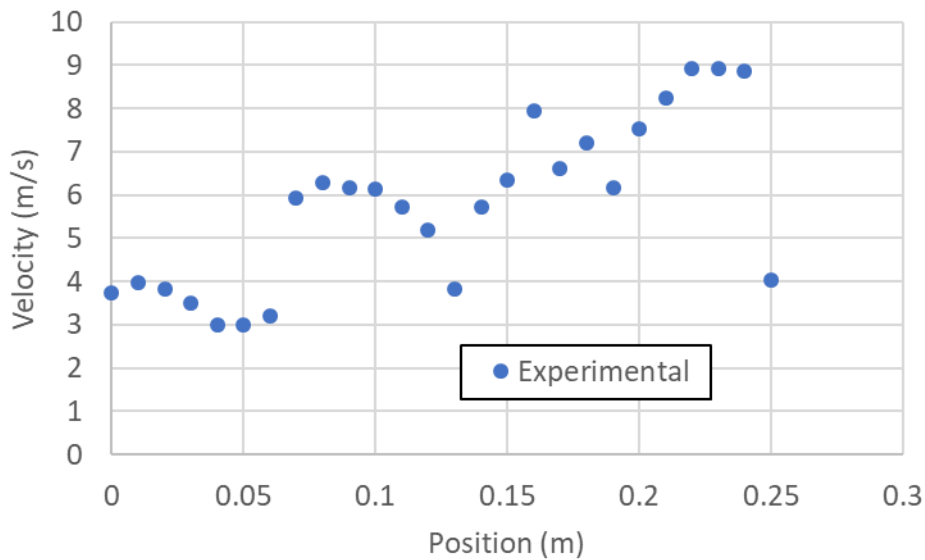


Figure 2-14: Velocity profile along centreline of exhaust for configuration 1, inverted vacuum fan

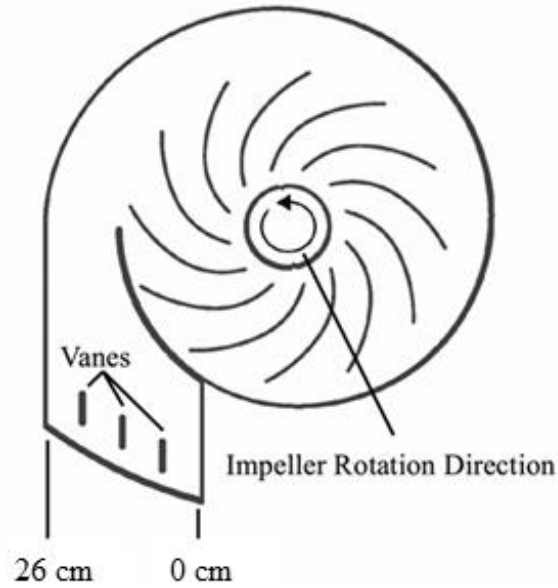


Figure 2-15: Interior view of vacuum fan

Figure 2-16 shows the velocity profile along the centreline of the 2D square diffuser's outlet. Measurements were taken at 1 cm intervals along the outlet centreline using the TSI 8455 digital Air Velocity Transducer. As with the profile of the vacuum fan, regions of reduced momentum in the diffuser profile are caused by the interior vanes. The peak velocity occurring between 43 cm and 53 cm is caused by the similar peak that occurred in the fan exhaust propagating through the diffuser. Comparing the diffuser outlet profile to the fan outlet profile, shows a reduction in the average exhaust jet velocity from 5.77 m/s to 3.33 m/s, or 42.3%.

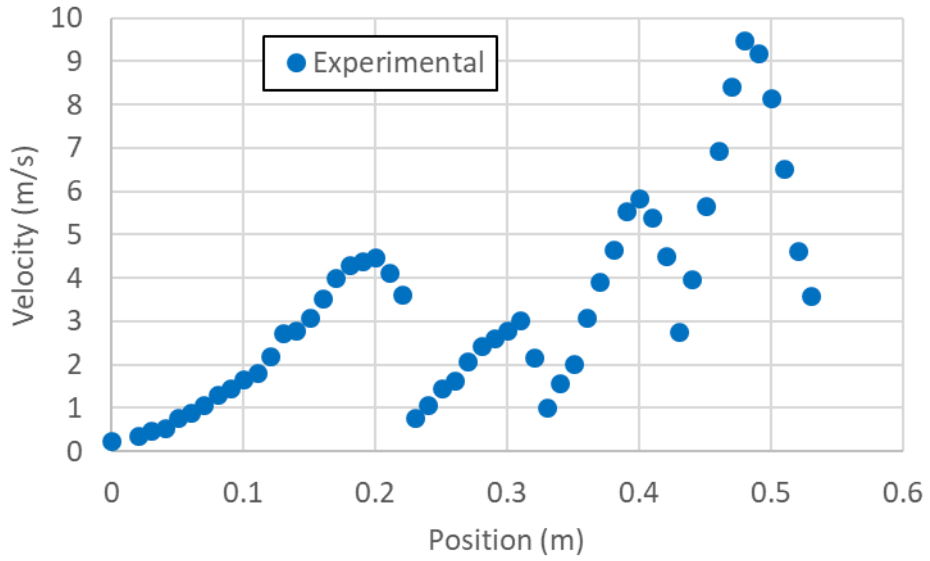


Figure 2-16: Plot of velocity profile along centreline for configuration 2, 2D square diffuser

Similar to the exhaust jet from the inverted fan, once the exhaust jet from the diffuser impinges onto the ground, it does not spread evenly (Figure 2-13). While no velocity higher than 0.32 m/s was recorded, a small peak does occur at 0° and 10 cm above the ground. This peak is a function of the diffuser geometry. The expanding side of the diffuser directs the exhaust to impinge upon the ground at a 30° angle from the vertical, towards the 0° (right) side of the fan as shown in Figure 2-17.

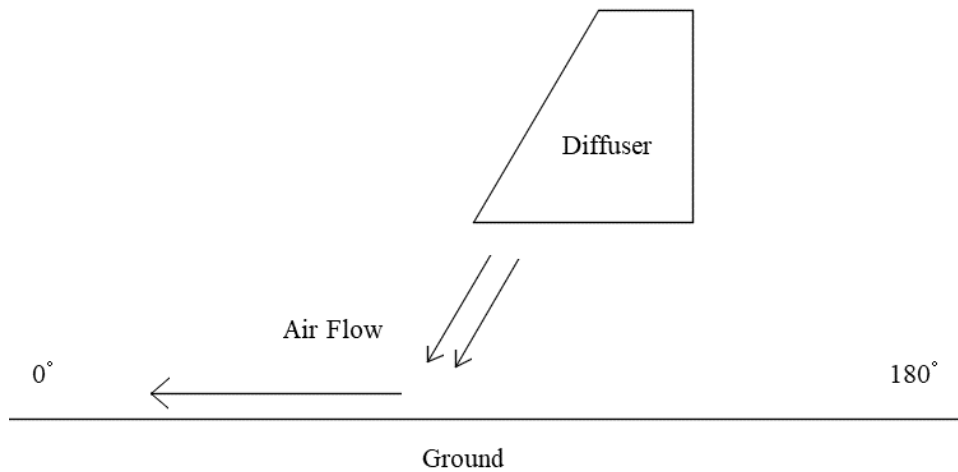


Figure 2-17: Schematic view of diffuser flow impingement

Figure 2-18.1 and 2-18.2 show the velocity profile along the centreline of each of the six outlets in the manifold diffuser, in addition to the velocity profile through the damper at the end of the diffuser. Measurements were taken at 1 cm intervals along each outlet centreline using the TSI 8455 digital Air Velocity Transducer. For each outlet plot, 0 cm is the edge of the outlet that is closest to the fan. For the damper, 0 cm is the edge closest to the ground. Table 2-4 provides a list of the flow rates through each of the outlets. While the intent of this diffuser was to have evenly distributed and balanced flow through each outlet, the velocity profiles and flow rates show this was not the case. In all six outlets, the profiles show that the majority of the air leaves the outlet through the last quarter of the opening. This is due to the momentum of the air flow carrying it past the openings, before reaching the far outlet wall and being directed downward.

It was later learned that a critical step to properly balance the air flow through each outlet was omitted. While the diffuser was designed such that the total pressure loss over the path to each outlet was equal, the magnitude of the pressure loss through each outlet was too small, i.e. the outlets were too large. For proper manifold performance, the highest loss along each flow path must occur through each outlet. Also, that loss should be at least an order of magnitude greater than the sum of the losses up to the outlet for the flow naturally balance.

Notwithstanding the failure of the manifold diffuser to provide equal flow at each outlet, the measurement of the velocity field around the manifold diffuser shows that this diffuser provides the most uniform air velocity distribution. All velocities measured around the diffuser were below 0.21 m/s, and no significant peaks occurred (Figure 2-13).

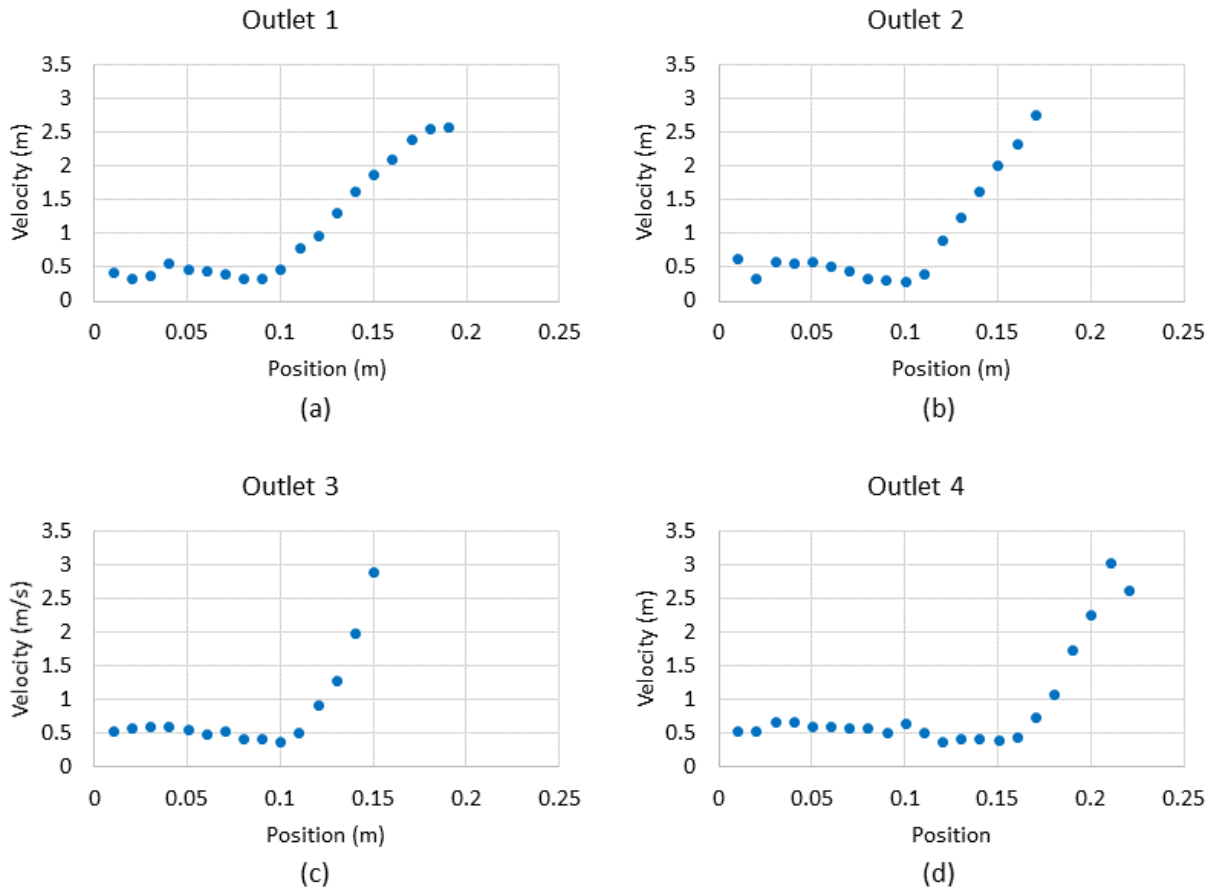


Figure 2-18.1: Plots of the velocity profile along the centreline of outlets one to four of the manifold diffuser

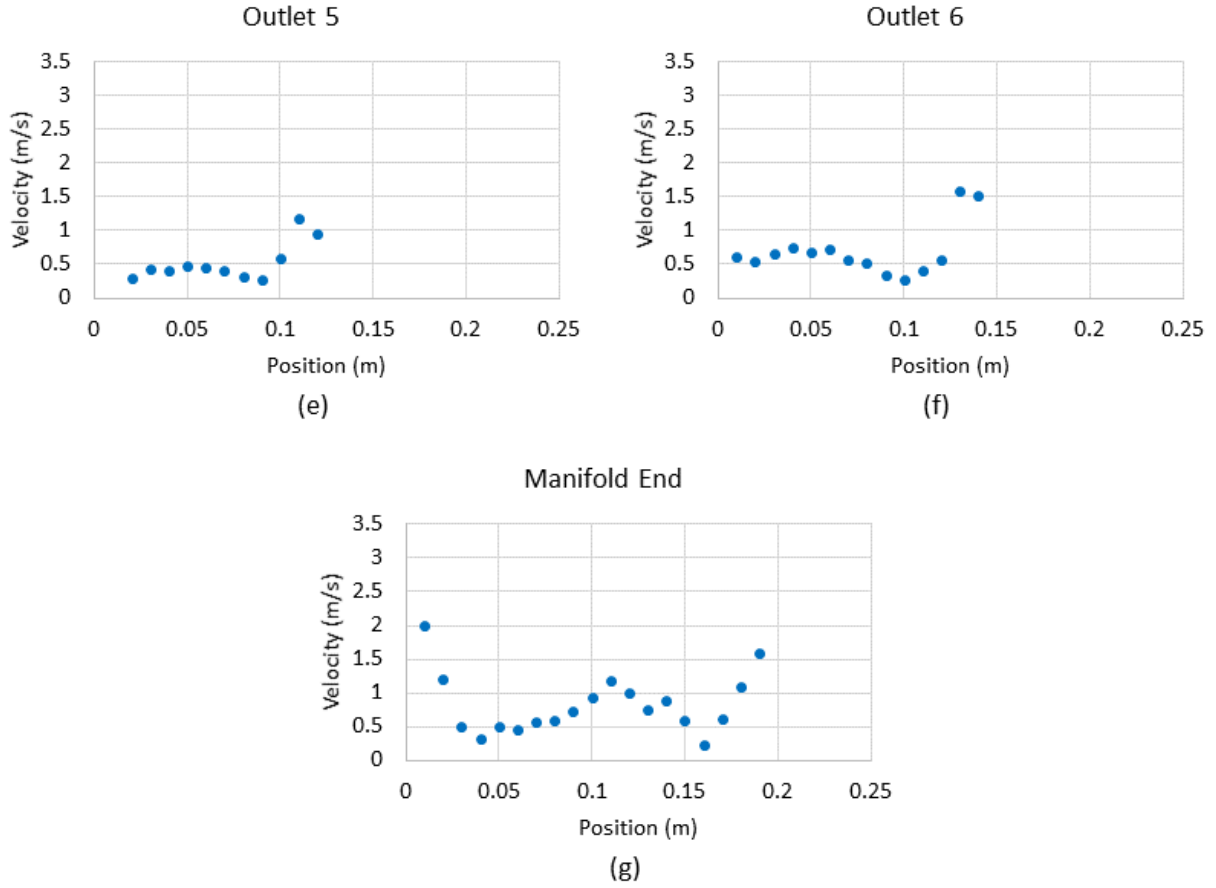


Figure 2-18.2: Plots of the velocity profile along the centreline of outlets five, six, and end of the manifold diffuser

Table 2-5: List of Manifold Diffuser Outlet Flow Rates

	Flow Rate [m ³ /s]
Outlet 1	0.022
Outlet 2	0.017
Outlet 3	0.014
Outlet 4	0.020
Outlet 5	0.007
Outlet 6	0.010
Manifold End	0.007

When comparing the performance of the three configurations against the ISO standard, configurations 1 and 2 are able to meet the velocity requirements of the standard at a 2.00 m radius around their exhausts. Configuration 3 is able to meet the intent of the standard, based on replacing the cylindrical domain with a stadium domain. Table 2-6 below summarises of the experimental velocities measured for each of the configurations.

Table 2-6: Summary of the Experimental Measured Velocities

Configuration	Inverted Fan	2D Square Diffuser	Manifold Diffuser
Max Velocity 0 – 0.25 m Range [m/s]	1.10 ±0.1	0.32 ±0.02	0.21 ±0.01
Max Velocity 0.25 –1.5 m Range [m/s]	0.24 ±0.01	0.15 ±0.01	0.16 ±0.01
Difference from Inverted Fan 0 – 0.25 m Range [%]	N/A	-70.9	-80.9
Difference from Inverted Fan 0.25 –1.5 m Range [%]	N/A	-37.5	-33.3
Average Exhaust Velocity [m/s]	5.77 ±0.4	3.33 ±0.2	0.86 ±0.1
Difference from Inverted Fan Average Velocity [%]	N/A	-42.3	-85.1

Comparing both the 2D square diffuser and the manifold diffuser to the inverted fan shows that a diffuser can significantly improve the performance of the fan against the ISO standard. Also with slower average jet velocities, any disturbance to the ground caused by the impinging jet should be minimized. The interaction between the ground and the exhaust jet is outside the scope of this research, and additional research would be required to confirm that the slower jet would reduce the disturbance on the ground. Comparing the two diffusers to each other, it can be seen that the extra outlets on the manifold diffuser, with their current performance, provide marginal benefit over the single outlet of the 2D square diffuser, with the manifold diffuser only providing a reduction of 0.11 ±0.02 m/s in the recorded peak velocity. Without further refinement, the extra work it would take to produce and mount the manifold diffuser to the planter would not be worth the minimal improvement in performance relative to the ISO standard. Furthermore, before it could be considered as a viable alternative, a properly designed manifold diffuser must be built and validated.

2.5 Chapter Summary

This chapter presented the methodology and results of the experimental component of this thesis. Three different fan configurations, i.e. the inverted vacuum fan, the 2D square diffuser, and the manifold diffuser were measured against the ISO 17962 Standard. The inverted fan and 2D square diffuser easily meet the standard. The manifold diffuser did not perform as intended, i.e. it did not exhaust equal flowrates through all of the outlets: therefore, this concept was not considered for CFD simulation. Overall, the experimental study showed that by properly directing the fan exhaust towards the ground, the CNH Industrial vacuum fan can meet the ISO standard.

CHAPTER 3 COMPUTATIONAL FLUID DYNAMICS MODELS

3.1 Introduction

The following chapter will document CFD simulations of the experimental configurations explored in Chapter 2. While three configurations were tested against the ISO standard, only two of the three configurations were simulated using CFD. The manifold diffuser (Configuration 3) was not modelled for two reasons. First, for the diffuser to operate as intended, further refinement of the design was necessary. Second, due to the multiple outlets and different domain, i.e. a stadium versus a circle, a direct comparison to the other configurations becomes problematic, as shown in Chapter 2. For each configuration that was modelled, the geometry, mesh, solution method, and results will be discussed in detail. ANSYS Fluent 15.0™ was used to run all the CFD models for this research project.

3.2 CFD Theory

The following section presents some general theory related to CFD. Since the model of the centrifugal vacuum fan was the most complex of the models created, examples specific to this model will be highlighted in this section.

The CFD package ANSYS Fluent 15.0™ was chosen to model the flow inside and around the vacuum fan. The Fluent CFD solver is based on the finite volume method, which solves the flow by discretizing the domain into a finite number of control volumes or cells. Flow variables are defined at the centroids of each cell. Then continuity and Navier-Stokes equations are discretized and solved iteratively for each cell by discretely integrating the surface and volume integrals. The effect of turbulence is included by solving the Reynolds Averaged Navier-Stokes (RANS) equations for the mean flow field. The RANS equations include the effect of the Reynolds stresses (MacCormack, 2014; ANSYS™ Inc., 2013b). The continuity and RANS equations are discretized by integrating the transport equations over each cell. The resultant set of coupled linear algebraic equations is solved iteratively.

The first step in solving a CFD model, independent of the software chosen, is to identify the solution domain. Once the domain is identified, it can then be discretized into a mesh of cells. For this study, the domains were created from CAD (computer assisted design) drawings. To reduce the complexity of the domains and minimize the number of cells needed, unnecessary features were removed. Examples of such features are bolts, holes, fillets, or any other features that are too small to affect the overall flow.

In Fluent, skewness and orthogonal quality are used to measure the quality of a mesh. Skewness is defined on a scale of zero to one and is a measure of how close each cell is to its ideal shape. A skewness value of zero (0) denotes a cell that is perfect, not skewed in any direction. A value of one (1) denotes a cell that is skewed in one or more directions in such a way to render the three-dimensional volume into a two-dimensional shape or a two-dimensional shape into a line or thin sliver. Figure 3-1 shows an example of skewness for two-dimensional triangle and quadrilateral shapes, as the skewness increases the shapes change from fully two-dimensional forms to linear elements. The quality of a mesh deteriorates as skewness increases. A mesh with an average skewness value between 0.0 and 0.94 is considered to be of acceptable quality, while a value greater than 0.98 is considered unacceptable for most applications (ANSYS™ Inc., 2013a). Skewness in a mesh can be reduced by decreasing cell size near complex geometrical boundaries, as larger cells tend to be more skewed in these locations.

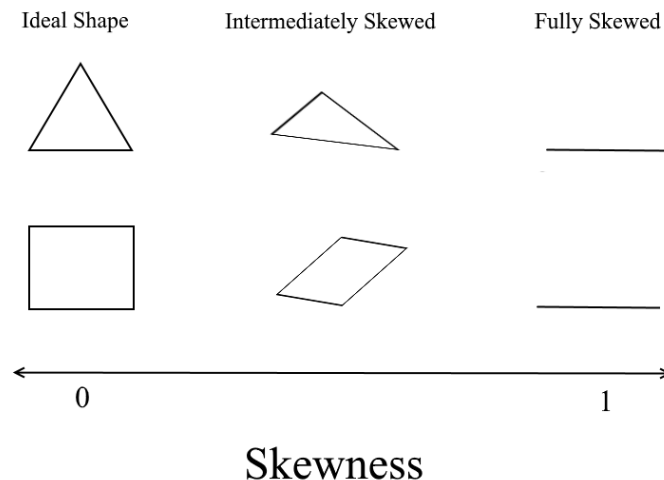


Figure 3-1: Examples of skewness ranging from not skewed to fully skewed

Orthogonal quality is a measure of how well each cell is aligned with its neighbouring cells. It is calculated by comparing the vectors normal to each cell face to a vector drawn between the centroids of each adjacent cell, and to a vector drawn between the centroid of each cell to each cell face. Figure 3-2 gives examples of good and poor orthogonal quality, along with the vectors used to calculate orthogonal quality. The red arrow is the vector from the centroid of the cell to the cell face, the blue arrow is the vector normal to the cell face, and the green arrow is the vector between the centroid of the two cells. For good orthogonal quality all three vectors are aligned, while for poor quality one or more of the vectors are not aligned. Quantitatively, an orthogonal quality value of one (1) is defined as being perfectly aligned and a value of zero (0) as being completely unaligned. A mesh with an average value of 1.0 to 0.15 is considered to be of acceptable quality, with any lower values unacceptable for most applications (ANSYS™ Inc., 2013a). As cells become more skewed, the orthogonal quality deteriorates and can be improved by using smaller cell sizes near complex geometry.

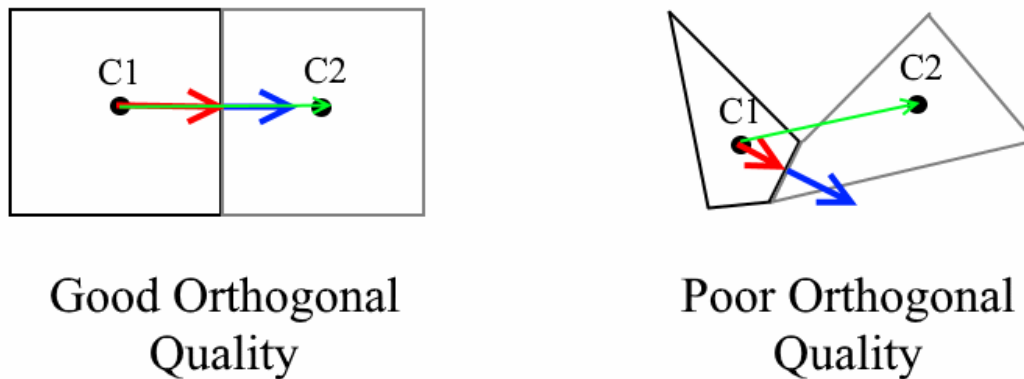


Figure 3-2: Examples of orthogonal quality

By minimizing skewness and maximizing orthogonal quality, higher quality meshes are produced. Meshes with high skewness and poor orthogonal quality can produce erroneous results, such as predicting unrealistically high velocities due to poor communication of data between cells. Both metrics apply to unstructured and structured meshes. Figure 3-3 presents a comparison of unstructured and structured meshes. An unstructured mesh is comprised of tetrahedral shaped elements that vary in size and shape and each element has no specific orientation. A structured mesh is comprised of hexahedral cubes that align with each other.

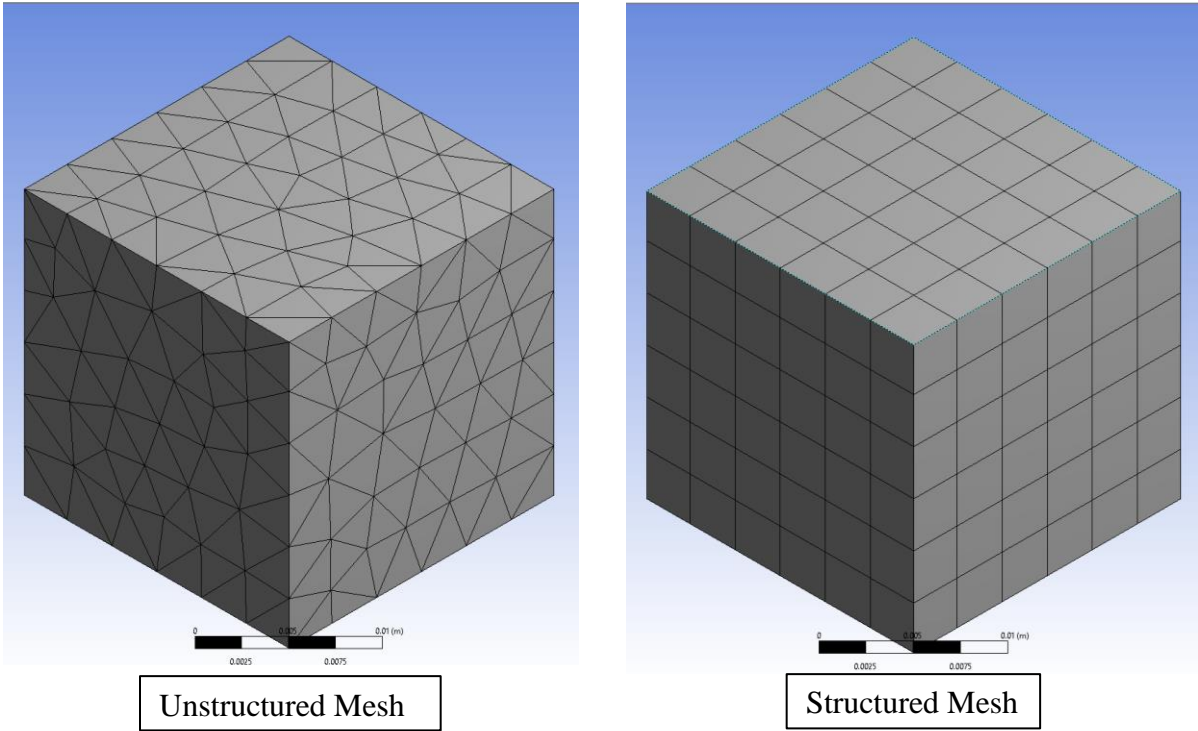


Figure 3-3: Examples of unstructured and structured meshes

In meshes with complex geometry, an unstructured mesh will usually produce cells with a lower skewness for a given cell size. A structured mesh typically requires smaller cell sizes to capture finer geometry details.

For CFD models of centrifugal fans, as with most other CFD models, the number and size of cells play a large role in determining the accuracy of the model. Coarse meshes or meshes with skewed cells can lead to less realistic results. As a rule of thumb, at a minimum 70,000 to 100,000 cells are required to achieve minimum acceptable results (Gülich, 2010). Also, the literature review showed that meshes with greater than 500,000 cells were able to produce model results comparable to experimental measurements. Note that by discretizing the domain into a mesh, discretization error is introduced into the solution. This error cannot be completely eliminated but it can be minimized to the point where the discretization error is much smaller than other sources of error, by conducting a mesh refinement study. As the number of cells in the mesh increases the average cell size decreases. Once the cell size decreases below a certain threshold, the effect of further decreasing the cell size diminishes to the point where the solution becomes no longer dependent on the mesh size, i.e. the numerical error from the discretization

becomes sufficiently small and no longer appreciably influence the results of the simulation (Versteeg &, Malalasekera, 2007). A mesh independent solution can be found by identifying some characteristic variables in the problem, such as flow rate and pressure for a fan, and measuring the change in those variable for increasingly refined meshes (Gülich , 2010). As the mesh is further refined the change in the variables from one refinement to another should decrease. Once the change has decreased to an acceptable level, depending on the level of uncertainty in the rest of the model, the mesh can be deemed as no longer being a significant source of error (Versteeg &, Malalasekera, 2007). However, increasing the number of cells increases the amount of time required for a simulation. Therefore, with limited computational resources, a balance must be found between the computational size of the mesh and ensuring that the cells are small enough to not overly influence the model solution. According to the literature review, in the case of modelling a centrifugal fan, using an unstructured mesh made up of tetrahedral shaped cells will aid in achieving this balance.

In running a fan simulation, it must be decided if a steady state or transient (time dependant) method will be used to solve the flow. In the case of a centrifugal fan, one of the most common steady state methods is the frozen rotor method. This method approximates the flow through the fan by using two reference frames, one rotating and one stationary. The rotating reference frame is defined around the impeller. During the computation this reference frame mathematically imposes an angular velocity component upon the flow throw the impeller to model the impeller's rotation while the impeller remains fixed or frozen. The stationary reference frame is defined as the remainder of the fluid domain. This method is much less computationally intensive compared to a transient solution, and has been used with success in modelling centrifugal fans (Son, Kim, & Ahn, 2011). However, it does have one major weakness: The frozen rotor method solely solves the flow with the two reference frames at a set relative orientation, which means that the impeller blades are set at a single position relative to the casing and volute. This introduces inaccuracies to the solution as it ignores the inherent unsteadiness inside the fan, and cannot correctly predict how the flow leaves the impeller blades (Dick, et. al., 2001). To solve the flow in a transient manner the sliding mesh method can be used. In this method, the mesh making up the impeller is rotated incrementally at each time step, modelling the movement of the fan impeller. In other words, the geometry of the mesh changes with each time step. This allows the flow inside the fan to develop as it would in reality, changing with the rotation of the impeller,

and recreating the unsteadiness of the flow in the fan. It is for these reasons that the sliding mesh method is widely considered to be superior for simulation of centrifugal fans (Corsini, Delibra, & Sheard, 2013).

To have a transient simulation produce accurate results and achieve solution convergence, the proper time step size must be selected. This is accomplished through the use of the Courant Friedrichs Lewy (CFL) number; also known as the Courant number. The CFL/Courant number is defined as follows:

$$\text{CFL} = \frac{u\Delta t}{\Delta x} \quad (3-1)$$

where u is velocity (m/s), Δt is the time step (sec), and Δx is the length interval (m). For a transient fan simulation, u is taken to be the rotational velocity of the impeller, and Δx is the size of the smallest cell in the impeller mesh. Usually, the time step, Δt , is taken so that $\text{CFL} < 1$, however Courant numbers greater than one have been shown to still produce accurate results (Petit & Nilsson, 2013). A sufficiently small time step, will usually mean that the solution from one time step to the next does not change significantly. This leads to a well behaved, non-diverging, simulation that can be solved with fewer iterations per time step (Gjernes, 2014). The length of time that is required to be simulated for the flow through a fan depends on the goal of the model. For example, if the goal is to study the flow patterns inside a fan during start-up, only a few rotations, one to four, are required to be simulated. However, if the goal is to study the flow during regular operation of the fan, as is being done in this work, then the model must run until the flow develops past the initial start-up stages and enters a pseudo-steady state or fully developed stage. The operational stage is referred to as pseudo-steady state because the flow inside the fan is in reality unsteady, but the flowrate and pressure that the fan produces is constant. To fully develop the flow within the fan it may take five to eight rotations of the impeller, possibly more if the flow is extremely unsteady (Gülich, 2010).

Properly modelling the turbulence is also important. ANSYS Fluent™ offers a number of turbulence models. Of the available turbulence models, the standard $k-\varepsilon$ model, the renormalization-group (RNG) $k-\varepsilon$ model, the realizable $k-\varepsilon$ model, and the shear-stress transport (SST) $k-\omega$ model have been used to successfully model turbulence in a centrifugal fan. A brief description of each of these models is as follows:

Standard k - ε : This is the simplest of the turbulence models presented. It uses two equations to model the turbulence kinetic energy, k , and its dissipation rate, ε . It provides reasonable accuracy for a wide variety of flows. However, typically it is only used for modelling simpler shear flows, as it cannot accurately model boundary layer separation, rotating flows, and decelerating flows (Fluent Inc., 2001).

RNG k - ε : This turbulence model is an improvement over the standard k - ε model. It uses the standard equation for k and adds an additional strain term to the ε equation. While this allows for better accuracy when modelling swirling flows, this model still has many of the same limitations as the standard k - ε model (Fluent Inc., 2001).

Realizable k - ε : This model was proposed as an improved version of the standard k - ε model; it is better suited to solving flows with jets, rotation, boundary layer separation, and boundary layer recirculation. The model is called realizable because it ensures some aspects of the turbulence are physically realistic. For example, it ensures that the k - ε equations use a positive normal Reynolds Stress. The standard k - ε model, when it encounters a large strain, can predict a negative normal stress, which is not realistic. Using the realizable k - ε model ensures that the normal stress stays positive throughout the solution (Shih, Liou, Shabbir, Yang, & Zhu, 1994).

SST k - ω : This model attempts to improve the standard k - ε model by blending it with the k - ω model, where dissipation rate, ε , is replaced with the specific dissipation, ω . It specializes in modelling flows with high pressure gradients and flow separation. It can, however, introduce unnaturally high turbulence levels when encountering flows with large accelerations or stagnant regions (Gjernes, 2014). The main advantage with this model is that it better models flow near a wall, where a k - ε model may suppress boundary layer separation, the k - ω model will not. Also since the SST k - ω model is a blend of the k - ε model with the k - ω model, it has the performance of the k - ε model in the far field, where the k - ε model has an advantage in accuracy over the standard k - ω model (Versteeg & Malalasekera, 2007).

The main difference in the above models is how the dissipation of the turbulence is calculated. However, all four of these turbulence models have a common weakness: their use of an eddy

viscosity relation to calculate the Reynolds stress, which is best used for simple shear flows. These models all assume an isotropic turbulent viscosity, i.e. that it is the same in all directions. By assuming an isotropic turbulent viscosity, each of the models can produce erroneous results in complex flows. Since the Reynolds stress is being modeled rather than directly calculated, the accuracy of the solution is limited. The advantage in using an eddy viscosity relation, is that it is easy to have converge, and is not resource intensive to calculate (Versteeg &, Malalasekera, 2007). Of the four turbulence models presented for modelling centrifugal pumps and fans, the realizable $k-\varepsilon$ model has been shown to resolve the flow features most accurately, when measured against experimental results (Petit & Nilsson, 2013). Hence, it was chosen for this research project.

With greater time and/or more computational resource, the use of a Reynolds stress model (RSM) could have been explored. The RSM model, also called a second-moment closure model, is described in six partial differential equations (PDE), instead of the two PDEs of the previously mentioned models, each to calculate the transport of Reynolds stresses. This removed the need for the eddy viscosity model and its inherent flaws. However, the disadvantage of using an RSM is that it is computationally intensive and as such hasn't been as extensively validated as the two equation models (Versteeg &, Malalasekera, 2007).

In Fluent, when specifying the turbulence model, a wall treatment model is also specified that will handle the reduction of turbulence near the wall. As the distance from the wall increases beyond the viscous sublayer, the velocity increases in a non-linear manner. Resolving this region can be costly in terms of computational power and often it is more efficient to model the near-wall region rather than attempting to calculate and fully resolve it close to the wall. For example, a wall function will locate the first node in the fully turbulent region away from the wall, and bridge the flow to the wall using some universal relations. From the literature review, the standard log-law wall model was shown to provide adequate results and will be employed for this study. The standard log-law is defined as follows:

$$\frac{u_p}{u_\tau} = \frac{1}{\kappa} \ln \left(\frac{y_w u_\tau}{\nu} \right) + C^+ \quad \text{where } u_\tau = \sqrt{\frac{\tau_w}{\rho}} \quad (3-2)$$

where u_p is the fluid velocity parallel to the wall [m/s], u_τ is the friction or shear velocity [m/s], κ is the Von Karman constant (typically 0.41), y_w is the distance from the wall (m), ν is the kinematic viscosity of the fluid [m²/s], C^+ is a constant (~ 5.0 for a smooth wall), τ_w is the wall shear stress [Pa], and ρ is the density of the fluid [kg/m³] (White, 2011). All walls, including the ground, were considered smooth with respect to the log-law in this thesis.

The final aspect of a CFD model that will be discussed in this section is the boundary conditions. The boundaries for a centrifugal fan model consist of the solid walls of the casing, volute, and impeller; the inlet, located above the eye of the impeller; and the outlet of the fan. Specifying the boundary conditions at the walls is handled automatically by the CFD software. It employs a no-slip condition at the wall for the velocity component parallel to the wall, while the velocity component normal to the wall is set to zero (Gülich, 2010). To define the inlet, three parameters are given: the average inflow velocity, a turbulence level, and a turbulence length scale. The average inflow velocity sets the desired flow rate through the fan. For the turbulence level, a value of 5% of the inflow velocity squared has been found to produce reasonable results, as has a length scale equal to the impeller inlet diameter. Note, the interior of the fan is a region of high turbulence and sensitivity studies have shown that model results are not sensitive to inlet turbulence parameters, as the impeller introduces much higher turbulence levels (Gülich, 2010). The outlet of the fan model is defined using the average static pressure seen at the outlet (Gülich, 2010). Note, according to standardised fan testing procedures, in the case of a fan discharging to atmosphere, the pressure seen at the outlet can be considered to be equal to atmospheric pressure (AMCA and ASHRAE, 1985).

3.3 The Inverted Vacuum Fan Model

The simulation of the production fan was divided into two parts. The first was a transient simulation of the isolated fan, drawing in air through the inlet and discharging it through the exhaust. The second simulation was a steady state model that used the results from the first simulation as an input parameter. It used the exhaust velocity profile from the final time step of the transient simulation to simulate the exhaust of the exhaust jet impinging on the ground. The simulation was broken into two parts to reduce the computational complexity in two ways. First, it allowed for the fan simulation to use a transient solution and the simulation of the surrounding

air to use a steady state solution. Second, it reduced the total cell count of the exhaust jet simulation to a more manageable level, which would reduce overall computation time. By basing the steady state model on the results from the transient, the steady state model is essentially a “snap shot” in time, showing the overall flow field based on a single time step. Since the flow rate through the fan is constant, this is assumed to be representative of the flow field in the air surrounding the fan.

3.3.1 Inverted Vacuum Fan Geometry

The inverted vacuum fan geometry was based on a CAD model provided by CNH Industrial Planter Engineering department and the Soil & Crop Modeling Team. The fluid domain of the interior of the fan was required to model the flow through the fan. The definition of this domain began with simplifying the fan CAD model. The original CAD model is shown in Figure 3-4. The simplification consisted of removing unnecessary features such as bolt holes, chamfers, and individual bolts. This simplified model was then “filled” with fluid, and the original CAD model removed. This process resulted in a domain that consists solely of a fluid body that represents the interior of the fan. Figure 3-5 shows the fluid domain of the fan. This domain was cut into three volumes, or sub-domains, to allow for the sliding mesh method to be used to model the rotation of the impeller. Volume A is the stationary fan case and volute, volume B is the stationary inlet region, and volume C will contain the rotating impeller mesh.

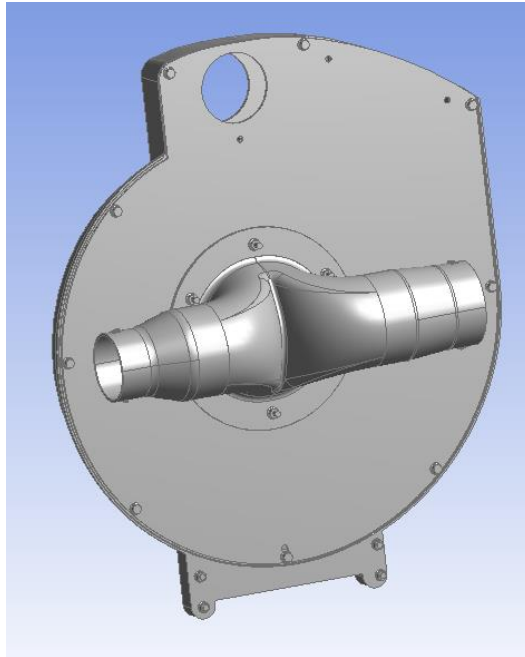


Figure 3-4: Production vacuum fan CAD model

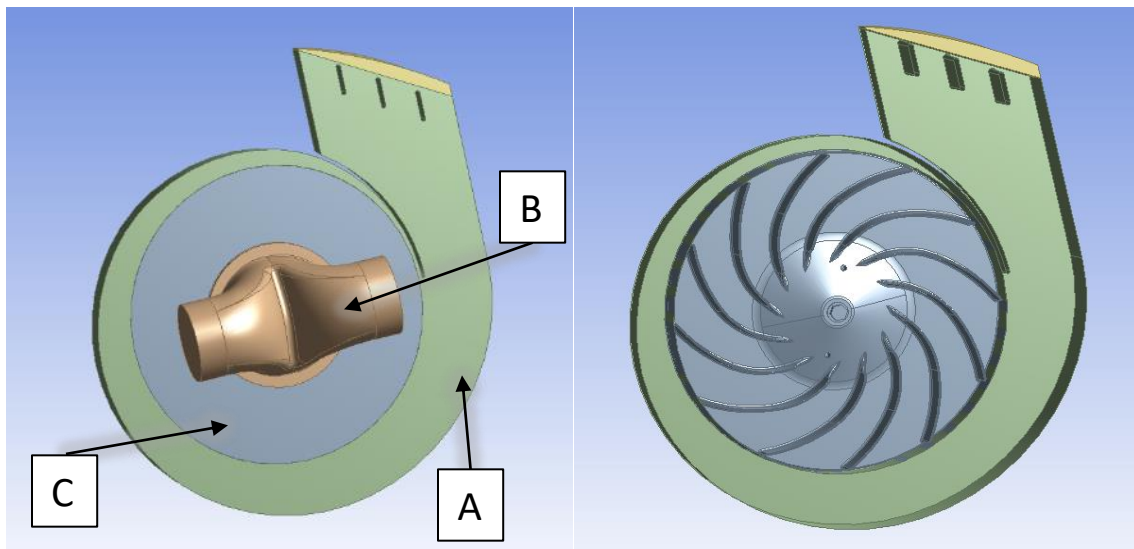


Figure 3-5: Exterior and interior of the fan fluid domain

The second fluid region that was modelled for this configuration was the discharge domain surrounding the inverted fan. Figure 3-6 shows the geometry of this domain, which was divided into three volumes. Volume A contains a void to represent the casing of the fan, and contains the

fan exhaust. Volume B allows for refinement of the mesh that would contain the area where the jet from the fan's exhaust impinges on the ground. Volume C surrounds the other two regions and extends outward to a 2-m radius from the fan. The edge of volume C corresponds to the locations measured in the experimental part of this work. The height of the discharge domain was limited to 1.0 m for the CFD model, rather than the full 1.5 m height of the experimental domain. This was done for two reasons: decreasing the height decreases the volume of the domain by 33%, reducing the number of cells, and the experimental section results indicate that above 1 m in elevation the fan exhaust had negligible effect on the surrounding domain.

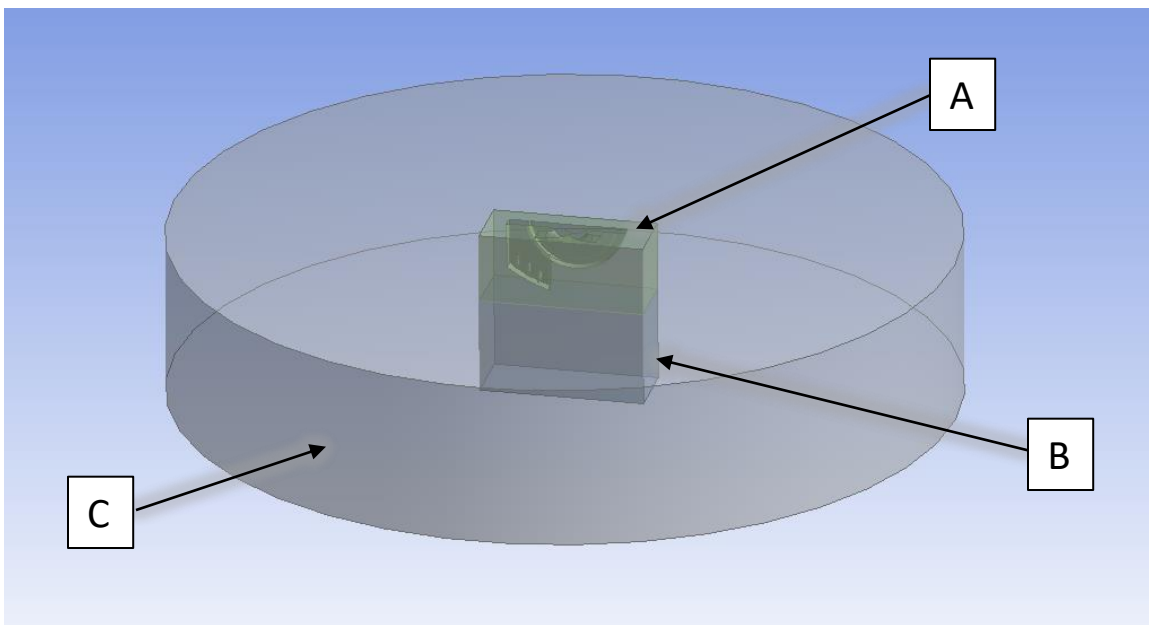


Figure 3-6: Three-dimensional isometric view of the fluid domain surrounding the inverted vacuum fan

3.3.2 Mesh

ANSYS Meshing™ was used to create the meshes for the models of the fan and the surrounding discharge domain. The fan mesh was unstructured and consisted of tetrahedral cells ranging in size from 1×10^{-3} m to 1×10^{-2} m (1 mm to 10 mm). At the outlet of the fan the maximum element size was set to 5×10^{-3} m (5 mm). To be able to resolve the boundary layer inside the fan, an inflation layer was used along the sidewalls of the fan. This resulted in a mesh that consisted of 1,876,658 elements and had an average orthogonal quality of 0.8059, and an average

skewness of 0.3458. The mesh contains a similar number of elements to the meshes cited in the literature review, and the skewness and orthogonal quality were in an acceptable range. Figure 3-7 shows a close-up of the mesh and inflation layer. Also shown is the interface between the mesh of the rotating impeller (green) and the stationary casing (yellow). The average size of the elements along this interface was approximately 1×10^{-2} m (10 mm) on average.

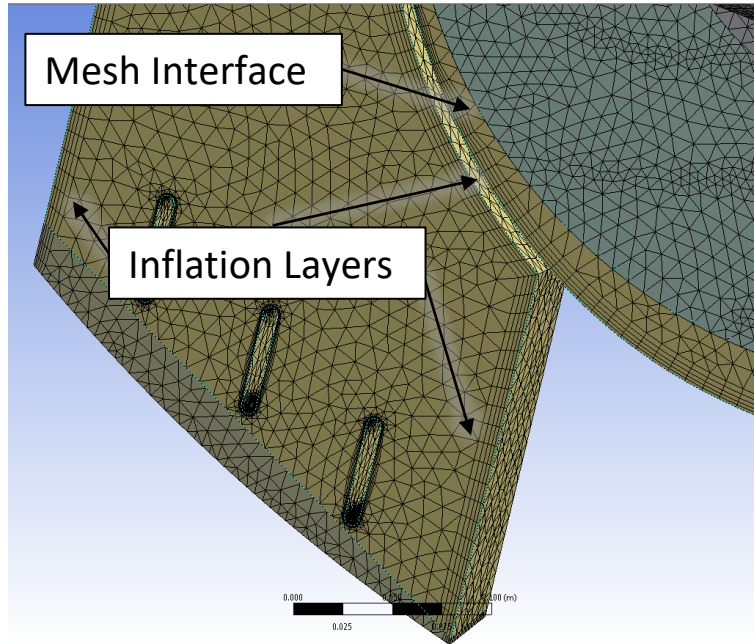


Figure 3-7: Close-up view of the inflation layers in the fan's volute and outlet and the interface between the rotating and stationary meshes

For the above mesh and all meshes following, a grid independence study was not completed. Rather, using advice and rules gleaned from the literature review and consultation with ANSYS™ support, a single high cell count mesh was created for each model. This was justified in three ways: by ensuring the mesh was of high quality, i.e. low skewness with high orthogonal quality, by utilizing inflation at the no-slip boundaries to properly resolve the boundary layers, and by employing meshes with high cells counts, similar in number to the meshes in the literature that were found to be grid independent. The literature review, in Section 1.3.2, found models of fans with cell counts ranging from 500,000 to 5,800,000 to be grid independent. The mesh for the above model, with 1,800,000 cells, falls within that range.

Figure 3-8 shows the interior of the mesh of the discharge domain surrounding the fan. It illustrates the three mesh regions that comprise the domain. Volume A is a void to represent the case of the fan, volume B is a region that was refined to capture the fan exhaust jet, and volume C is the air surrounding the fan. The inlet to model is located at the fan exhaust in volume A, and the model outlet located along the periphery of volume C. This mesh consisted of unstructured tetrahedral elements with cells ranging in size from 5×10^{-3} m to 3×10^{-2} m (5 mm to 30 mm). The elements in the jet region were refined to a size of 2×10^{-2} m (20 mm). To resolve the boundary layer created by the impinging jet an inflation layer was used along the ground plane. The resulting mesh was made up of 6,408,719 elements, had an average orthogonal quality of 0.8714, and an average skewness of 0.2118.

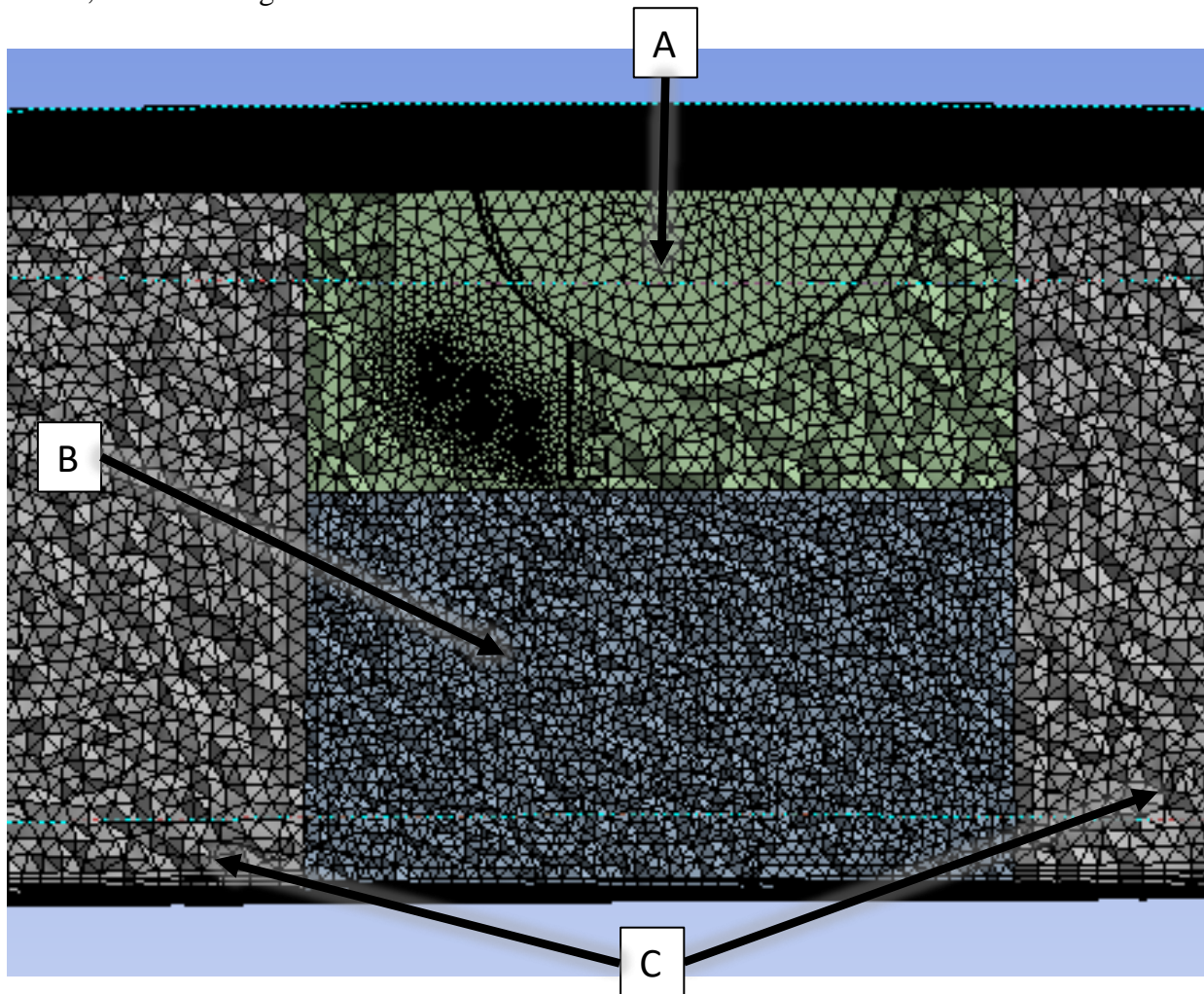


Figure 3-8: Three-dimensional view of the interior mesh of the fluid domain surrounding the inverted vacuum fan

3.3.3 Solution Set-up

This section presents the parameters used to model the flow through the vacuum fan, and to model the jet from the fan exhaust and its effect on the surrounding domain.

The turbulence model used for the transient vacuum fan simulation was the realizable k- ϵ model in conjunction with a standard log-law wall treatment. This model was selected based on a review of the literature and a recommendation from ANSYS™ technical support. The boundary conditions of the fan simulation were as follows: the inlet was given a uniform velocity of 3.35 m/s, the outlet was set as atmospheric pressure, 95 kPa, and the walls of the impeller and the case were set as a no-slip boundary. Both inlet and outlet conditions are based upon the experiment. For this model and every subsequent model, a second order upwind differencing scheme was used to calculate fluxes through the mesh faces.

The time step of the simulation was set to be 4.76×10^{-5} s, and the impeller was set to rotate at 3500 RPM. This resulted in 360-time steps per revolution or 1° per time step. This gave the simulation a run-time of approximately 24 hours for one revolution of the impeller, using an Intel® Xeon® Processor E3-1270 running at 3.50 GHz with 32 GB of RAM. The time step was calculated using the CFL number, which was set to one (1); the length scale was set to the length of the cells making up the tips of the impeller blades (0.05 m), and the velocity was the impeller blade tip speed, i.e. 97.7 m/s (base on a rotational speed of 3500 RPM and an impeller diameter of 533 mm).

The turbulence model used for the steady state simulation of the discharge domain surrounding the fan was also the realizable k- ϵ model with a standard log-law wall treatment. This model was selected for its ability to accurately model turbulence in a jet flow. There were three boundary conditions in this model: a no-slip boundary at the ground plane and on the exterior of the fan; the inlet, which used the outlet velocity profile from the final time step for the fan model; and the boundary above the fan and along the 2.0 m radius around the fan, which was set as an outlet under atmospheric pressure, 95 kPa.

3.3.4 Results

The fan simulation was run until a fully developed flow was present at the exhaust, which required 6660-time steps or 18.5 revolutions, and was equivalent to the fan running for 0.317 s. The flow was said to be fully developed when the shape of the velocity profile at the outlet of the fan did not change for a full rotation of the impeller.

Figure 3-9 presents the velocity contours and direction vectors of the flow in the fan on the mid-plane of the fan. The direction vectors are not scaled with the velocity of the flow and are mainly intended to indicate local flow direction. Also, they have been evenly distributed through the domain and are not representative of the grid size, which is true for all figures with direction vectors. The figure shows that as the impeller rotates in a counter clockwise direction, air is drawn into the impeller and accelerated tangentially through the blades toward the casing. After the flow leaves the impeller it begins to decelerate and is directed to the volute by the casing. The flow continues decelerating as it passes through the volute and exits the fan through the exhaust.

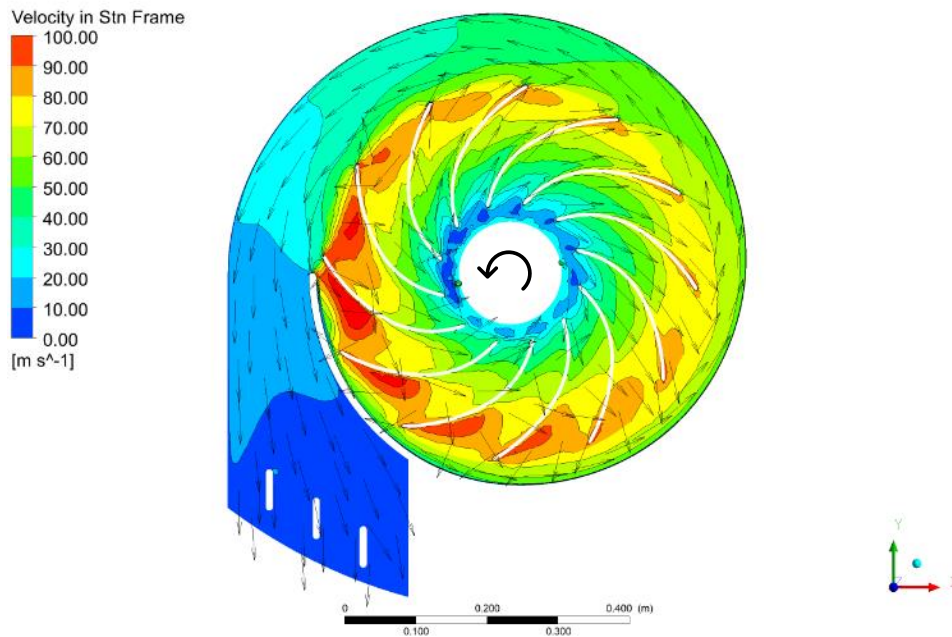


Figure 3-9: Velocity contours and vectors inside of fan, 0 m/s – 100 m/s

Figure 3-10 shows a close-up view of the velocity contours and direction vectors in the exhaust section of the fan, with a velocity scale appropriate to the region of interest. Again, the vectors

are not scaled with flow velocity. This image illustrates how the highest exhaust velocity occurs towards the exterior edge of the fan outlet, in region A along the outer wall. As the flow enters the expanding section of the outlet, the high velocity air follows the wall at A until the flow exits the fan. Downstream of each vane a wake forms, producing three regions of low velocity.

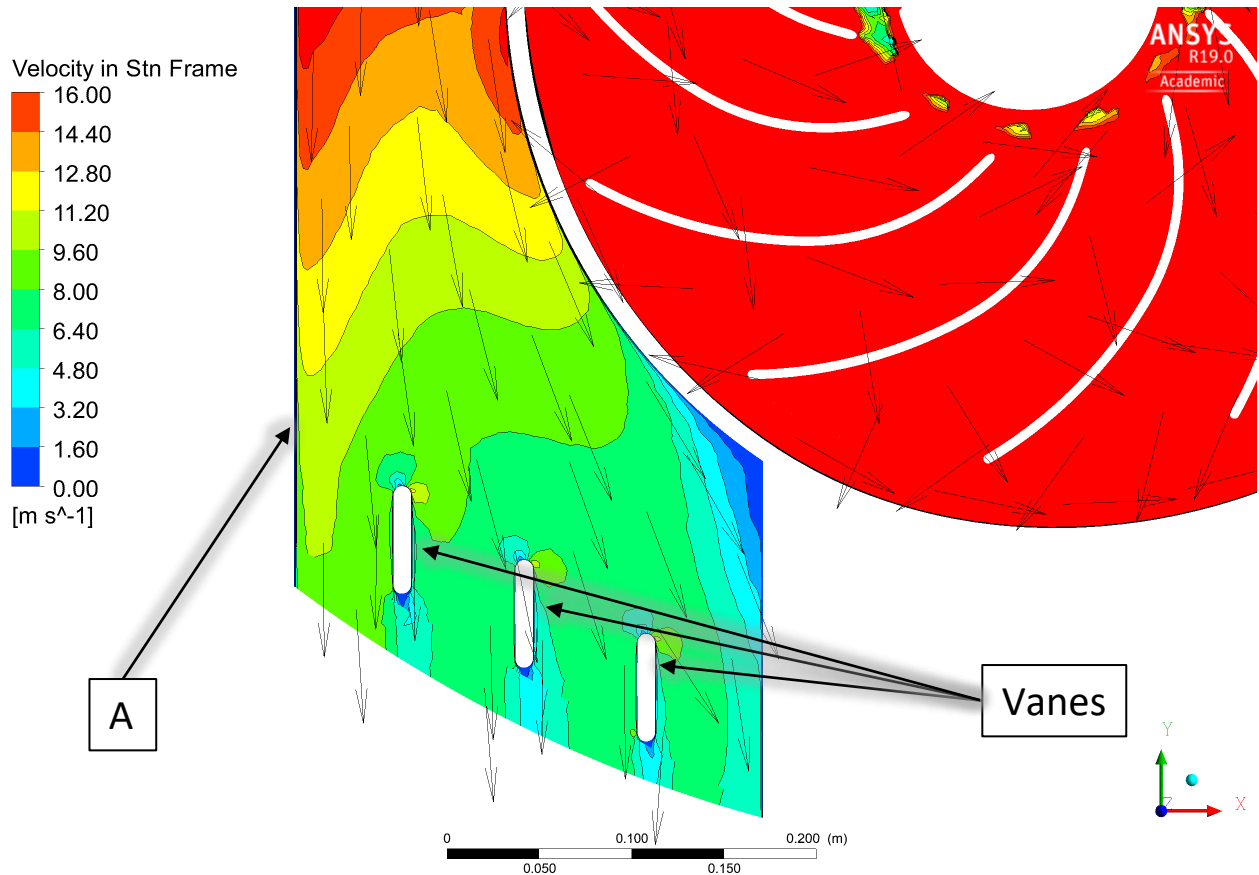


Figure 3-10: Close-up view of velocity contours in the fan volute and outlet, 0 m/s – 16 m/s

Figure 3-11 presents contours of gauge pressure in the exhaust section of the fan. It shows that as the cross-sectional area in the exhaust section expands, the static pressure steadily increases until it reaches atmospheric value at the outlet.

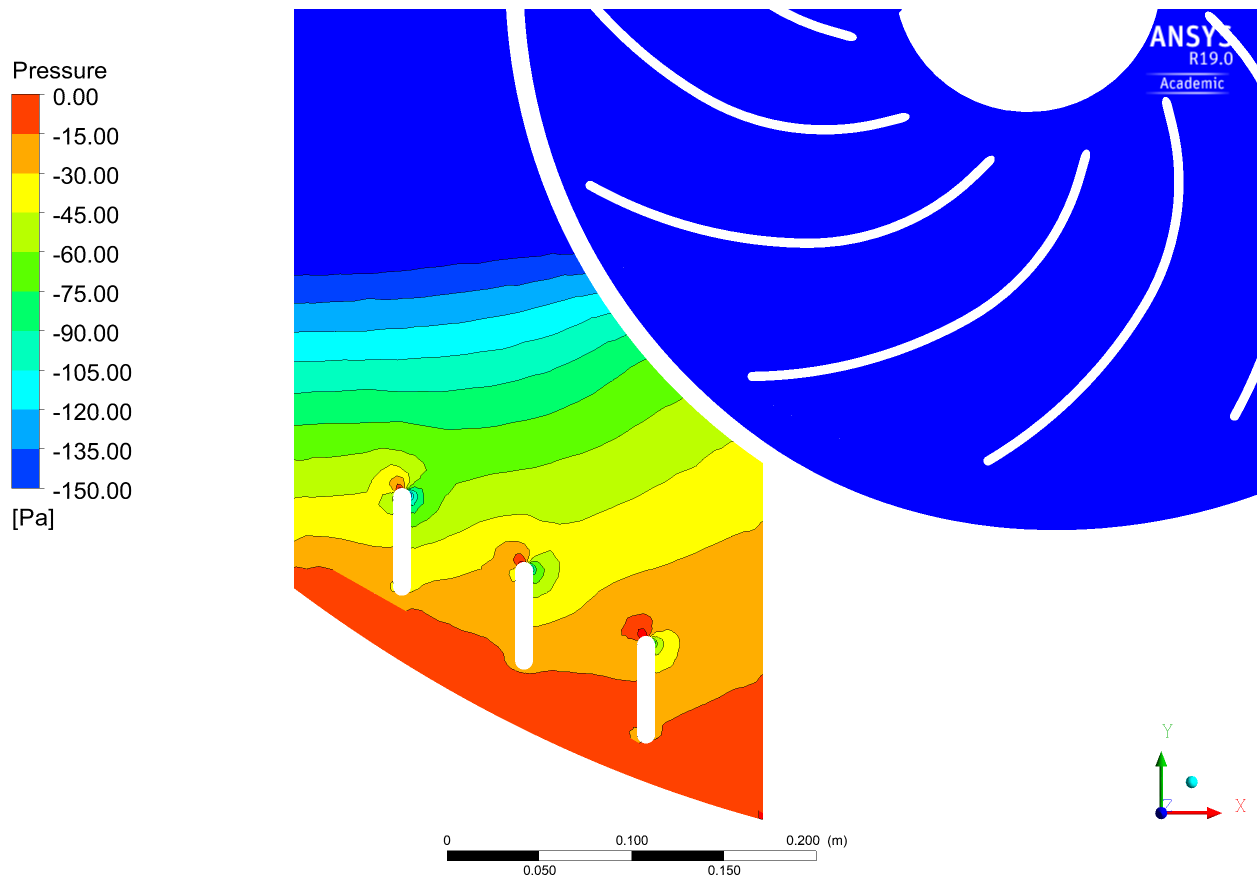


Figure 3-11: Close-up view of pressure contours in the fan volute and outlet

One of the main purposes of this simulation was to obtain the exhaust velocity profile for use as an input for the remaining simulations. Plotted in Figure 3-12 is the predicted velocity profile along the centreline of the exhaust outlet. Also, plotted for reference is the velocity profile along the centreline of the exhaust obtained experimentally. The modelled velocity profile was taken from the final time step of the simulation, after a fully developed flow was reached. By comparing the profile from the final time step to the experimentally measured profile two velocity profiles show overall good agreement, with the obvious exception of the exhaust profile in the region of 0 cm to 6 cm. Unfortunately, the project deadline did not permit additional simulations to explore the source of the difference in this region. The average variation between the two profiles was 28%; if the 0 cm to 6 cm portion of the profile is excluded the average variation drops to 10%.

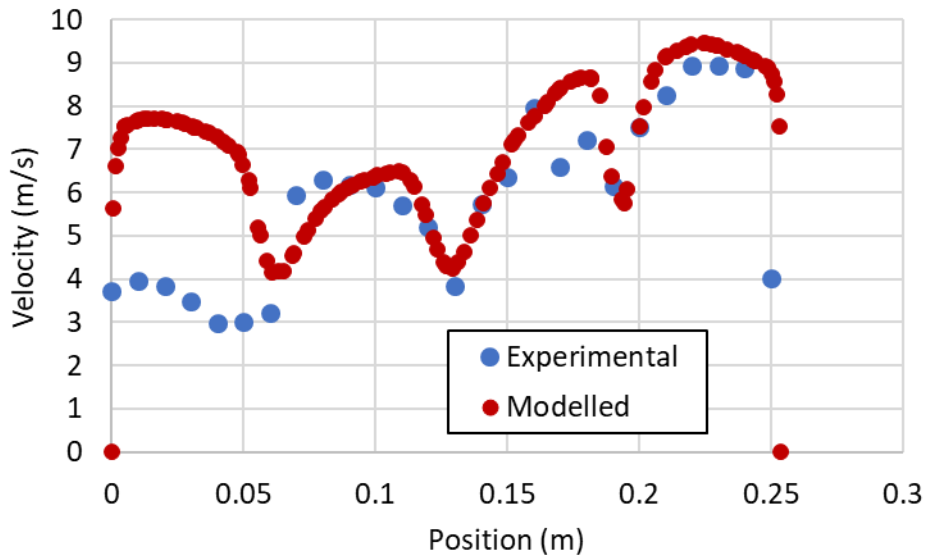


Figure 3-12: Plot of predicted and measured velocity profiles along centreline of the inverted fan's exhaust

Using the velocity profile from the fan simulation, the effect of the fan exhaust on the surrounding air flow was simulated next. Figure 3-13 and Figure 3-14, present two-dimensional cross sections with velocity contours and direction vectors, from the steady state model of the air flow around the fan, for the side view and front view of the fan, respectively. Both images show the exhaust jet exiting the fan and impinging upon the ground. The direction vectors, which are not scaled with velocity, show that as the jet leaves the fan, the surrounding air is entrained, i.e. drawing air downwards into the jet. After impinging on the ground, in the side view, the jet is shown to follow the ground. It continues to entrain the surrounding air as the flow heads towards the end of the domain. In the front view, the jet is shown entraining the surrounding air as it leaves the fan, before it impinges on the ground. Once impingement occurs, the spread of the jet along the ground is much less compared to the side view. In fact, the exterior flow is drawn inward along the ground on the right-hand side of Figure 3-13. Both figures show that velocities at the 2.0 m radius from the fan do not exceed the 2.0 m/s or 4.0 m/s limits imposed by the ISO standard described earlier.

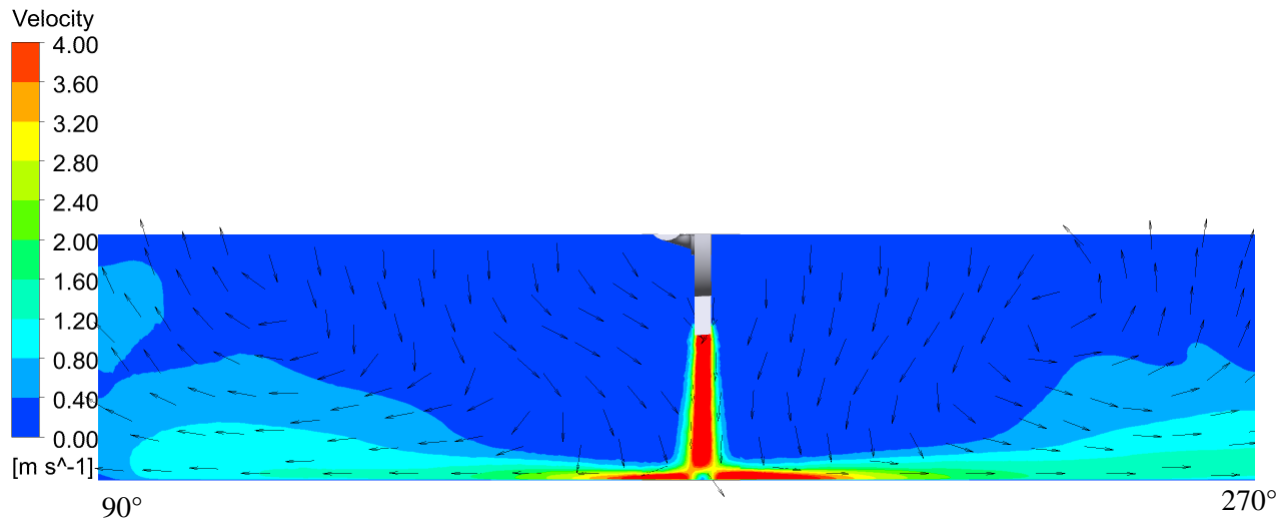


Figure 3-13: Side view of velocity contours and vectors of impinging fan exhaust

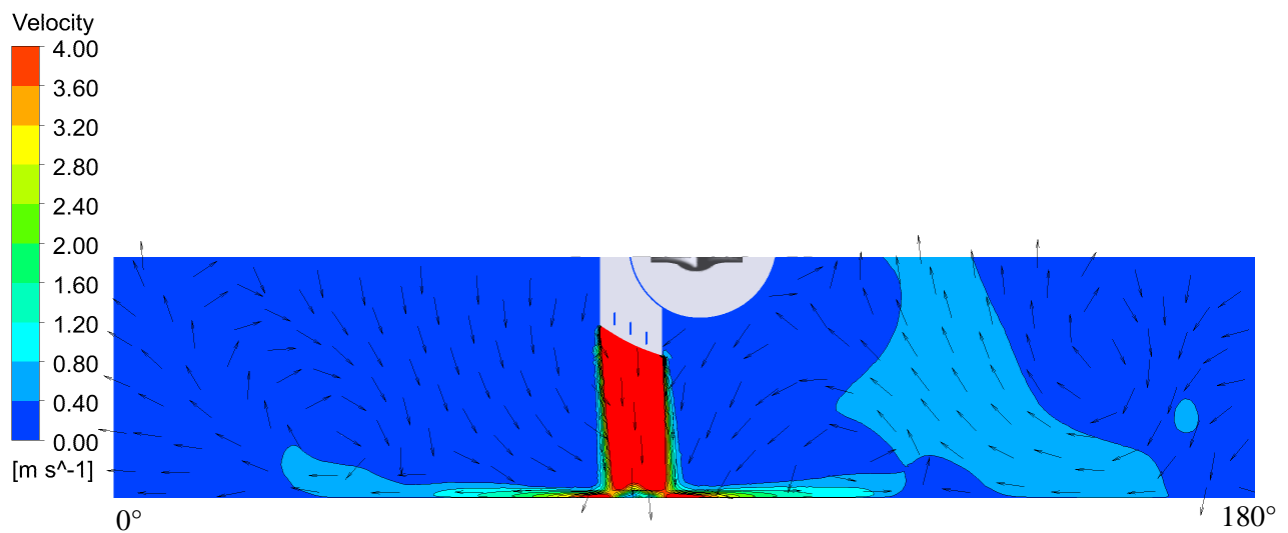


Figure 3-14: Front view of velocity contours and vectors of impinging fan exhaust

Figure 3-15 shows an isometric view of velocity contours and vectors along a plane 1 cm above the ground. As would be expected of an impinging jet, the highest velocities occur directly below the fan exhaust before the flow begins to spread out along the ground. Unlike the ideal impinging jet described in Section 2.4.1, the flow does not spread out equally in all directions. Near the point of impingement, the flow velocity spikes symmetrically on the 90°/270° axis, while the velocity distribution is asymmetric about the 0°/180° axis. The contours of the velocity field

show that more flow was directed in the 0° direction compared to the 180° direction. At the edge of the domain, the velocity magnitude is between 0.4 m/s and 1.2 m/s in the 90° and 270° directions, and is near zero in all other directions. The shape of the velocity field shown is mostly a function of the shape of the fan exhaust, with some influence from the exhaust velocity profile. For a more in-depth discussion of the effect of the exhaust parameters on the shape of the velocity field near the ground see Appendix A.

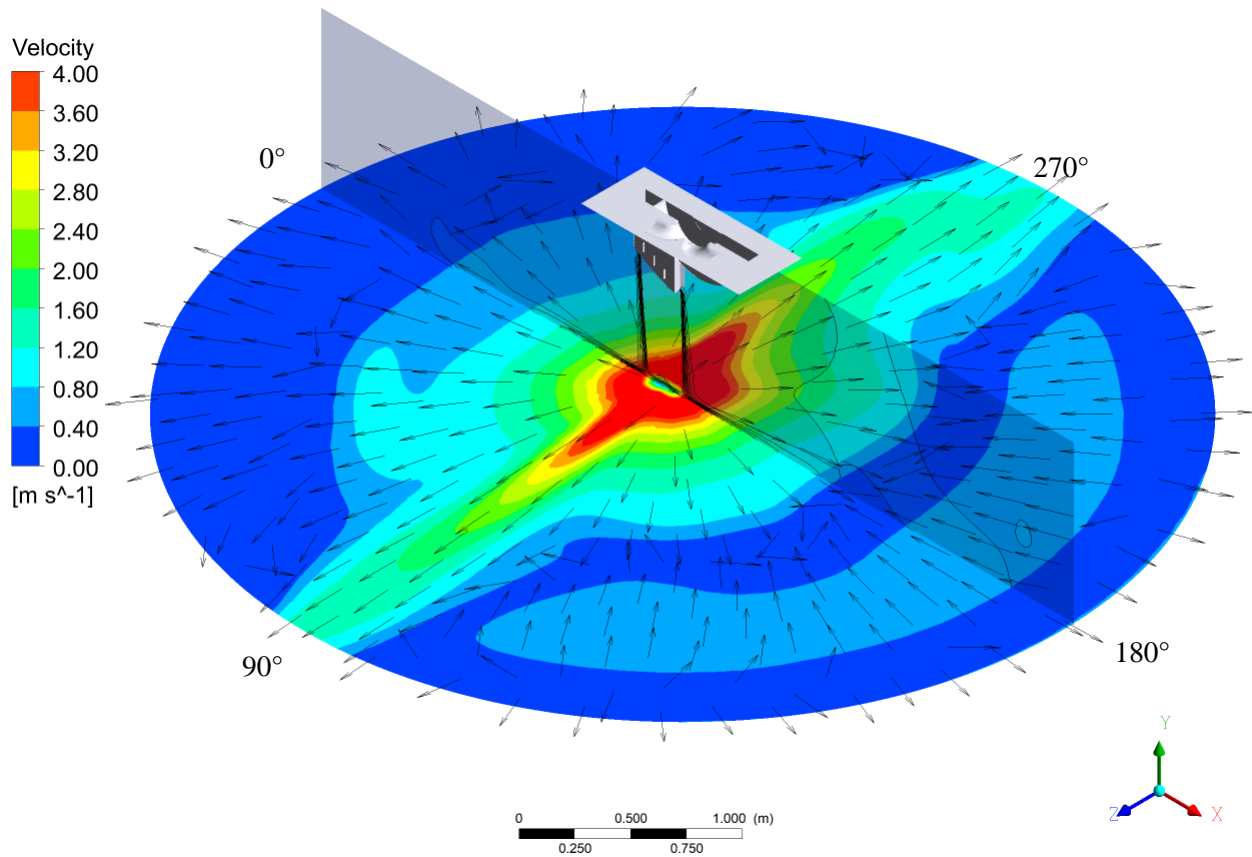


Figure 3-15: Isometric view of velocity contours and vectors at 1 cm above the ground

3.4 Fan with the 2D Square Diffuser

The simulation of the 2D square diffuser was broken into two parts. The first was a model of the diffuser itself, which directs air from the fan's exhaust around a 180° bend, through an expansion, and then discharges the air through an exhaust. It used the velocity profile at the outlet of the fan simulation as the diffuser inlet profile. The second simulation was a model of the discharge domain surrounding the combined diffuser and fan. This model used the outlet

velocity profile from the diffuser simulation as the input velocity profile, to simulate the exhaust of the diffuser impinging on the ground. In a similar manner to the inverted fan simulation, this configuration was divided into two parts to reduce the simulation run-time.

3.4.1 Two-Dimensional Square Wide-Angle Diffuser Geometry

The geometry for the diffuser model was based upon the CAD model used to construct the diffuser for the experimental section of this work. Figure 3-16 shows the geometry of the diffuser. It consisted of a single fluid domain that receives the air exhausted from the fan, turns it, and then decelerates it as it reaches the end of the diffuser.

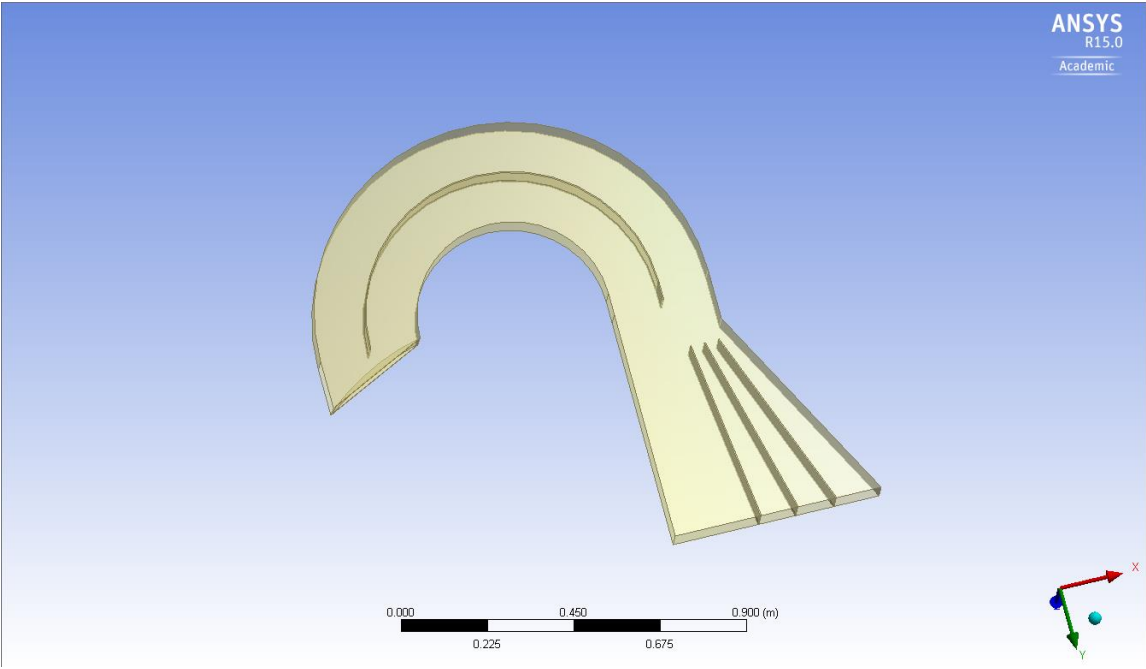


Figure 3-16: Interior view of the 2D square wide-angle diffuser geometry

Figure 3-17 shows the geometry used to model the interaction of the diffuser on the air surrounding the fan and diffuser. It consisted of a single domain: a column of air with a 2.0 m radius centred on the diffuser outlet, with the external surfaces of the fan and diffuser included as interior walls. As for the inverted fan configuration, the air was modelled to a height of 1.0 m above the ground.

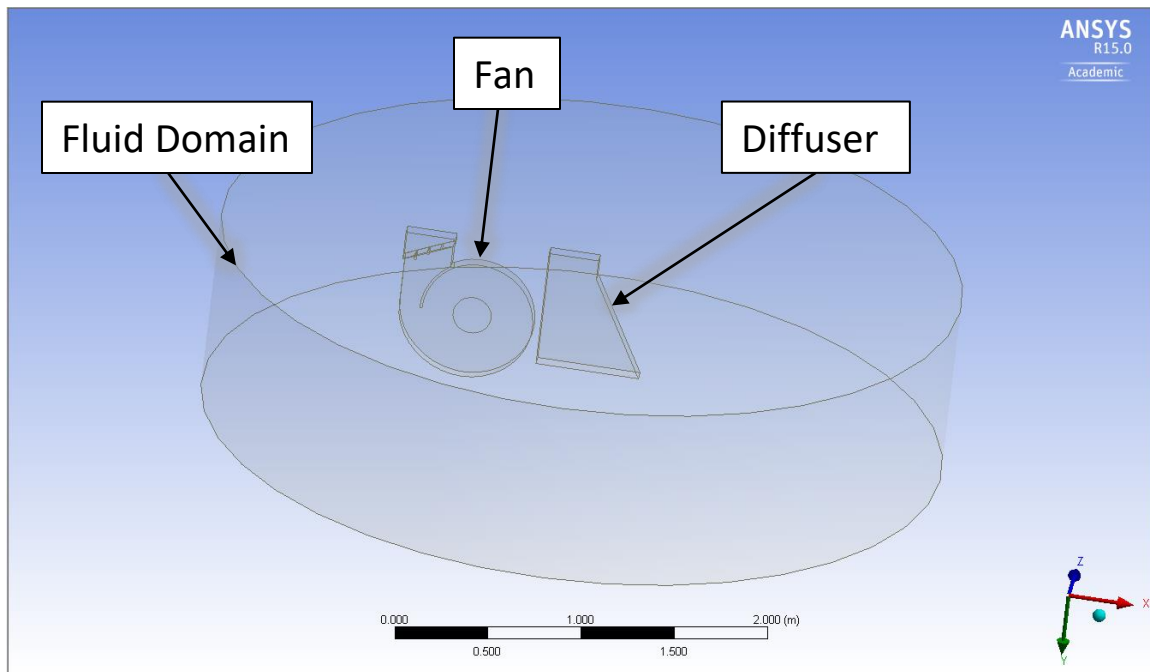


Figure 3-17: Three-dimensional view of the fluid domain surrounding the fan and diffuser

3.4.2 Mesh

ANSYS™ meshing was used to create the meshes for the diffuser and the surrounding exhaust domain. For the diffuser, an unstructured tetrahedral mesh was used, consisting of cells ranging in size from 2.6×10^{-4} m to 5.0×10^{-3} m. At the inlet face of the diffuser the element size was set to 5×10^{-3} m, while the element size at the outlet face was set to 3×10^{-3} m. This resulted in a mesh that consisted of 2,494,762 elements and had an average orthogonal quality of 0.8657 and an average skewness of 0.2128. To be able to resolve the boundary layer inside the diffuser an inflation layer was used along the outside walls, inside walls, and the turning vane. Figure 3-18 illustrates the mesh and the inflation layers.

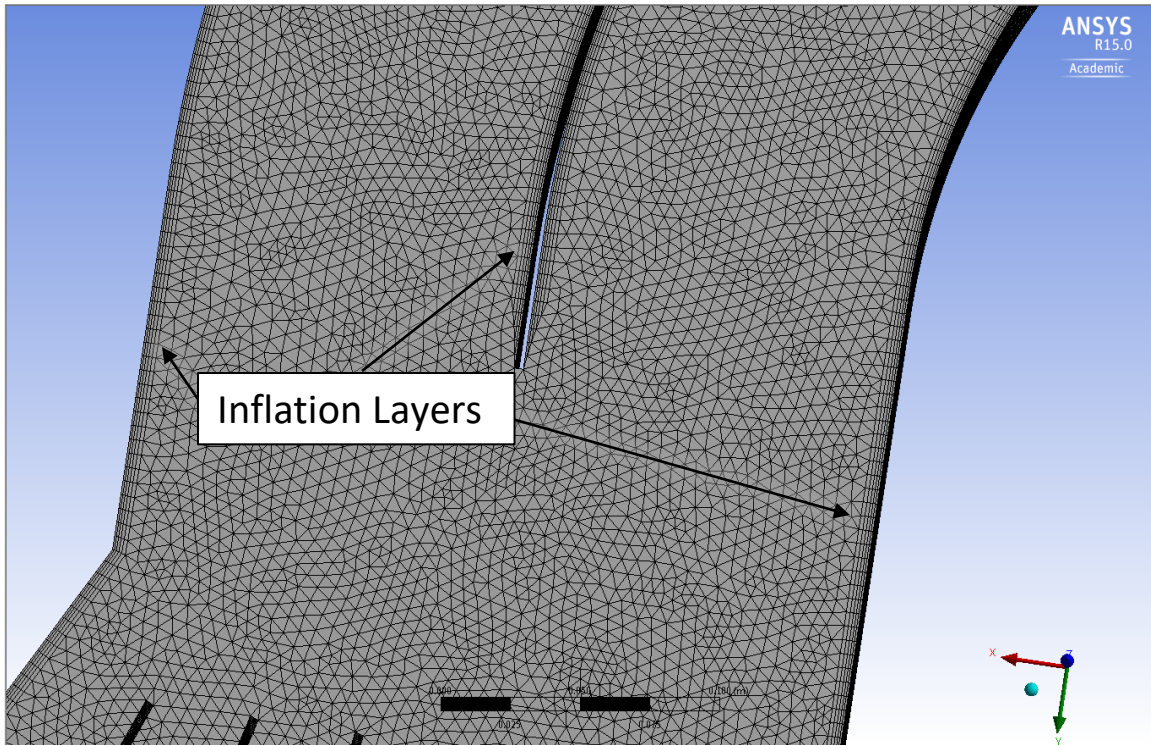


Figure 3-18: Close-up view of the diffuser mesh showing the inflation layers

Figure 3-19 shows the interior of the mesh of the discharge domain surrounding the diffuser and fan. Volume A indicates the diffuser section and fan, while volume B represents the air surrounding the diffuser and fan. This mesh consisted of an unstructured tetrahedral mesh with cells ranging in size from 5.0×10^{-3} m to 3.0×10^{-2} m. The size of the elements at the inlet face was set to 3.0×10^{-3} m. To resolve the boundary layer created by the impinging jet an inflation layer was used along the ground plane. The resulting mesh consisted of 5,158,069 elements and had average orthogonal quality of 0.8627 and an average skewness of 0.2200.

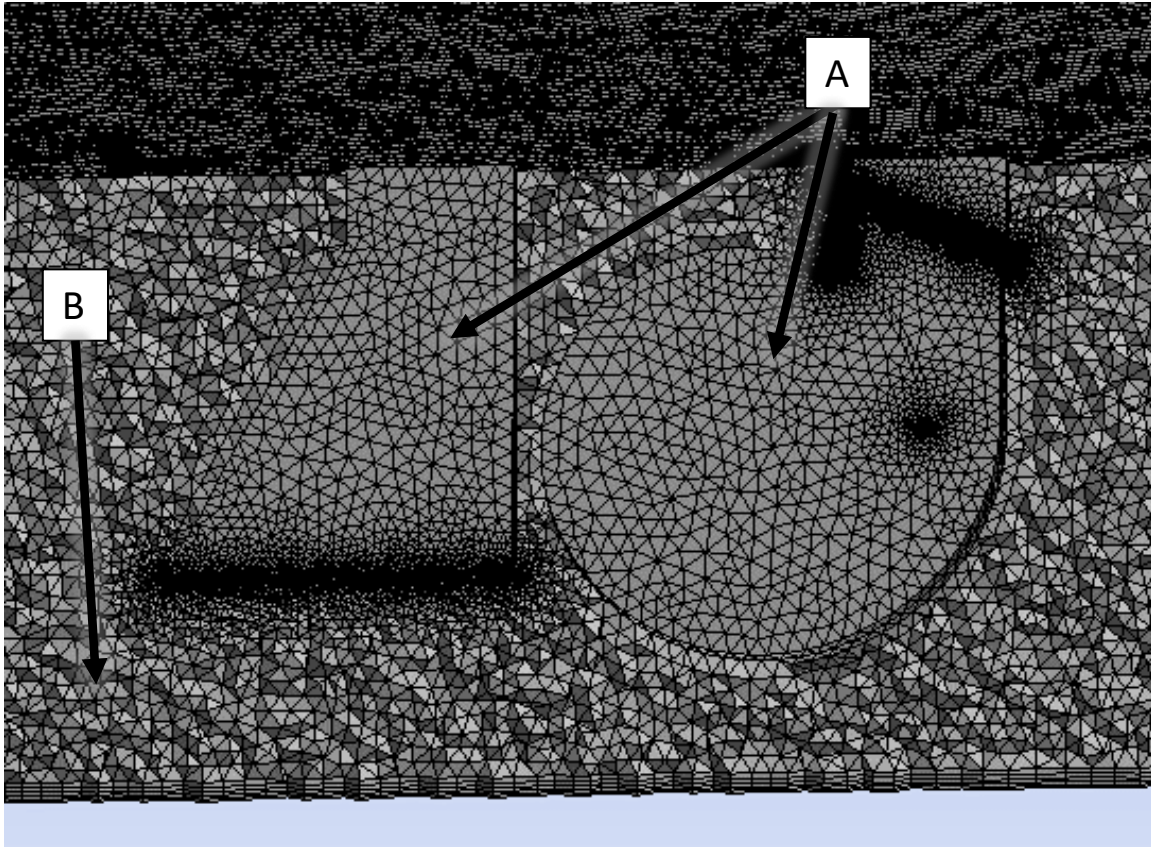


Figure 3-19: Three-dimensional view of the interior mesh of the fluid domain surrounding the diffuser and fan

3.4.3 Solution Set-up

This section presents the parameters used to model the flow through the 2D square diffuser, and to model the jet from the diffuser's exhaust and its effect on the surrounding domain.

The eddy viscosity model used for the diffuser simulation was the realizable $k-\varepsilon$ model in conjunction with a standard log-law wall treatment. The boundary conditions of the diffuser simulation were as follows: the inlet used the outlet velocity profile for the final time step from the fan simulation; the outlet was set to atmospheric pressure (95 kPa); and the walls of the diffuser used a no-slip boundary condition.

For the simulation of the air around the diffuser and fan the realizable $k-\varepsilon$ model was selected based on a recommendation from ANSYS™. The flow at the wall was modelled using a standard log-law wall treatment. The boundary conditions for this simulation were like that of the

discharge domain around the fan: a no-slip condition at the ground plane and the exterior of the fan and diffuser; the inlet was located at the diffuser exhaust and used the diffuser velocity profile; and the boundary above the fan/diffuser and at the 2.0 m radius around the fan was set as the outlet under atmospheric pressure, 95 kPa.

3.4.4 Results

Figure 3-20 shows the velocity contours and direction vectors of the flow inside the diffuser on the mid-plane of the diffuser. The highest velocities inside the diffuser occur along the outer wall. The contours show that the turning vane effectively turns the flow, with minimal stall occurring at the edge of the vane and the inside edge of the diffuser inlet. In the expanding section, some stall can be seen along the inside edge of the largest channel at location A. In the outer most expanding section, location B, the flow can be seen to be effectively decelerated from over 10 m/s down to between 6.0 to 8.5 m/s. Overall the average fan exhaust velocity of 6.95 m/s is reduced to an average velocity at the diffuser exit of 3.12 m/s, which is a 55% reduction.

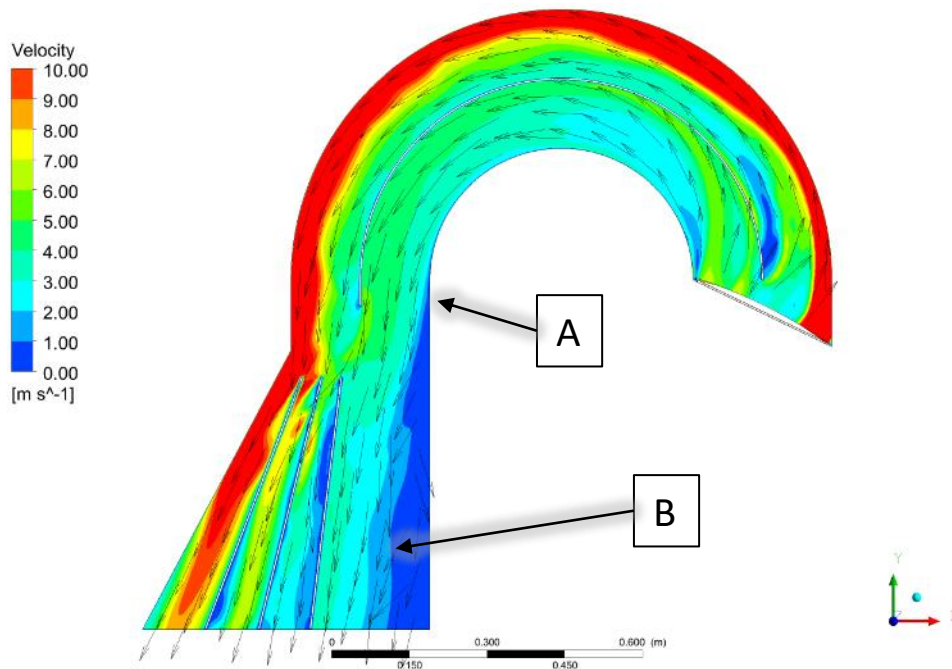


Figure 3-20: Velocity contours and vectors inside of the 2D square diffuser

Figure 3-21 shows contours of pressure in the diffuser. Comparing the diffuser velocity and pressure contours shows that the flow separation at location A, occurs as the pressure in the

exhaust transitions from negative to positive gauge pressure. This indicates that the adverse pressure gradient along the inner was sufficient to cause separation. The figure also illustrates the pressure recovery, which occurs in the expanding sections of the diffuser, with the most dramatic examples of pressure recovery occurring in the three smaller expanding sections. The static pressure in these sections increases rapidly, which is associated with the deceleration of the flow through the diffuser.

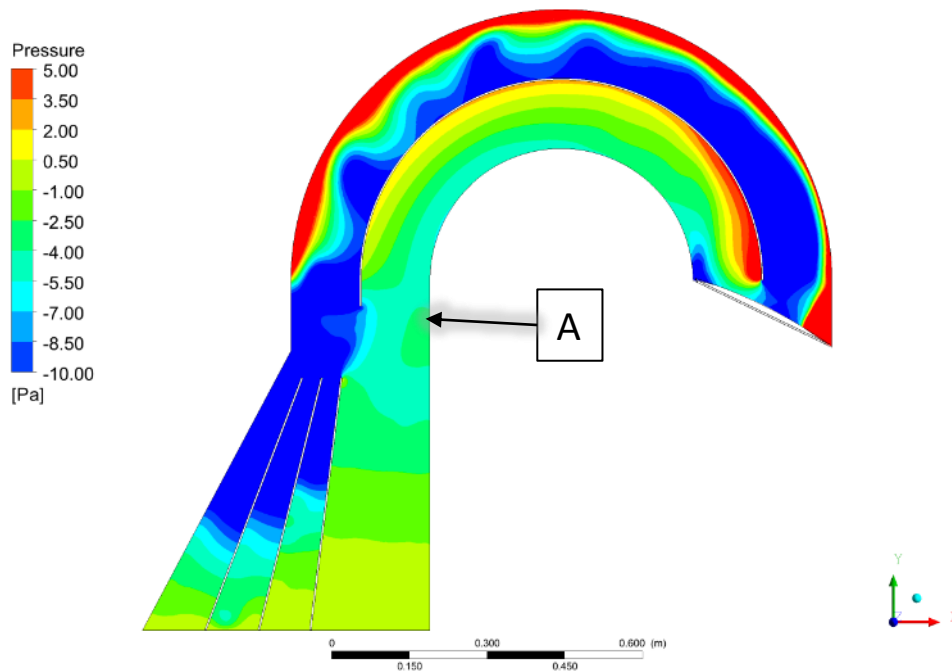


Figure 3-21: Pressure contours inside the 2D square diffuser

Plotted in Figure 3-22 is the velocity profile along the centerline of the diffuser exhaust. Also plotted is the velocity profile measured experimentally. The plot shows that the diffuser is most effective in the 0 cm to 23 cm channel and the 23 cm to 33 cm channel where it reduces the velocity to below 4.0 m/s and 2.5 m/s respectively. Overall there is good agreement in the shape of the two profiles, with the “peaks” and “valleys” lining up nicely. The variation between the average velocity of the two profiles is 6.5%.

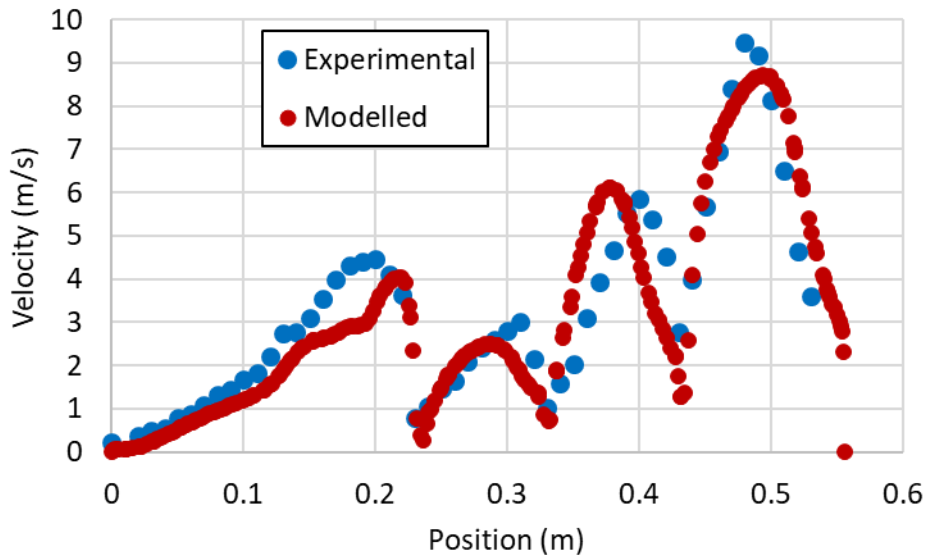


Figure 3-22: Plot of modelled and measured velocity profiles along the centreline of the diffuser exhaust

Note that in the figure above, the experimental data were corrected for the difference in flow rate. This was done because the two data sets were taken at two different fan speeds; the modelled data was for a fan speed of 3500 RPM and the experimental data was for a fan speed of 3300 RPM. When the diffuser was attached to the fan a speed of 3300 RPM was required for the experimental data to achieve 4.98 kPa of vacuum as required by the seed meters. Using the fan affinity laws, the experimental data was converted from 3300 RPM to 3500 RPM (Bleier, 1998) using the relation below:

$$\frac{Q_1}{Q_2} = \frac{N_1}{N_2} \quad (3-3)$$

where Q_1 [m³/s] is the flow rate at fan speed N_1 [RPM] and Q_2 [m³/s] is the flow rate at fan speed N_2 [RPM]. The change in fan speed was due to keeping a constant 4.98 kPa

The exhaust flow from the diffuser was modelled using the exit velocity profile from the simulation of the diffuser. Figure 3-23 is a two-dimensional cross-sectional view of the flow below the diffuser and fan using velocity contours and direction vectors. The figure shows the exhaust leaving the diffuser and impinging upon the ground. The vectors show how the surrounding air is entrained by the jet. In this plane, the jet is asymmetric and after impingement,

it continues to flow in the direction of the diffuser expansion, i.e. towards the left side of the figure, with almost no flow moving towards the fan or underneath the fan. Unlike the jet from the inverted fan, the flow along the ground from the diffuser does not separate, and follows the ground for the entire 2.0 m radius, confining all the higher velocity flow to within a few centimeters of the ground. The figure also demonstrates that the velocities at the 2.0 m radius from the fan did not exceed the 2.0 m/s or 4.0 m/s limits imposed by the ISO standard, as the only location that shows a velocity of greater than 2.0 m/s occurs directly below the diffuser outlet.

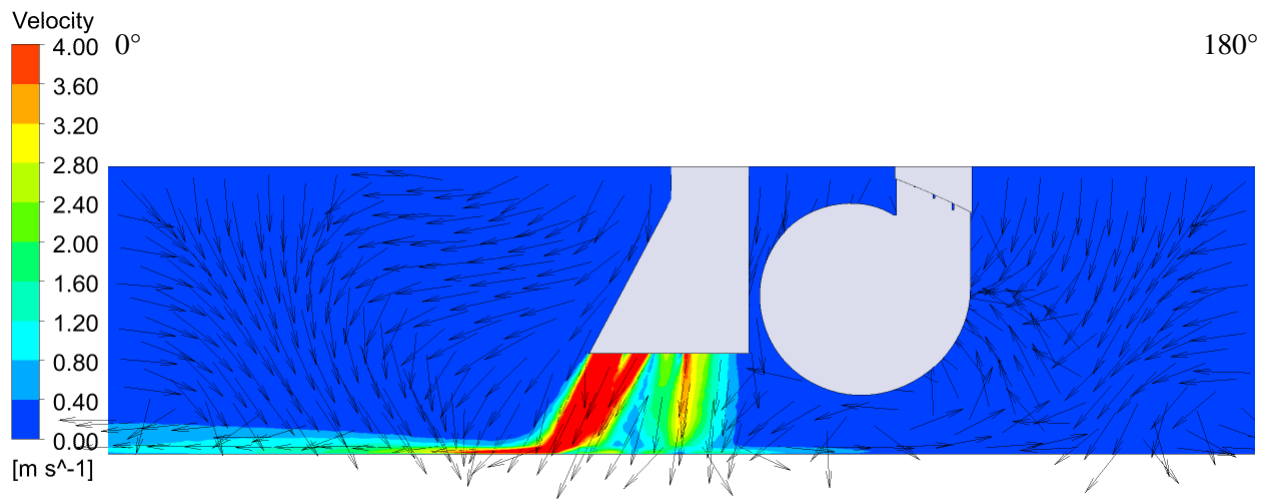


Figure 3-23: Front view of velocity contours and vectors of the impinging diffuser exhausting

Figure 3-24 shows an isometric view of velocity contours and vectors along a plane 1 cm above the ground. The highest velocities occur where the jet first meets the ground and quickly decrease afterwards. Just as for the jet from the inverted fan, the jet from the diffuser does not spread out equally in all directions. As was shown in Figure 3-23 above, most of the jet flow propagates in the 0° direction, with almost no flow propagating under the fan. This is due to the geometry of the diffuser directing the highest velocity flow to meet the ground at a 30° angle from the normal.

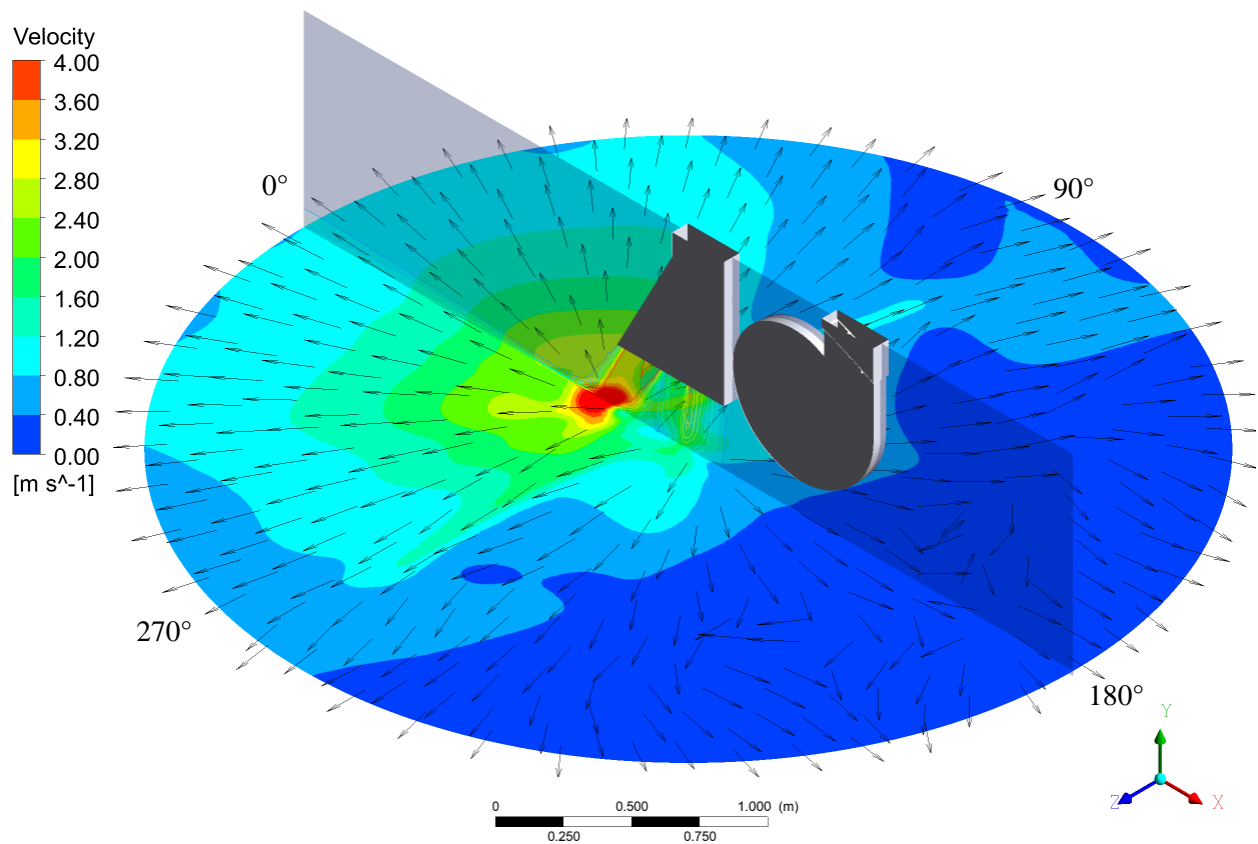


Figure 3-24: Isometric view of velocity contours and vectors at 1 cm above the ground

3.5 Chapter Summary

This chapter documents the CFD methodology used and the CFD models created to complement the experimental part of this thesis. The goal was to show that a CFD simulation for two of the three fan configurations, could be used to show compliance with the ISO 17962 standard. Both models showed that the inverted fan and the 2D square diffuser met the ISO standard. The simulations and the experimental data showed similar trends, as well as maximum values for the velocity field. This suggests that CFD can be an effective tool to assess compliance with the ISO standard.

CHAPTER 4 DISCUSSION AND ANALYSIS OF RESULTS

4.1 Introduction

The following chapter will compare the results of the experimental and simulation sections of this thesis research and both sets of data will be evaluated against the ISO 17962:2015 standard. Also, the results from the inverted fan will be directly compared to the results of the 2D square diffuser.

4.2 The Inverted Fan

The following section presents the data for the velocity field around the inverted vacuum fan. Plotted in Figures 4-1a and 4-1b are the horizontal air velocities predicted and experimentally measured at a 2-m radius around the fan. Both data sets present data points at 30° intervals around the fan at heights ranging from 10 cm to 100 cm above the ground, with the modelled data also showing points from 0 cm to 10 cm. The plots qualitatively show good agreement in predicting the peak velocities occurring at the 10-cm height at the 90° and 270° locations, as well as showing the trend of diminishing velocities as the measurement height increases. As is discussed in Appendix A, the peak velocities occurring at 90° and 270° are a result of the shape of the fan exhaust. While both sets of data indicate that the velocity tends to decrease with height, the overall agreement between the profile shapes and magnitudes is poor. Qualitatively plot *j* showed the best agreement on profile shape. For measurements in the 10 cm range the experimental values tend to have a greater magnitude at most of the measurement locations. One reason that the velocity distribution for the two data sets differ may be due to the ground differences between the model and the experiment. As discussed in Appendix A, a slight incline of the ground surface can have a noticeable effect on the velocity field just above the ground. A second reason may be that the stand that held the fan for the experiment was not modelled. The stand was assumed to have a negligible effect on the flow field, but the differences in the two data sets may indicate that this is not the case.

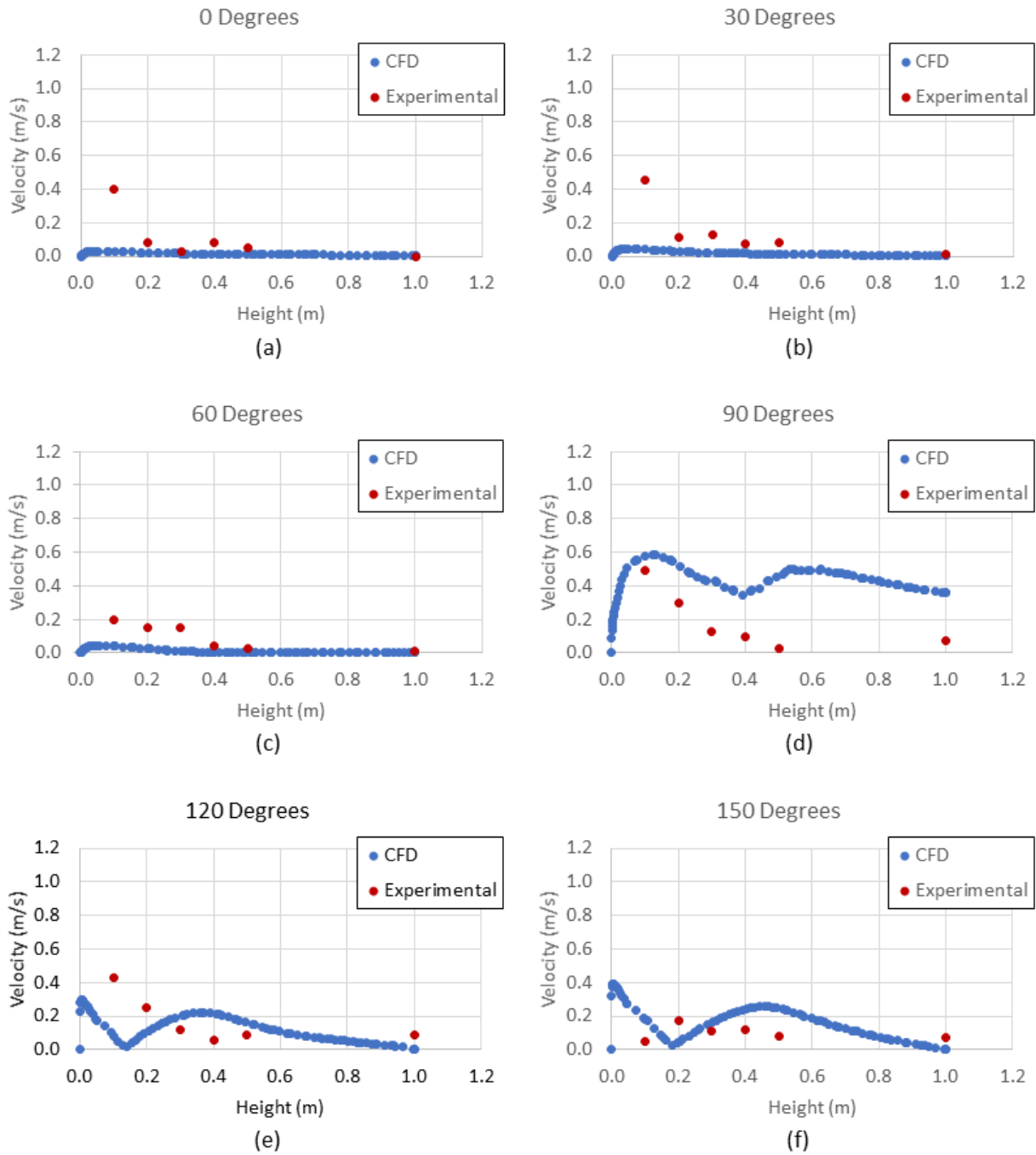


Figure 4-1a: Velocity profiles at 30-degree intervals, 2 m radius around the inverted fan

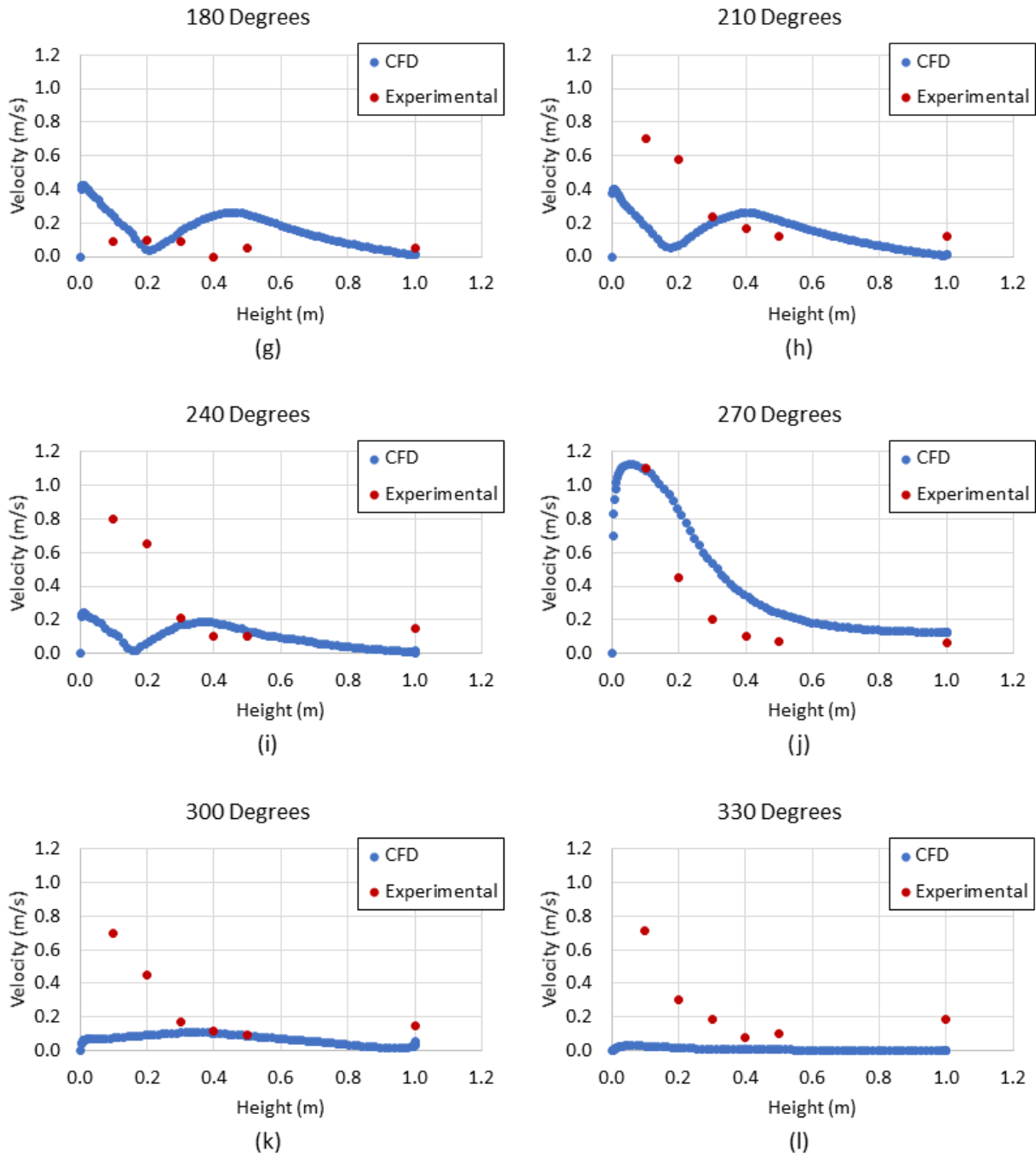


Figure 4-1b: Velocity profiles at 30-degree intervals, 2 m radius around the inverted fan

Another way to compare the two data sets is to use the concept of conservation of mass.

According to this principle, for steady flow of an incompressible fluid, the rate at which the mass of fluid enters and exits the domain must be equal. The mass flow rate is given by the following relation:

$$\dot{m} = \rho v A \quad (4-1)$$

where \dot{m} (kg/s) is the mass flow rate, v (m/s) is the average fluid velocity, and A (m²) is the area over which the flow rate is being taken. Relating this to conservation of mass:

$$\dot{m}_{in} = \dot{m}_{out} \quad (4-2)$$

which states that the mass flow rate into the system must be equal to the mass flow out of the system. Applying this relation to both the experimental system and the simulated system, and if both have the same inlet mass flow rate, implies that both should have the same exit mass flow rate. Since the density of the fluid and the outlet area of both systems are the same, then the average velocity over the outlet area should also be the same.

Table 4-1 presents a comparison of the weighted average velocity of the experimental and modelled velocity fields at the edge of the measurement domain. A weighted average was used to account for the sparse nature of the experimental data, between the 50 cm and 100 cm measurement elevations. More weight was placed on the 50 cm and 100 cm measurement locations, by using a linear interpolation, between the two elevations, at 10 cm intervals to estimate data for the 60 cm, 70 cm, 80 cm, and 90 cm measurement elevations. The velocities for all ten elevations were then averaged to calculate the average velocity for the velocity fields at the edge of the measurement domain. Comparing the two average velocities shows a small difference of 2%, which indicates a good general agreement between the experimental and modelled data.

Also presented in Table 4-1 is a comparison of the maximum measured velocity and the maximum simulated velocity. Comparing the two maximum velocities shows a small difference of 2.7%, which indicates a good agreement between the experimental and modelled data.

Table 4-1: Comparison of Experimental and Modelled Velocities for the Inverted Vacuum Fan

Parameter	Experiment	Simulation	Absolute Difference	Percent Difference [%]
Weighted Average Velocity [m/s]	0.15 ±0.01	0.147	0.003	2.00
Maximum Velocity [m/s]	1.10 ±0.1	1.130	0.03	2.72

The above data show that the CFD model can give some insight on the ability of the fan to meet the ISO standard. It correctly predicted the location of the peak velocity, it gave an indication of the magnitude of the peak velocity, and it showed good agreement on the average flow in the domain. However, there were significant and extensive differences between the measured and simulated velocity fields and the reason for these differences is not yet clear. While the model did have some trouble with resolving the details of the flow, the goal of the model was not to resolve details but to get a general picture of the effect of the fan on the surroundings and show compliance with the ISO standard, which was achieved. The above data also show that by directing the fan to exhaust towards the ground, the vacuum fan can meet the ISO 17962:2015 standard.

4.3 The Fan with the 2D Square Diffuser

The following section presents the data for the velocity field around the fan and 2D square diffuser. Plotted in Figures 4-2a and 4-2b are the horizontal air velocities simulated and experimentally measured at a 2-m radius around the diffuser. Data are presented at 30° intervals around the diffuser at heights ranging from 10 cm to 100 cm above the ground, with the simulated data also showing points from 0 cm to 10 cm. The plots qualitatively show good agreement between most of the measured and modelled data. Both data sets show the expected trend of diminishing velocities as the measurement height increases. Also, both data sets indicate that the peak velocity of the flow from the diffuser occurs in the 0° direction.

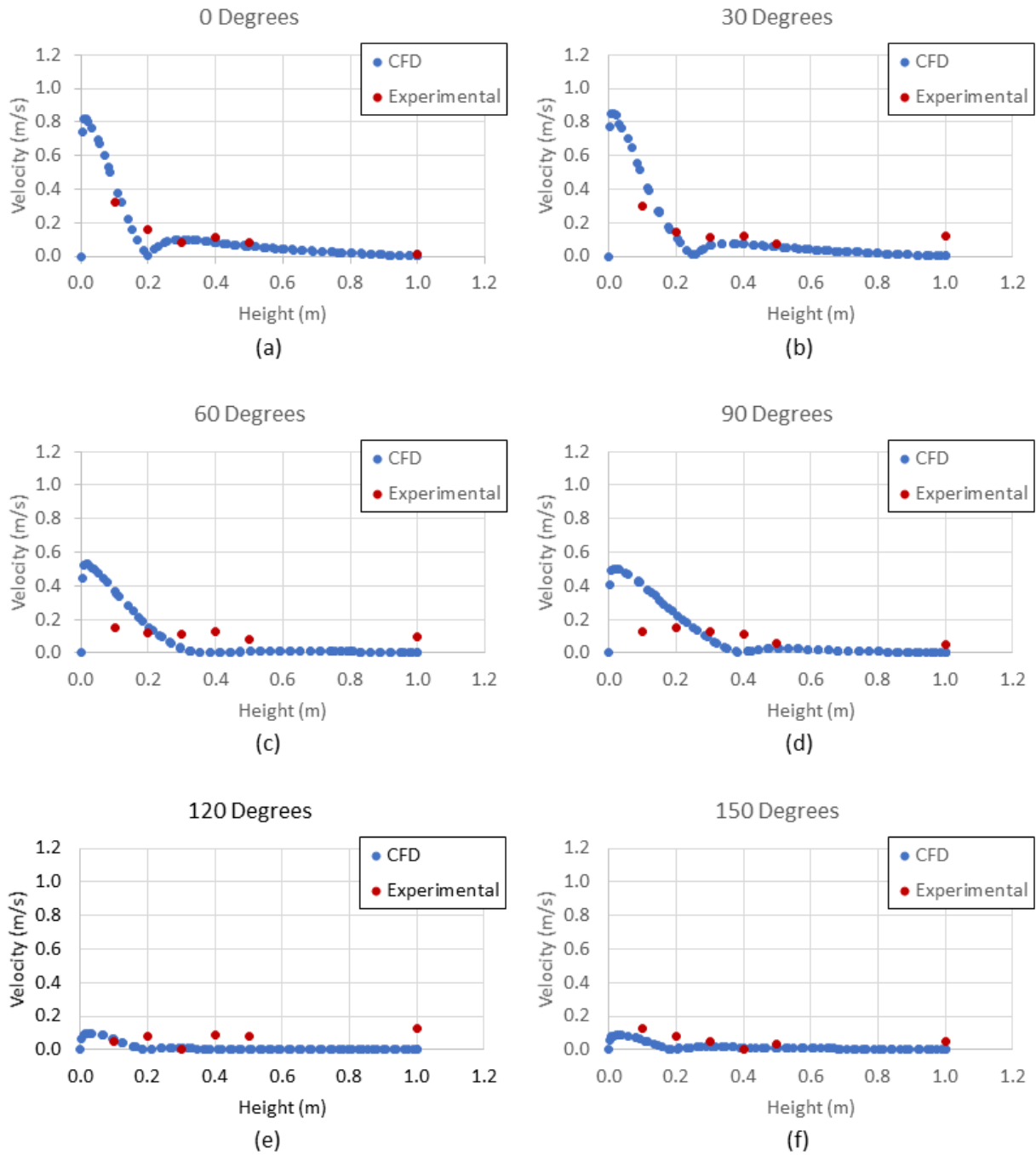


Figure 4-2a: Velocity profiles at 30-degree intervals, 2 m radius around the 2D square diffuser

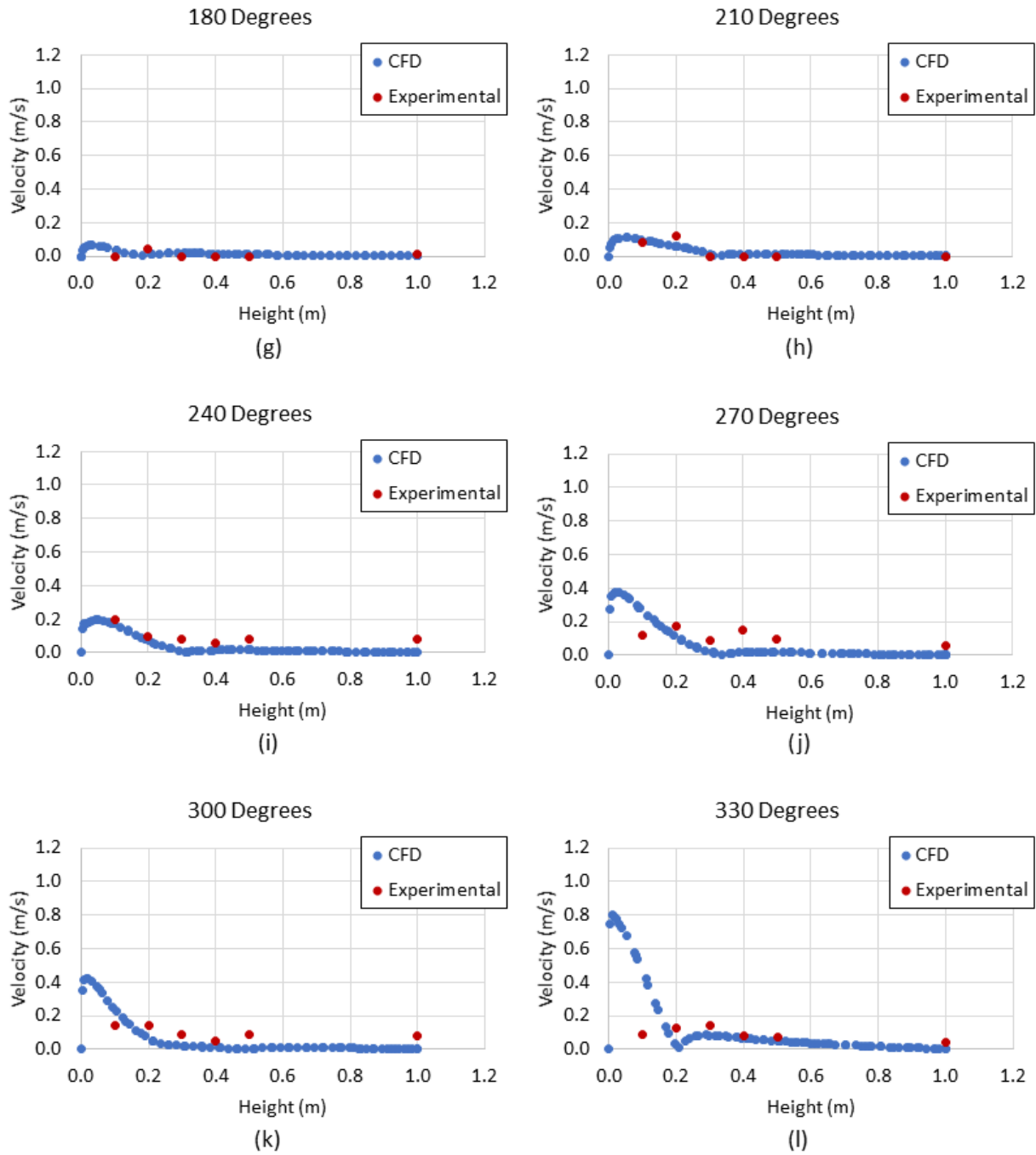


Figure 4-2b: Velocity profiles at 30-degree intervals, 2 m radius around the 2D square diffuser. According to the simulations, the velocity diminishes slowly and in a symmetrical manner as the location moves away from the 0° direction. In comparison, for the experimental data, the velocity quickly diminishes in an asymmetric manner, with the 0° and 30° locations having a very similar velocity profile. The profiles around the remainder of the measurement domain

indicate minimal flow. Regardless of the rate at which the velocity diminishes from the peak value, both data sets indicate that between the 90° and 270° locations, there is almost no flow. One reason for the difference in velocity distribution between the experimental and the modelled data, could be that the fan stand (see Figure 2-7) used to position the fan during the experiment was not included in the CFD model. The stand had a cross bar located directly below the diffuser exhaust, which may have aided in obstructing the flow near the ground. In the CFD model, there was nothing to obstruct the flow once it left the diffuser.

As mentioned previously, the location of the peak velocity in both cases is a function of the diffuser geometry. The opening of the diffuser directs the exhaust jet to impinge upon the ground at an angle, and then most of the flow continues to follow the ground in that direction.

Comparing the measured and simulated velocity profile at the location of the peak velocity, according to the simulated data the peak velocity may have occurred below the 10-cm minimum measurement elevation. In fact, in each plot, the maximum simulated velocity occurred below 10 cm. This means that the 10-cm minimum measurement elevation was likely too high to capture the true maximum velocity in the experiment.

Just as for the inverted fan mass conservation was used to quantitatively compare the average flow field of the experiment and simulation. Table 4-2 presents a comparison of the weighted average velocity of the experimental and modelled velocity field at the edge of the measurement domain. Comparing the two average velocities shows a difference of 9%, which indicates a good general agreement between the experimental and modelled data.

Also presented in Table 4-2 is a comparison of the maximum measured velocity and the maximum modelled velocity. Comparing the two maximum velocities shows a large difference of over 165%, which could indicate that the CFD model is not able to predict the maximum velocity. However, the maximum modelled velocity occurred below 10 cm, and 10 cm was the minimum elevation measured. When limiting the modelled data to a 10-cm elevation or above, the difference drops dramatically to 25%.

Table 4-2: Comparison of Experimental and Modelled Velocities for the 2D Square Diffuser

Parameter	Experimental Data	Modelled Data	Absolute Difference	Percent Difference [%]
Maximum Velocity [m/s]	0.32 ±0.01	0.85	0.53	165
Maximum Velocity [m/s] (> 10 cm elevation)	0.32 ±0.01	0.40	0.08	25.0
Weighted Average Velocity [m/s]	0.078 ±0.01	0.071	0.007	9.0

The results above indicated that the CFD model can only provide limited insight on the ability of the diffuser to meet the ISO standard. It correctly predicted the location of the peak velocity, it gave an indication of the magnitude of the peak velocity (above 10 cm), and predicted an average velocity that was within 10% of the experimental value. It also indicated that by directing the fan exhaust towards the ground using the diffuser, the vacuum fan can meet the ISO 17962:2015 standard, without extensive modification of the planter.

4.4 Comparison of the Fan and 2D Square Diffuser

From the data presented in Sections 4.2 and 4.3 either inverting the vacuum fan or installing the 2D square diffuser allows the fan to meet the ISO standard. However, the intent of the ISO standard is not simply to minimize air velocities around the fan, but to minimize the environmental effects of the fan exhaust. One of these effects that was previously identified was the possibility of fugitive seed coating to be dispersed by the fan. This section will show that the addition of the diffuser is superior in minimizing such environmental effects as compared to simply inverting the fan. As the previous sections have shown that the CFD predictions in terms of the average velocities, peak velocities, and peak velocity locations is comparable to the experimental data, the simulated data will be used to compare the inverted fan to the diffuser. However, there are numerous significant differences between the measured and simulated velocity fields for both configurations. Therefore, while this comparison will provide some insight it will not be definitive.

The first metric of comparison will be the average velocity of the air at the periphery of the measurement domain, which can also be referred to as the average system outlet velocity. Table

4-3 gives a comparison of these velocities and shows that the average outlet velocity from the diffuser is over 50% lower compared to the inverted fan. According to mass conservation, the inlet mass flow rate into the system must be equal to the exit mass flow rate leaving the system. However, the same mass flow rate is supplied by the fan for both cases. This means that the mass of air entrained by the exhaust jets, and transported into the domain, must be different. Looking at the average exhaust velocities, the diffuser exhaust is also more than 50% slower. Therefore, the faster exhaust jet from the inverted fan will entrain more air into the system. This increased air entrainment is an indication of a greater potential environmental effect from the inverted fan. In contrast the diffuser reduces the amount of air passing through the domain, minimizing the potential for fugitive seed coatings to be dispersed.

Table 4-3: Comparison of Velocities of the Inverted Fan and 2D Square Diffuser

Parameter	Inverted Fan	2D Square Diffuser	Absolute Difference	Percent Difference [%]
Average System Outlet Velocity [m/s]	0.147	0.071	0.076	-51.7
Average Exhaust Velocity [m/s]	6.95	3.12	3.83	-55.1

By examining the velocity field at the ground plane, the difference in the two configurations becomes even more evident. Figure 4-3 shows a top-down view of the velocity contours and direction vectors at 1 cm above the ground under the inverted fan. As previously shown, the fan exhaust jet spreads symmetrically along the 90°/270° axis, with the highest velocities occurring directly under the fan where the exhaust jet impinges on the ground.

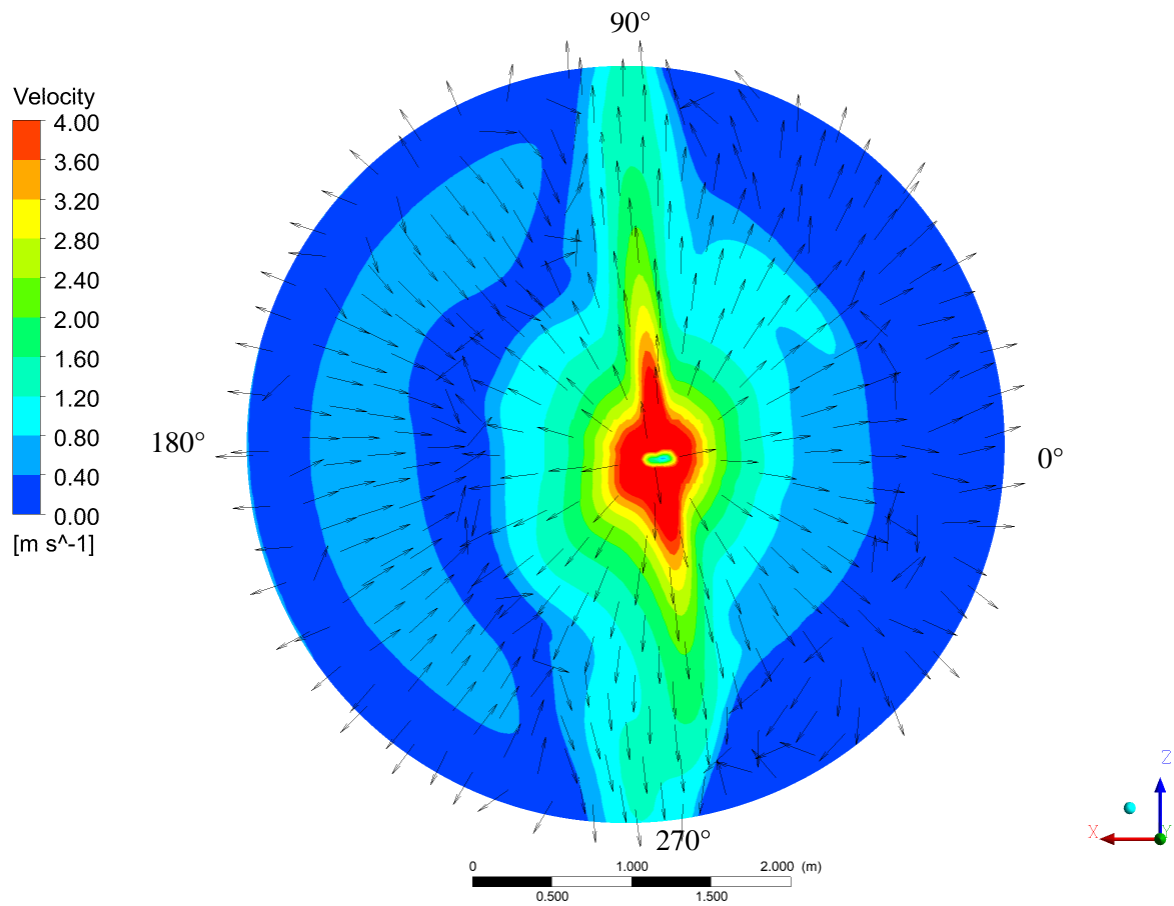


Figure 4-3: Top-down view of velocity contours and vectors at 1 cm above the ground for the inverted vacuum fan

Figure 4-4 shows a top-down view of the velocity contours and direction vectors at 1 cm above the ground under the diffuser. The highest velocities occur at the point the jet from the outer most expanding section of the diffuser impinges upon the ground. Most of the flow is directed in the 0° direction of the domain (direction of diffuser expansion), and almost no flow goes in the 180° direction.

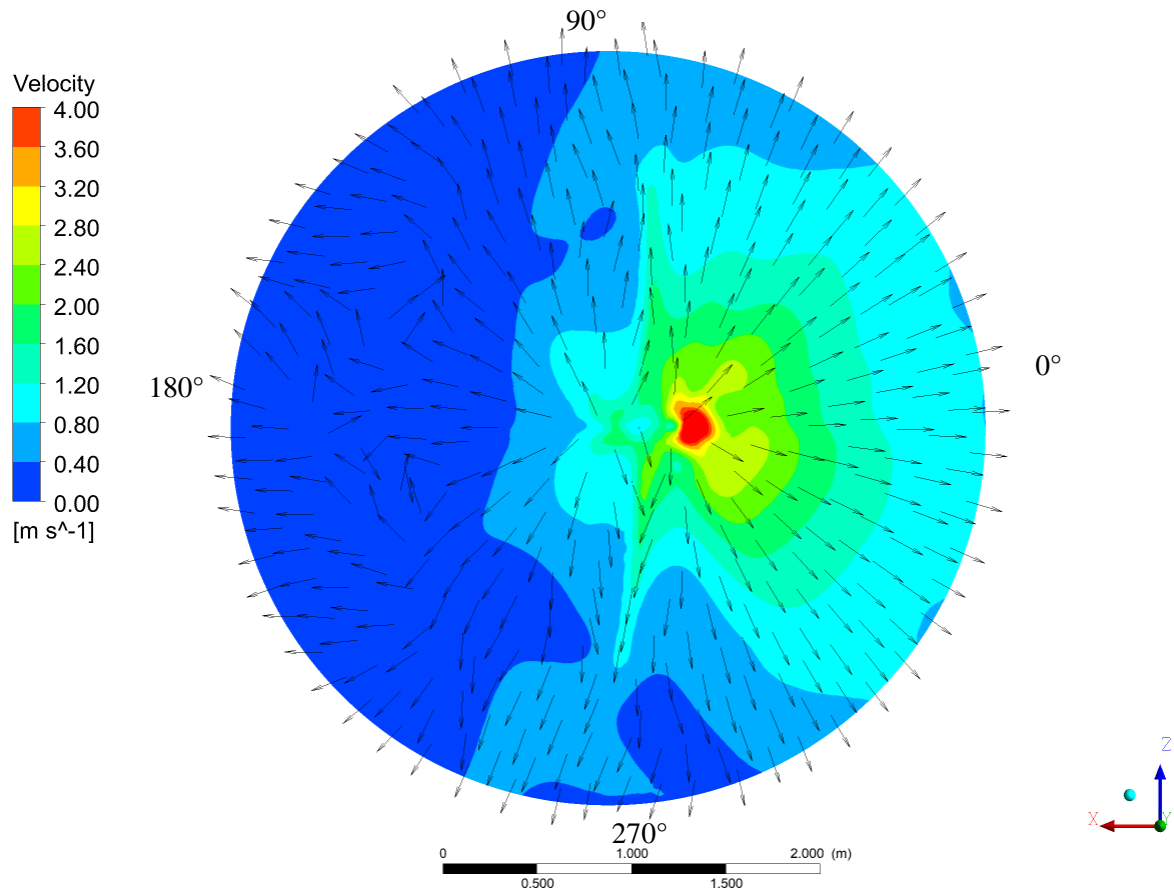


Figure 4-4: Top-down view of velocity contours and vectors at 1 cm above the ground for the 2D square diffuser

Comparing the velocity distributions near the ground for both configurations shows that the area over which the highest velocities (red contours) occur is greatly reduced for the diffuser. The highest velocity area under the inverted fan covers 2.5% of the total ground area, while the high velocity area under the diffuser covers just 0.3%, a reduction in area of almost 90%. In addition to creating less disturbance in the surrounding air, this indicates that after impinging upon the ground, the flow would have less potential to disturb and transport any seed coatings that had previously fallen to the ground.

4.5 Summary of Chapter

This section compared the experimental and modelled results of the inverted vacuum fan and the 2D square diffuser in terms of the velocity field at a 2-m radius from the exhaust. It was found

that the CFD simulations adequately modelled the effects of both exhaust jets on their surroundings. However, there were also significant differences between the CFD predictions for the velocity field and the limited experimental results, which require further investigation. Also, comparing the effects on the surroundings suggested that diffuser would create less of an impact on the surroundings than the inverted fan.

CHAPTER 5 CONCLUSION AND RECOMMENDATIONS

5.1 Conclusion

In 2015, the International Organization for Standardization, ISO, published ISO 17962:2015 Agricultural machinery - Equipment for sowing - Minimization of the environmental effects of fan exhaust from pneumatic systems, to minimize the environmental effects of planter (or seeder) fan exhaust. It establishes a limit on the air velocity created by the discharge of a fan measured around a circumference with a 2-m radius from the fan. To meet the standard the air velocity must be lower than either 2 m/s or 4 m/s depending on the measurement height above the ground, with the higher limit enforced for lower heights. The main goal of this work is show that it is possible for the CNH Industrial planter fan to meet the ISO 17962 standard. There was also a secondary goal of this work, which is to show that a numerical model (Computational Fluid Dynamics or CFD), which is not fully validated, can be an effective a tool to assess compliance with the ISO standard. The purpose of the CFD model was to show the overall air flow pattern and give insight into where the high velocities are located and provide an approximate value of the magnitude of those velocities, so the model can aid in determining compliance with the ISO standard.

The first part of this thesis research was to experimentally verify the ability of the fan to meet the standard, by measuring air velocities at a 2-m radius around it. To accomplish this, three fan configurations were designed and built. The first configuration was comprised of removing the fan from the planter and inverting it so the exhaust was directed towards the ground. This allowed the fan exhaust to be directly measured against the ISO standard and provided a baseline for measuring the effectiveness of the other configurations. The second configuration was comprised of attaching a 2D square diffuser to the fan that would both re-direct the exhaust flow to the ground and reduce the velocity. The third configuration was comprised of attaching a manifold diffuser to the fan that directed the exhaust to the ground by discharging it through multiple outlets, with the goal of producing multiple slower exhaust jets. For each of the three configurations, the highest velocities measured were 1.10 m/s for the inverted fan, 0.32 m/s for the 2D square diffuser, and 0.21 m/s for the manifold diffuser. All are within the allowable range

specified in the standard and therefore meet the requirement. However, while all three configurations could meet the intent of the standard, the manifold diffuser did not function as expected in terms of the flow distribution through the exhaust ports and would need further refinement before becoming a viable option. The major flaw with the design of the manifold diffuser was that the pressure loss at the outlets was insufficient to ensure that the flow was equally distributed between them. This resulted in uneven exhaust flow rates and higher than expected peak velocities. While the inverted fan could meet the standard (see Appendix B), it is not a simple solution since it would require a major redesign of the planter. Instead, the 2D square diffuser represented the most practical solution.

The second part of the thesis research was to create a computational fluid dynamics (CFD) model of the inverted fan and the 2D square diffuser. The manifold diffuser was excluded from this part of the work, as the design required further refinement. Both CFD models were implemented in two parts to reduce simulation times. The first part was a model of the airflow through the fan or 2D square diffuser; then the outlet velocity profile for each of these models was used to simulate the effects on a domain contained within a 2-m radius around the exhaust jet for the fan and diffuser. The results were assessed against the ISO standard, which both models met and exceeded. They were also compared against the equivalent experimental scenarios. Both models showed agreement with the experimental data in terms of the prediction for the peak velocity magnitudes and locations, as well as showing similar trends in the velocity distribution. However, there was significant differences in the actual velocity profiles taken at the periphery of the measurement domain. Quantitatively the experimental and modelled results were within 2% and 9% of the average exit velocity, for the inverted fan and diffuser respectively. The combination of predicting the high velocity locations, their magnitudes and the average effluent velocity indicated that both models met the goal of being useful tools to measure compliance with the ISO standard.

Finally, the environmental effects of the inverted fan and the diffuser were compared to each other. This comparison was done using the results of CFD models. It showed that the 2D square diffuser greatly reduced the fan's environmental impact on the surrounding air domain in two ways. First, the slower exhaust jet entrained 50% less air, meaning the diffuser decreased the ability of the fan to draw air into the domain. Second, comparing the velocity fields at a plane 1

cm above the ground, showed that the diffuser reduced the regions of high momentum in the plane by 90%. By reducing the amount of entrained air, and reducing the velocities near the ground, the diffuser reduced the potential of the fan to spread fugitive seed coating into the environment.

5.2 Recommendations

Based on the work completed as part of the thesis research the following recommendations are put forth:

1. While the 2D square diffuser met the ISO standard and outperformed the inverted vacuum fan, its design requires further refinement. The CFD model showed that the high velocity flow was confined to one side of the diffuser. It is recommended that the design be refined to better distribute the fan exhaust flow over the cross-section of the diffuser. This may be accomplished by varying the orientation of the turning vane in the 90° bend of the diffuser.
2. The manifold diffuser was found to have great promise in producing a benign exhaust flow, however, it still requires further refinement to perform properly. Further research should be done to refine the design. One way to refine the design would be to properly size the outlets so that the flow through each of the outlets is balanced and the whole outlet area is used effectively. This could be accomplished by reducing the outlet sizes to provide increased head loss, increasing the number of outlets, and fully closing the end of the manifold.
3. With regards to the effect of the fan exhaust on the environment, the ISO standard stipulated directing the fan exhaust towards the ground, however, little thought was given to how this would affect the resultant lift and transport of dust. It is recommended that further research be done to ensure that directing the exhaust to the ground does not cause excessive dust and particle lift in the air negating any benefit from the ISO standard.

4. There is an opportunity to improve the comfort of the operator of the planter. As testing was being performed it was noted that the sound levels generated by the fan could easily exceed 80 db. Since work is being done on modifying the vacuum fan it, it may be possible to include some features that result in sound attenuation. It is recommended that research into adding a sound attenuation feature into a diffuser or flow redirection device for the fan exhaust be pursued. See Appendix B for further discussion.

5. After this project was completed, CNH Industrial redesigned the vacuum fan casing and created a refined air diffuser and vacuum fan hybrid based on this work. The new fan has been in production since 2017, is more compact, has a reduced noise output, and meets the ISO standard (see Appendix B). Subsequent data collection (for model validation purpose) of the hybrid air diffuser and vacuum fan is recommended.

REFERENCES

- ANSYS™ Inc. (2013a, May 7). Lecture 7: Mesh Quality & Advanced Topics. *Introduction to ANSYS™ meshing*. Houston, TX.
- ANSYS™ Inc. (2013b, May 7). Introduction to ANSYS Fluent™ Lecture 2: Introduction to the CFD Methodology. Houston, TX.
- AMCA and ASHRAE. (1985). ANSI/AMCA 210-85 Laboratory Methods of Testing Fan Rating. Arlington Heights, IL: AMCA/ASHRAE.
- Bleier, F. (1998). *Fan Handbook: Selection, Application, and Design*. New York: McGraw-Hill.
- Carlson, J., Johnston, J., & Sagi, C. (1967). Effects of Wall Shape on Flow Regimes and Performance in Straight, Two-Dimensional Diffusers. *Journal of Basic Engineering*, 89, 151-160.
- Chong, T., Joseph, P., & Davies, P. (2008). A Parametric Study of Passive Flow Control for a Short, High Area Ratio 90 deg Curved Diffuser. *Transactions of the ASME, Journal of Fluids Engineering*, 139, 1-12.
- CNH Industrial. (2014). Early Riser 5 Series Planter Brochure. (CIH01031401).
- Cochran, D., & Kline, S. (1958). TN 4309 Use of Short Flat Vanes for Producing Efficient Wide-angle 2D Subsonic Diffuser. Washington, DC: NACA.
- Coleman, H., Steele, W. (1989) *Experimentation and Uncertainty Analysis for Engineers*. Hoboken, NJ: John Wiley & Sons Inc.
- Corsini, A., Delibra, G., & Sheard, A. (2013). A Critical Review of Computational Methods and Their Application in Industrial Fan Design. *ISRN Mechanical Engineering*, 2013, 1-20.
- Dick, E., Vierendeels, J., Serbruyns, S., & Vande Voorde, J. (2001). Performance Predictions of Centrifugal Pumps with CFD-Tools. *Task Quarterly*, 5(4), 579-594.
- Fluent Inc. (2001). *Chapter 10. Modeling Turbulence*. Retrieved from <http://www.afs.enea.it/fluent/Public/Fluent-Doc/PDF/chp10.pdf>.
- Fluent Inc. (n.d.). *Realizable k-epsilon Model*. Retrieved from <http://aerojet.engr.ucdavis.edu/fluenthelp/html/ug/node480.htm>.
- Gjernes, T. (2014). Optimization of Centrifugal Slurry Pumps through Computational Fluid Dynamics. Master's Thesis, Simon Fraser University, School of Mechatronic Engineering.

- Gonzalez, J., Fernandez, J., Blanco, E., & Santolaria, C. (2002). Numerical Simulation of the Dynamic Effects Due to Impeller-Volute Interaction in a Centrifugal Pump. *Transactions of the ASME Journal of Fluids Engineering*, 124, 348-355.
- Gopaliya, M. K., & Chaudhary, K. (2010). CFD analysis of performance characteristics of Y-shaped diffuser with combined horizontal and vertical offsets. *Aerospace Science and Technology*, 14, 338-347.
- Gülich, J. F. (2010). *Centrifugal Pumps* (2nd ed.). Berlin, Germany: Springer.
- Hummad, F., & Jadallah, A. (2007). An Experimental Verification of the Effect on Boundary Layer Suction on the Different Angle Diffusers. *Tikrit Journal of Engineering Science*, 14(4), 66-86.
- International Organization for Standardization. (2015). ISO 17962:2015 Agricultural machinery -- Equipment for sowing -- Minimization of the environmental effects of fan exhaust from pneumatic systems. Geneva Switzerland: International Organization for Standardization.
- Kline, S., Abbot, D., & Fox, R. (1959). Optimum Design of Straight-Walled Diffusers. *Journal of Basic Engineering*, 81, 321-331.
- Kurokawa, J., Imamura, H., & Choi, Y.-D. (2010). Effect of J-Groove on the Suppression of Swirl Flow in a Conical Diffuser. *Transactions of the ASME Journal of Fluids Engineering*, 132, 1-8.
- Liu, Q., Qi, D., & Moa, Y. (2006). Numerical Calculation of Centrifugal Fan Noise. *Journal of Mechanical Engineering Science*, 220, 1167-1177.
- Luo, J., & Razinsky, E. (2009). Analysis of Turning Turbulent Flow in a 180 deg Turning Duct with and without Guide Vanes. *Transactions of the ASME Journal of Turbomachinery*, 131, 021011.1 - 021011.10.
- MacCormack, R. (2014). *Numerical Computation of Compressible and Viscous Flow*. AIAA Education Series. AIAA.
- Madsen, J., Shyy, W., & Haftka, R. (2000). Response Surface Techniques for Diffuser Shape Optimization. *AIAA Journal*, 38(9), 1512-1518.
- Majidi, K. (2005). Numerical Study of Unsteady Flow in a Centrifugal Pump. *Transactions of the ASME Journal of Turbomachinery*, 127, 363-371.
- Montgomery, D. C., & Runger, G. C. (2007). *Applied Statistics and Probability for Engineers* (4th ed.). Hoboken, NJ: John Wiley & Sons Inc.

- Moran, M., & Shapiro, H. (2008). *Fundamentals of Engineering Thermodynamics*. (6th ed.). Hoboken, NJ: John Wiley & Sons Inc.
- Morre, C., & Kline, S. (1958). TN 4080 Some Effects of Vanes and of Turbulence in 2D Wide-angle Subsonic Diffusers. Washington DC: NACA.
- Mott, R. (2005). *Applied Fluid Mechanics* (6th ed.). Upper Saddle River, NJ: Prentice Hall.
- Paul, A., Ranjan, P., Patel, V., & Jain, A. (2013). Comparative studies on flow control in rectangular S-duct diffuser using submerged-vortex generators. *Aerospace Science and Technology*, 28(1), 332-343.
- Petit, O., & Nilsson, H. (2013). Numerical Investigations of Unsteady Flow in a Centrifugal Pump with a Vaned Diffuser. *International Journal of Rotation Machinery*, 2013, 1-14.
- Reagan, M. (1990). Effect of Riblets on Pressure Recovery in a Straight-Walled Diffuser. Master's Thesis, USAF Air Force Institute of Technology, Aeronautical Engineering.
- Roberge, M., & Posselius, J. (2012). Agricultural combine with on-board baler and dust suppression capability. Patent No. US8313362 B2.
- Shih, T., Liou, W., Shabbir, A., Yang, Z., & Zhu, J. (1994). TM 106721 A New k-epsilon Eddy Viscosity Model for High Reynolds Number Turbulent Flows-Model Development and Validation. NASA.
- Son, P., Kim, J., & Ahn, E. (2011). Effects of Bell Mouth Geometries on the Flow Rate of Centrifugal Blowers. *Journal of Mechanical Science and Technology*, 25(9), 2276-2276.
- Sullerey, R., Mishra, S., & Pradeep, A. (2002). Application of Boundary Layer Fences and Vortex Generators in Improving Performance of S-Duct Diffusers. *Transactions of ASME Journal of Fluids Engineering*, 124, 136-142.
- Tapparo, A., Marton, D., Giorio, C., Zanella, A., Vivan, L., Girolami, V., Solda, L., Marzaro, M. (2012). Assessment of the Environmental Exposure of Honeybees to Particulate Matter Containing Neonicotinoid Insecticides Coming from Corn Coated Seeds. *Environmental Science and Technology*, 2012(46), 2592-2599.
- Versteeg, H., Malalasekera, W. (2007). *An Introduction to Computational Fluid Dynamics*. (2nd ed.). Essex, England: Pearson Education Limited.
- White, F. (2011). *Fluid Mechanics* (7th ed.). New York: McGraw Hill.
- Wolfshtein, M. (1970). Some Solutions of the Plane Turbulent Impinging Jet. *Journal of Basic Engineering*, 92(4), 915-922.

APPENDIX A

EFFECT OF OUTLET SHAPE ON VELOCITY DISTRIBUTION FOLLOWING JET IMPINGEMENT

This appendix documents a CFD study of the effect of the shape of the outlet producing a jet that impinges on a horizontal surface is presented in this appendix. Different outlet configurations are considered and the velocity contours 1 cm above the ground plane are presented for each outlet shape. The goal of this study is to qualitatively determine the extent to which the exhaust shape influences the impinging jet, and to aid in explaining the differences between the modelled results and the experimental results compared in Chapter 4. The geometry of the models used in this study, shown in Figure A-1, are based on the model of the fan exhaust jet impinging on the ground presented in Chapter 3.

Exhaust geometry A, is a round jet exhaust (16 cm radius) that will be used as a baseline to document the performance of a classical jet as described by Wolfshtein (1970). Exhaust geometry B, is a rectangular exhaust (26 cm x 8 cm) to examine the basic shape of the fan exhaust, and exhaust geometry C is a rectangular exhaust (26 cm x 8 cm) that is angled at the end to more closely mimic the shape of the fan exhaust.

For each of the CFD models the exhaust flow is discharged 50 cm above the ground plane, with the domain comprising a 2 m radius cylinder centred on the exhaust. The domain is discretized using a coarse structured mesh made up of approximately 265,000 cells, ranging in size from 0.01 m to 0.8 m. All of the simulations use a realisable k - ϵ eddy viscosity model to model the turbulence.

Results from the study are presented in Figures A.2 through A.6, in the form of velocity contour plots with direction vectors. The contours are taken at 1 cm above the ground plane in all cases.

The first simulation used exhaust geometry A, with a velocity inlet (exhaust velocity) of 7 m/s. Figure A.2 shows that as predicted by Wolfshtein, the velocity field is in the shape of concentric circles with slower velocities radiating evenly outward from the point of impingement. The coarse mesh prevents the velocity profile from remaining circular as the wall jet travels away from the point of impingement.

The second simulation used exhaust geometry B, with a velocity inlet (exhaust velocity) of 7 m/s. Figure A.3 shows that changing the exhaust shape from circular to rectangular greatly changes the shape of the velocity field of the impinging jet. This field is more oval shaped with high velocity peaking in one direction, similar to the field observed from the fan exhaust impingement. However, the field from the rectangular exhaust is much more symmetrical compared to that of the fan (Figure 4-3).

Figure A.4 shows the results of the third simulation, which used exhaust geometry C, with a velocity inlet (exhaust velocity) of 7 m/s. The angled exhaust outlet causes the velocity field to have a more asymmetric shape around the $90^\circ/270^\circ$ axis, with higher velocities occurring under the shorter side (located at 0°) of the exhaust.

Figure A.5 shows the results of the fourth simulation, which used exhaust geometry C, with the velocity inlet (exhaust location) divided in two parts. The first part was 19 cm in length and set to 7 m/s. The second part was the remaining 7 cm of the exhaust and set to 9.5 m/s. This was to more closely model the fan exhaust profile, with the higher velocity located on the 0° side of the exhaust. This velocity profile, combined with the asymmetries produced by the exhaust angle, increased the velocities in the 0° direction, and decreased those in the 180° direction.

Figure A.6 shows the results of the fifth and final simulation modelling exhaust geometry C, with the velocity inlet (exhaust location) divided in two parts and the ground plane inclined at 1° . The incline is about the $0^\circ/180^\circ$ axis, i.e. the 90° side is lower than the 270° side. The velocity inlet is same as that of the fourth simulation. Inclining the ground plane noticeably reduced the velocities seen in the 270° direction as compared to the previous simulation. Also, there was a reduction in the extent of the peak velocities shown in the 0° direction.

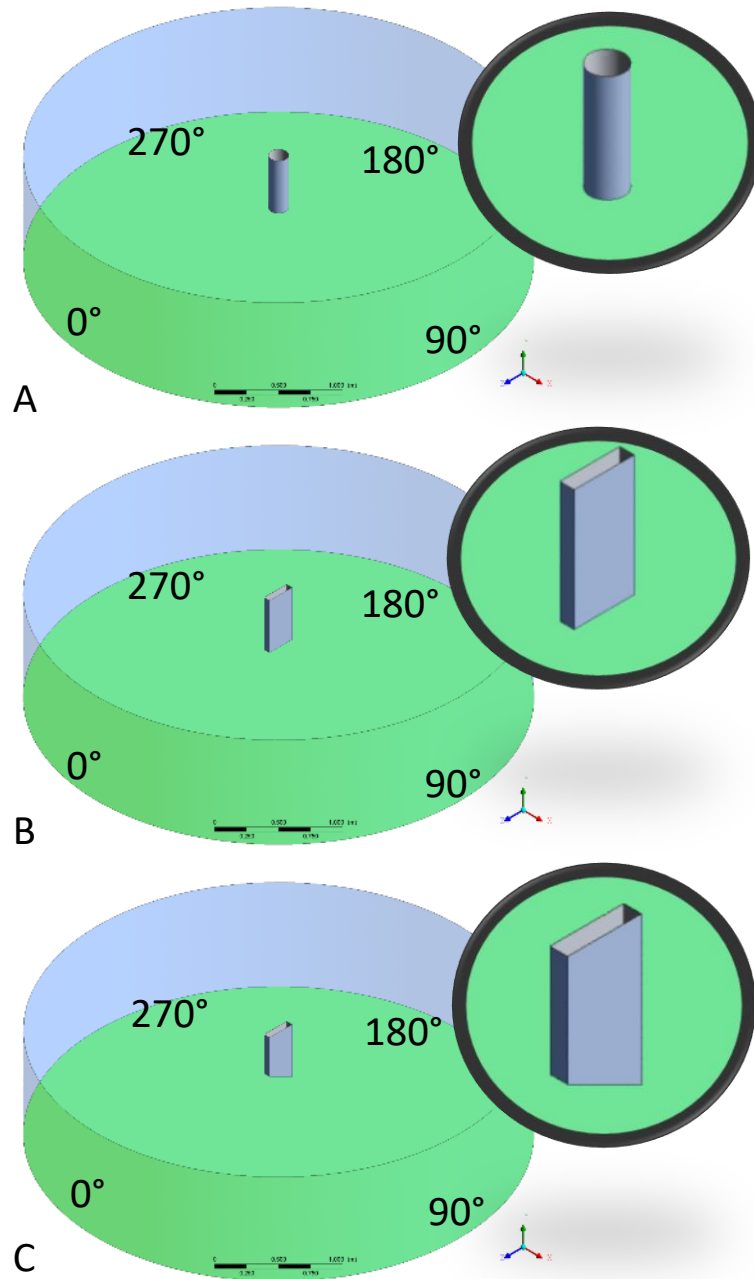


Figure A.1: Geometries used in outlet shape study

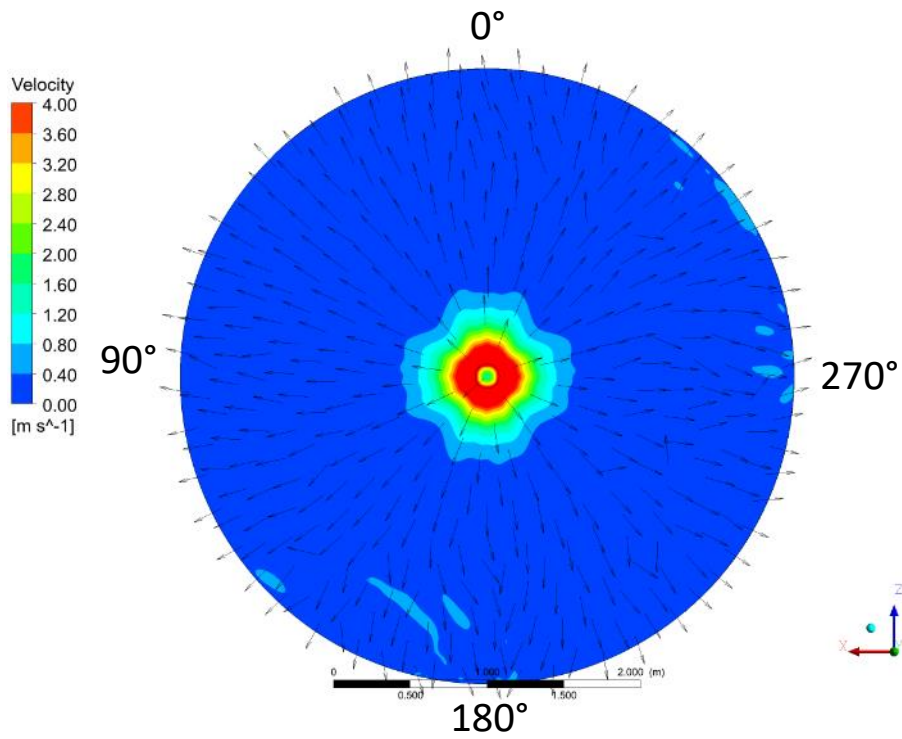


Figure A.2: Velocity contours and vectors resulting from a round jet impinging upon the ground

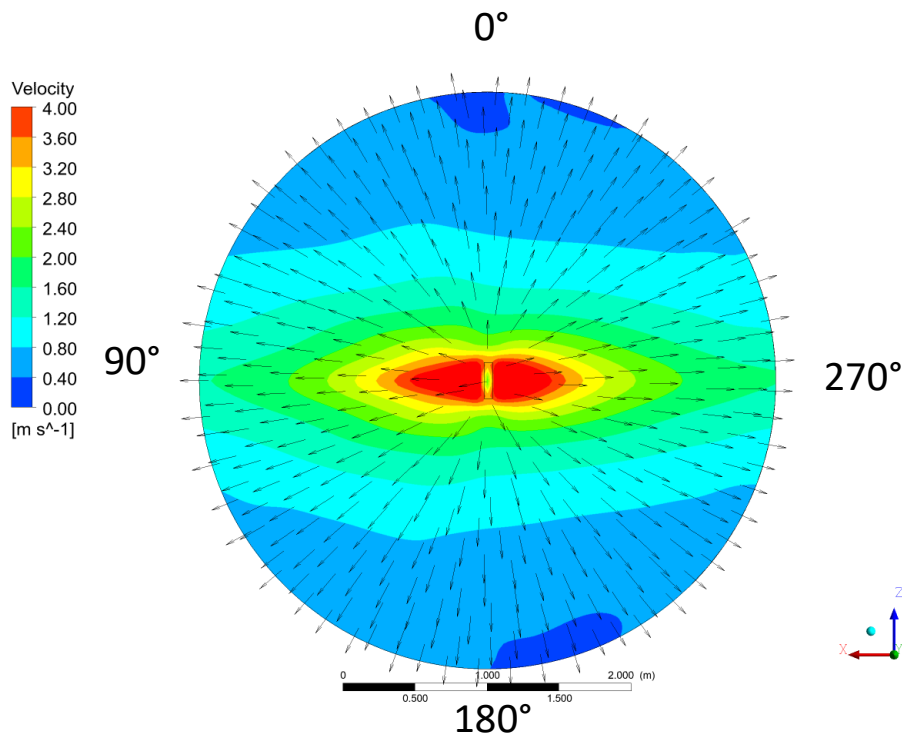


Figure A.3: Velocity contours and vectors resulting from a rectangular jet impinging upon the ground

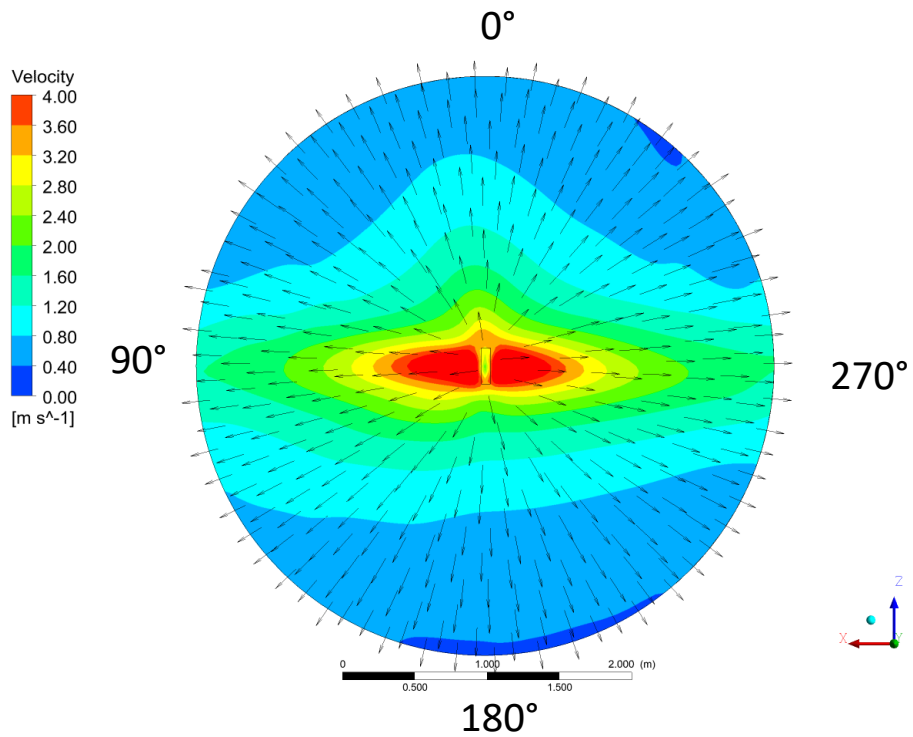


Figure A.4: Velocity contours and vectors resulting from an angled rectangular jet impinging upon the ground

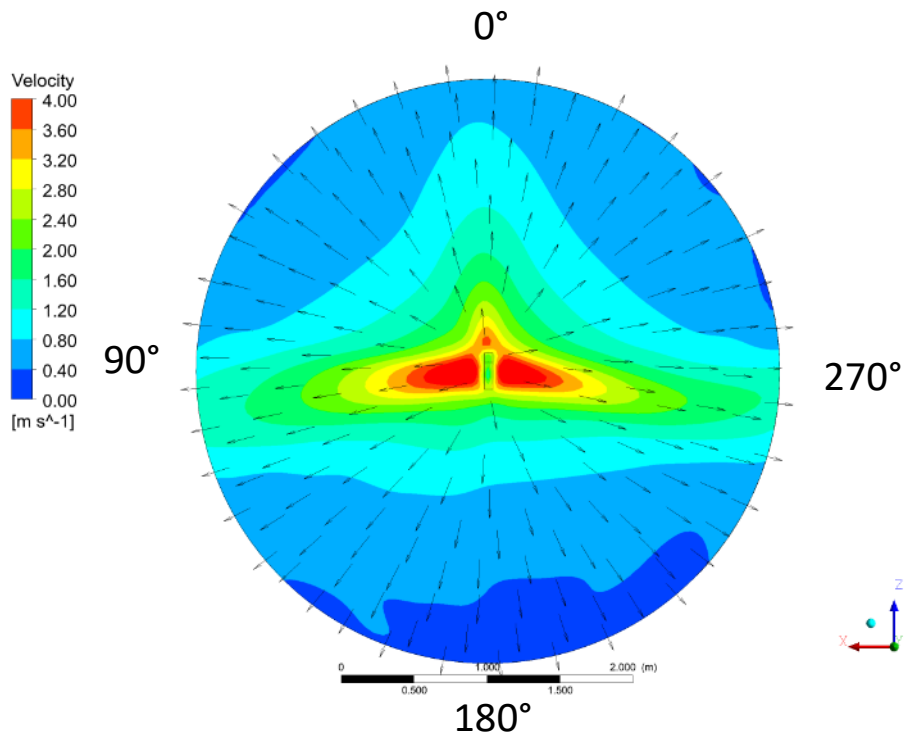


Figure A.5: Velocity contours and vectors resulting from an angled rectangular jet with a non-uniform velocity profile impinging upon the ground

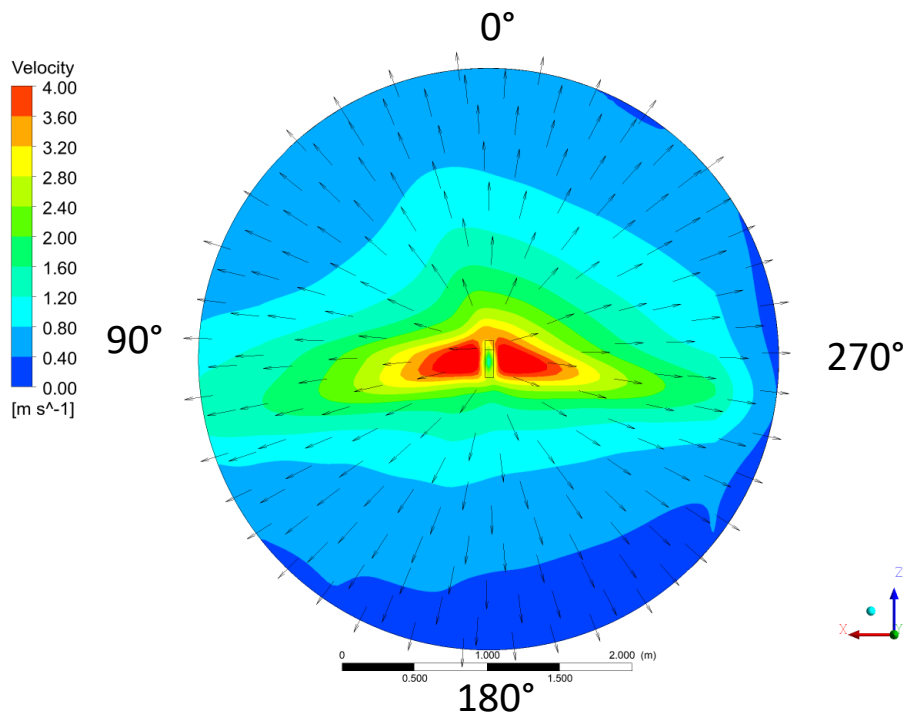


Figure A.6: Velocity contours and vectors resulting from an angled rectangular jet with a non-uniform velocity profile impinging upon a 1° sloped ground

APPENDIX B
FURTHER WORK RESULTING FROM THIS RESEARCH PROJECT

All the experimental section of this work was performed during the fall and winter of 2013. After sharing the experimental results with CNH Industrial, the production fan casing was redesigned. Figure B.1 shows the redesigned vacuum fan. In the figure *A* shows the new fan installed on the planter, *B* and *C* show the fan in detail.

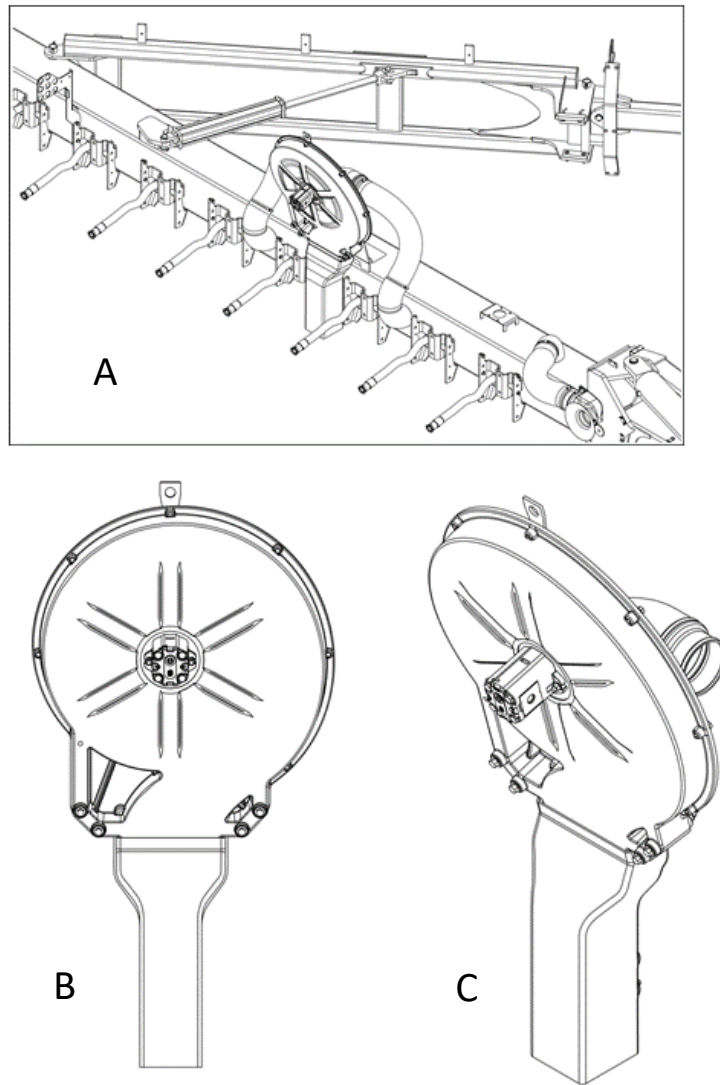


Figure B.1: Resigned planter vacuum fan with integrated diffuser, images courtesy of CNH Industrial

The new fan redirects the exhaust to point towards the ground through an integrated diffuser, which according the data above will allow the fan to meet the ISO 17962 standard. The new fan has been in production since 2017.

Also, research was performed on the ability of the diffuser to attenuate the high amount of noise produced by the vacuum fan, as recommended at the end of this thesis. A prototype combination diffuser and muffler was designed, built, and tested. It was found that using quarter wavelength cavities inside the diffuser, a 10 dB attenuation in noise level could be achieved. Since the combination diffuser and muffler was so effective in attenuating the noise, the design was patented. Figure B.2a and Figure B.2b show the first two pages of the granted patent, US 9,599,124 B2.



(12) **United States Patent**
Roberge et al.

(10) **Patent No.:** **US 9,599,124 B2**
(45) **Date of Patent:** **Mar. 21, 2017**

- (54) **AIR DIFFUSER FOR VACUUM FAN OF PLANTERS**
- (71) Applicant: **CNH Industrial Canada, Ltd.**,
Saskatoon (CA)
- (72) Inventors: **Martin Roberge**, Saskatoon (CA);
Michael Boyko, Saskatoon (CA); **Brian J. Anderson**, Yorkville, IL (US)
- (73) Assignee: **CNH Industrial Canada, Ltd.**,
Saskatoon, Saskatchewan (CA)
- (*) Notice: Subject to any disclaimer, the term of this patent is extended or adjusted under 35 U.S.C. 154(b) by 392 days.
- (21) Appl. No.: **14/243,689**
- (22) Filed: **Apr. 2, 2014**

- (65) **Prior Publication Data**
US 2015/0285269 A1 Oct. 8, 2015
- (51) **Int. Cl.**
F04D 29/44 (2006.01)
F04D 17/16 (2006.01)
F04D 29/42 (2006.01)
F04D 29/66 (2006.01)
- (52) **U.S. Cl.**
CPC **F04D 29/441** (2013.01); **F04D 17/168** (2013.01); **F04D 29/4226** (2013.01); **F04D 29/664** (2013.01); **F04D 29/665** (2013.01); **F05D 2250/52** (2013.01)
- (58) **Field of Classification Search**
CPC .. F04D 29/441; F04D 29/665; F04D 29/4226; F04D 17/168; F04D 29/664; F05D 2250/52
USPC 415/119, 120, 200, 206
See application file for complete search history.

- (56) **References Cited**
U.S. PATENT DOCUMENTS
- | | | | |
|---------------|---------|--------------------|-------------|
| 2,726,807 A * | 12/1955 | Lewis | A47L 7/0009 |
| | | | 15/320 |
| 3,196,977 A | 7/1965 | Sanders | |
| 3,794,137 A | 2/1974 | Teodorescu et al. | |
| 4,050,913 A | 9/1977 | Roach | |
| 4,076,099 A | 2/1978 | Proksch | |
| 4,177,629 A | 12/1979 | Kennedy | |
| 4,236,597 A | 12/1980 | Kiss et al. | |
| 4,281,740 A | 8/1981 | Weiss et al. | |
| 4,325,459 A | 4/1982 | Martin | |
| 4,669,952 A * | 6/1987 | Forsyth, III | F04D 29/444 |
| | | | 415/119 |
| 4,718,924 A | 1/1988 | DeMarco | |
| 4,786,299 A | 11/1988 | DeMarco | |
| 4,810,269 A | 3/1989 | Stackhouse et al. | |
| 5,127,238 A * | 7/1992 | Ichikawa | B60H 1/3204 |
| | | | 415/53.1 |
- (Continued)

- OTHER PUBLICATIONS**
- Reference notes retrieved from Google.com, "Farm Machinery and Power", Power et al. dated Dec. 31, 2007 (1 page).
- Primary Examiner* — Hoang Nguyen
(74) *Attorney, Agent, or Firm* — Rebecca L. Henkel;
Rickard K. DeMille

(57) **ABSTRACT**

A diffuser for the vacuum fan used with agricultural equipment. The diffuser has a rectangular outlet fixed to the outlet of the fan and a diverging rectangular cross-section outlet for increasing the cross-sectional flow area. A primary flow path between the inlet and the outlet is no less in area than the inlet to the diffuser and a series of rectangular side chambers with perforated walls covered by sound deadening material have predetermined dimensions to decrease the outlet air velocity attenuate selected noise frequencies.

15 Claims, 2 Drawing Sheets

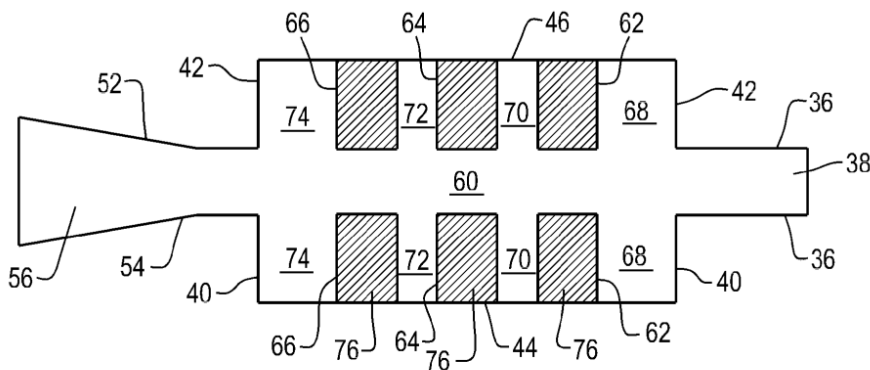


Figure B.2a: Patent granted for combination diffuse muffler design

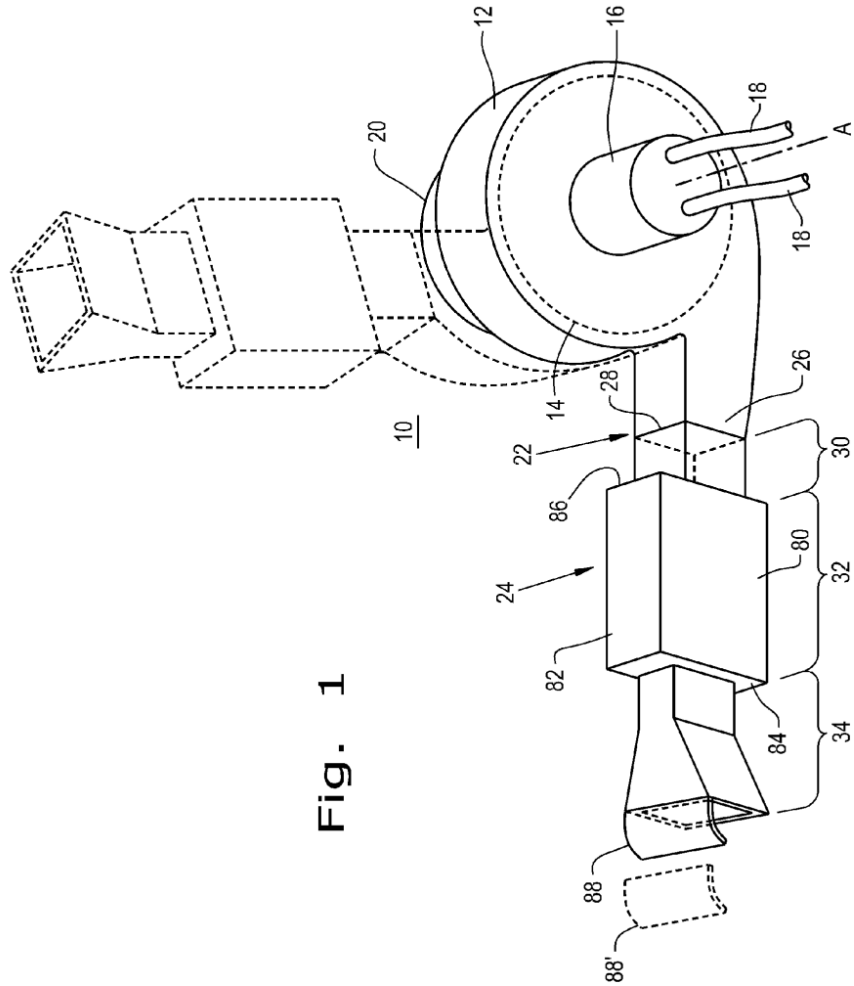


Fig. 1

Figure B.2b: Patent granted for combination diffuse muffler design